THE UNIVERSITY OF WARWICK

Library Declaration and Deposit Agreement

1. STUDENT DETAILS

Please complete the following:

Full name: ……

University ID number: ……

2. THESIS DEPOSIT

2.1 I understand that under my registration at the University, I am required to deposit my thesis with the University in BOTH hard copy and in digital format. The digital version should normally be saved as a single pdf file.

2.2 The hard copy will be housed in the University Library. The digital version will be deposited in the University's Institutional Repository (WRAP). Unless otherwise indicated (see 2.3 below) this will be made openly accessible on the Internet and will be supplied to the British Library to be made available online via its Electronic Theses Online Service (EThOS) service.
[At present, theses submitted for a Master's degree by Research (MA, MSc, LLM, MS or MMedSci) are not being deposited in WRAP and not being made available via EthOS. This may change in future.]

2.3 In exceptional circumstances, the Chair of the Board of Graduate Studies may grant permission for an embargo to be placed on public access to the hard copy thesis for a limited period. It is also possible to apply separately for an embargo on the digital version. (Further information is available in the *Guide to Examinations for Higher Degrees by Research*.)

2.4 *If you are depositing a thesis for a Master's degree by Research, please complete section (a) below. For all other research degrees, please complete both sections (a) and (b) below:*

(a) Hard Copy

I hereby deposit a hard copy of my thesis in the University Library to be made publicly available to readers (please delete as appropriate) EITHER immediately OR after an embargo period of ……..... months/years as agreed by the Chair of the Board of Graduate Studies.

I agree that my thesis may be photocopied. YES / NO (*Please delete as appropriate*)

(b) Digital Copy

I hereby deposit a digital copy of my thesis to be held in WRAP and made available via EThOS.

Please choose one of the following options:

EITHER My thesis can be made publicly available online. YES / NO (*Please delete as appropriate*)

OR My thesis can be made publicly available only after…..[date] (Please give date)
YES / NO (*Please delete as appropriate*)

OR My full thesis cannot be made publicly available online but I am submitting a separately identified additional, abridged version that can be made available online.
YES / NO (*Please delete as appropriate*)

OR My thesis cannot be made publicly available online. YES / NO (*Please delete as appropriate*)

3. GRANTING OF NON-EXCLUSIVE RIGHTS

Whether I deposit my Work personally or through an assistant or other agent, I agree to the following:

Rights granted to the University of Warwick and the British Library and the user of the thesis through this agreement are non-exclusive. I retain all rights in the thesis in its present version or future versions. I agree that the institutional repository administrators and the British Library or their agents may, without changing content, digitise and migrate the thesis to any medium or format for the purpose of future preservation and accessibility.

4. DECLARATIONS

(a) I DECLARE THAT:

- I am the author and owner of the copyright in the thesis and/or I have the authority of the authors and owners of the copyright in the thesis to make this agreement. Reproduction of any part of this thesis for teaching or in academic or other forms of publication is subject to the normal limitations on the use of copyrighted materials and to the proper and full acknowledgement of its source.

- The digital version of the thesis I am supplying is the same version as the final, hard-bound copy submitted in completion of my degree, once any minor corrections have been completed.

- I have exercised reasonable care to ensure that the thesis is original, and does not to the best of my knowledge break any UK law or other Intellectual Property Right, or contain any confidential material.

- I understand that, through the medium of the Internet, files will be available to automated agents, and may be searched and copied by, for example, text mining and plagiarism detection software.

(b) IF I HAVE AGREED (in Section 2 above) TO MAKE MY THESIS PUBLICLY AVAILABLE DIGITALLY, I ALSO DECLARE THAT:

- I grant the University of Warwick and the British Library a licence to make available on the Internet the thesis in digitised format through the Institutional Repository and through the British Library via the EThOS service.

- If my thesis does include any substantial subsidiary material owned by third-party copyright holders, I have sought and obtained permission to include it in any version of my thesis available in digital format and that this permission encompasses the rights that I have granted to the University of Warwick and to the British Library.

5. LEGAL INFRINGEMENTS

I understand that neither the University of Warwick nor the British Library have any obligation to take legal action on behalf of myself, or other rights holders, in the event of infringement of intellectual property rights, breach of contract or of any other right, in the thesis.

Please sign this agreement and return it to the Graduate School Office when you submit your thesis.

Student's signature: .....…… Date: .....

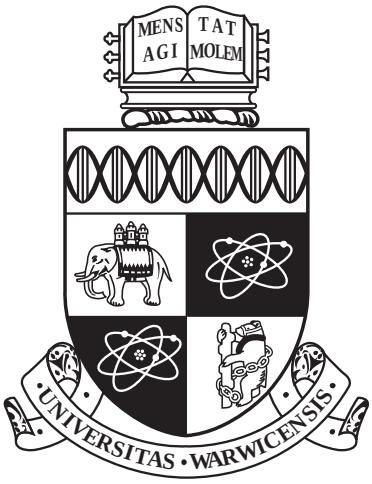

Hybrid simulations of flow bursts in magnetically confined plasmas

by

Peter William Gingell

Thesis

Submitted to the University of Warwick

for the degree of

Doctor of Philosophy

Department of Physics

March 2013

THE UNIVERSITY OF
WARWICK

Contents

List of Tables

List of Figures

Acknowledgments

I would first like to thank Professor Sandra Chapman and Professor Richard Dendy for their continual help and support over the last three and a half years. I also owe thanks to the EPOCH development team for their work on the PIC code adapted for this work, and for helping me through bugs in the early days. I also wish to recognise the rest of the CFSA for providing such a great atmosphere to work in. And of course, I will always be thankful for the unwavering support of my parents at every step in my education.

This work was part-funded by the EPSRC and the RCUK Energy Programme under grant EP/I501045 and the European Communities under the contract of Association between EURATOM and CCFE. The views and opinions expressed herein do not necessarily reflect those of the European Commission.

This thesis was typeset with LaTeX 2_ε[1] by the author.

[1] LaTeX 2_ε is an extension of LaTeX. LaTeX is a collection of macros for TeX. TeX is a trademark of the American Mathematical Society. The style package warwickthesis was used.

Declarations

I hereby declare that this thesis is my own work, except where explicitly stated, and that it has not been submitted for another degree at the University of Warwick, or any other University.
The results presented in Chapters 3 and 4 have been published in [Gingell et al., 2012] and [Gingell et al., 2013] respectively.

P. W. Gingell
May, 2013

Abstract

Strongly localised concentrations or depressions of plasma density and magnetic field strength ("blobs") are ubiquitous in the edge region of tokamak fusion experiments. They contribute significantly to heating and transport in that region, and therefore to overall energy confinement. The existing fusion plasma literature in this area focuses primarily on blobs sufficiently large that a fluid description is appropriate. However, the blob population may include some - not necessarily easily detectable - whose characteristic lengthscales are on the order of the ion gyro-scales. This implies that a description at the fluid level is unlikely to capture the full dynamics. In this Thesis, therefore, we report hybrid (particle ions, fluid electrons) particle-in-cell simulations of ion gyro-scale blobs, which enable us to examine the effects of finite Larmor radius on their dynamics, evolution, and their ability to heat the near-edge plasma. We find that ion gyro-scale blobs are advected with the background flow, and develop a twin-celled vortex structure. Asymmetry then arises from finite ion Larmor radius kinetics, manifesting in the size of the internal vortices, the shape of tails forming from blob ejecta, and the growth of a Kelvin-Helmholtz instability. Small scale blobs are also found to increase ion energies more than larger blobs as a result of ion pick-up at the upstream blob-background boundary, which may result in a significant increase in plasma energy caused by a blob population that is not yet directly observable. Finally, we examine the creation of ion gyro-scale blobs using hybrid simulations of kinetic interchange and Kelvin-Helmholtz instabilities, and present statistics of the sizes of blobs created by these instabilities, and power-laws for the resulting particle displacements.

Chapter 1

Introduction

1.1 Fusion Energy

The impact of climate change and the potential shortage of traditional fossil fuels in the future makes the search for new sources of energy that are safe, efficient and scalable critical to a planet with ever-increasing population and development. Although some renewable energy technologies, such as solar cells and wind turbines, show promise in certain regions of the world, energy transport, the space required for such endeavours, and the limited ability of these technologies to provide a stable base-load, all invite another approach to solving the energy crisis. Nuclear technologies, although not strictly renewable, can provide stable power loads with an energy output per kilogram of fuel at least six orders of magnitude greater than fossil fuels, without the release of greenhouse gases that can drive climate change. However, development of nuclear fission power may present issues with non-proliferation of nuclear weapons and storage of radioactive waste. Nuclear fusion possesses the advantages of greater energy release per gram of fuel than fission, with a clean and abundant fuel source in sea water, and radioactive waste products have manageable half-lives on the order of a human lifetime. For these reasons, nuclear fusion is seen by many as the most promising energy source of the future, and research into the use of nuclear fusion as an energy source has been ongoing since the 1950s.

In order for nuclei to fuse, they must overcome the electric Coulomb repulsion due to their positive charges, which leads to a low interaction cross-section for fusion at low energies. This fusion cross section informs the choice of reaction used for fusion power generation. The fusion of deuterium and/or tritium can occur by several reactions. These include deuterium-tritium, deuterium-deuterium, and deuterium-helium interactions as follows:

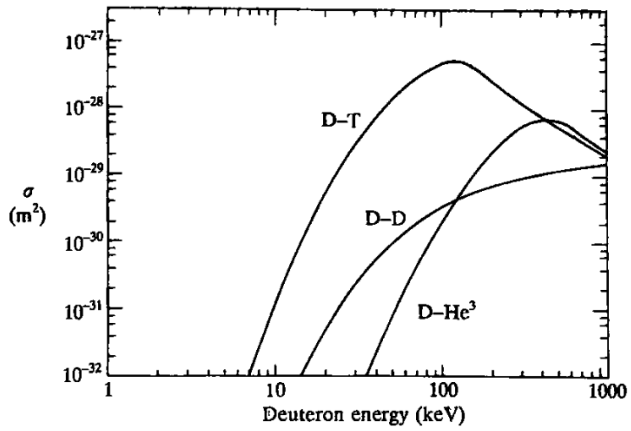

Figure 1.1: Temperature dependence of the fusion cross-sections σ for the D-T, D-D and D-He reactions. Reproduced from [Wesson, 2004].

$$ {}^{2}_{1}\mathrm{D} + {}^{3}_{1}\mathrm{T} \rightarrow {}^{4}_{2}\mathrm{He} + {}^{1}_{0}\mathrm{n} + 17.6\mathrm{MeV} \tag{1.1} $$

$$ {}^{2}_{1}\mathrm{D} + {}^{2}_{1}\mathrm{D} \rightarrow {}^{3}_{2}\mathrm{He} + {}^{1}_{0}\mathrm{n} + 3.27\mathrm{MeV} \tag{1.2} $$

$$ {}^{2}_{1}\mathrm{D} + {}^{2}_{1}\mathrm{D} \rightarrow {}^{3}_{1}\mathrm{T} + {}^{1}_{1}\mathrm{H} + 4.03\mathrm{MeV} \tag{1.3} $$

$$ {}^{2}_{1}\mathrm{D} + {}^{3}_{2}\mathrm{He} \rightarrow {}^{4}_{2}\mathrm{He} + {}^{1}_{1}\mathrm{H} + 18.3\mathrm{MeV} \tag{1.4} $$

The cross sections for these reactions are plotted in Figure 1.1. It can be seen that the cross section for the D-T reaction is orders of magnitude more than the other interactions except at impractically high temperatures. Hence, we choose D-T reactions for power generation, and note that the interaction cross-section increases with energy, to a maximum of 100 keV.

The principle at the heart of the technology is that of confinement. A fusion reaction results in a positive energy gain if the particles react before losing their energy. Hence, particles must retain their energy and remain in the reacting region for a sufficient time, i.e. they must be confined. The product of this time and density must be sufficiently large. This criterion, called the Lawson criterion, serves as a threshold for a successful fusion reactor, and can be expressed for the deuterium-tritium reaction, as follows:

$$ nT\tau_E \geq 5 \times 10^{21} \mathrm{m}^{-3}\mathrm{skeV}, \tag{1.5} $$

where n is the peak density, T is the peak temperature, and τ_E is the energy confine-

ment time. At sufficiently high temperatures, fuel becomes an ionised gas known as a plasma, which consists of ions and free electrons. At these temperatures, a simple material wall is not able to confine the plasma, and a more novel approach is required. Broadly speaking, two promising methods for fusion are being explored. For inertial confinement fusion (ICF), a solid fuel pellet is rapidly heated by means of an ultra-high intensity laser, which causes implosion of the pellet as the outer layers are ablated. In this case, particles are confined for a very short time by their inertia alone. The Lawson criterion may be satisfied by the high densities present in the centre of the imploding fuel pellet. For magnetic confinement fusion (MCF), toroidal magnetic fields are used to confine a low-density plasma for an extended period of time in a device known as a tokamak. The Lawson criterion is then satisfied in spite of low densities by a long confinement time. Within this Thesis, we focus on magnetic confinement fusion as a solution to fusion energy research.

Magnetic confinement fusion using a tokamak, and the particular experimental challenges that drive the research presented in this Thesis, will be discussed in Section 1.3. However, in order to inform the reader of the physics that form basis of many concepts in magnetic confinement fusion research, we begin with an introduction to plasma physics.

1.2 Plasma Physics

A plasma is a state of matter which occurs when the temperature of a gas is large enough to overcome the electrostatic forces binding the electrons to the constituent atoms (e.g Dendy [1993]). The particles are ionised, giving a fluid with two or more, oppositely charged populations: electrons and ionised atoms. However, plasmas are differentiated from ionised gases by their ability to shield the Coulomb potential of free charges over a lengthscale known as the Debye length [Debye and Hückel, 1923], defined by:

$$\lambda_d = \sqrt{\frac{\varepsilon_0 k_B T}{2 n_0 e^2}}. \tag{1.6}$$

where T_e is the electron temperature, and is n_e the electron number density. For the plasma approximation to hold, the Debye sphere, with radius λ_d, must contain enough electrons to shield a Coulomb potential applied at its centre. This implies that interactions between charged particles and the plasma are dominated by collective behaviour of many particles, rather than collisions with nearest neighbours. This condition can be expressed as $N_d \gg 1$, where $N_d = 4\pi n_e \lambda_d^3/3$. The extremely

high electrical conductivity of the state gives rise to many unique properties and phenomena, and instabilities and non-linearities in the governing equations make plasma physics a challenging field.

A brief introduction to some of the key concepts in plasma physics is presented below as part of a hierarchy of plasma phenomena. At the smallest length and time scales, plasma phenomena can be treated in terms of single particle dynamics, or at larger scales using a distribution function. These models, which make use of full particle trajectories, are referred to as "kinetic". At even larger spatial and temporal scales, we can make use of reduced models, for which we average over single particle trajectories. These are referred to as "fluid" models, and may comprise multiple fluids of charged particles or, in the case of magnetohydrodynamics, a single quasi-neutral fluid.

1.2.1 Single Particle Dynamics

Charged particles in a plasma are subject to the Lorentz force, given by

$$\mathbf{F} = q(\mathbf{E} + \mathbf{v} \times \mathbf{B}) \tag{1.7}$$

where q is the particle's charge, $\mathbf{E}$ is the electric field, $\mathbf{B}$ is the magnetic field, and $\mathbf{v}$ is the particle's velocity (e.g. Dendy [1993]). If $\mathbf{B} = 0$, a particle is freely accelerated by the electric field. However, if instead $\mathbf{E} = 0$, the equation of motion becomes

$$\frac{m}{e}\dot{\mathbf{v}} = \mathbf{v} \times \mathbf{B}. \tag{1.8}$$

To determine the trajectories of particles subject to a background magnetic field, it is useful to split the velocity into components parallel and perpendicular to the magnetic field, $\mathbf{v} = \mathbf{v}_{\parallel} + \mathbf{v}_{\perp}$. Since the $\mathbf{v} \times \mathbf{B}$ force has no component in the parallel direction, the parallel velocity is constant. Particles, therefore, move at a constant velocity along magnetic field lines. The perpendicular velocity is determined by:

$$\ddot{\mathbf{v}}_{\perp} = -\Omega^2 \mathbf{v}_{\perp}, \tag{1.9}$$

$$\Omega = \frac{qB}{m}. \tag{1.10}$$

Hence, each component of $\mathbf{v}_{\perp}$ undergoes simple harmonic motion, leading to circular motion of the particle around the magnetic field line with frequency Ω, which is known as the cyclotron frequency, or gyrofrequency. The radius of that

oscillation, known as the cyclotron radius or gyroradius, is given by

$$\rho = v_\perp/\Omega. \tag{1.11}$$

By taking the scalar product of Equation 1.8 with velocity, we find

$$\frac{m}{e}\mathbf{v}\cdot\dot{\mathbf{v}} = \frac{d}{dt}\left(\frac{1}{2}mv^2\right) = \mathbf{v}\cdot(\mathbf{v}\times\mathbf{B}) = 0. \tag{1.12}$$

Hence, the kinetic energy $w = (1/2)mv^2$ is a constant of the motion. Since the velocity along the field line remains constant, $w_\parallel$ is constant, and from $w = w_\parallel + w_\perp$ we can conclude that both $w_\perp$ and $v_\perp$ are also constant. This implies that the gyro-radius ρ and the cyclotron frequency Ω are both constant of the motion. A particle with arbitrary initial velocity will thus follow a helical trajectory around a guiding centre which is parallel to the magnetic field lines. Particles with positive charge rotate in a left-handed sense compared to the magnetic field, and particles with a negative charge rotate in a right-handed sense.

In the more complex case for which we include both static electric and magnetic fields, the parallel and perpendicular components of the motion decouple (e.g. Dendy [1993]), giving the following equations of motion:

$$\frac{m}{e}\dot{\mathbf{v}}_\parallel = \mathbf{E}_\parallel \tag{1.13}$$

$$\frac{m}{e}\dot{\mathbf{v}}_\perp = \mathbf{E}_\perp + \mathbf{v}_\perp\times\mathbf{B} \tag{1.14}$$

where components are defined parallel and perpendicular to the magnetic field. Hence, a charged particle freely accelerates parallel to $\mathbf{B}$. Now, if we transform to a reference frame with constant velocity $\mathbf{v}_d$ such that $\mathbf{v}_\perp = \mathbf{c}_\perp + \mathbf{v}_d$, the perpendicular equation of motion becomes

$$\frac{m}{e}\dot{\mathbf{c}}_\perp = \mathbf{E}_\perp + \mathbf{v}_d\times\mathbf{B} + \mathbf{c}_\perp\times\mathbf{B}. \tag{1.15}$$

We can then choose $\mathbf{v}_d$ such that

$$\mathbf{v}_d = \frac{\mathbf{E}\times\mathbf{B}}{B^2}, \tag{1.16}$$

and Equation 1.15 reduces to the form of the perpendicular component of Equation 1.8,

$$\frac{m}{e}\dot{\mathbf{c}}_\perp = \mathbf{c}_\perp\times\mathbf{B}. \tag{1.17}$$

As before, this leads to circular motion around the magnetic field line. Hence, particle motion in an electromagnetic field can be decomposed into three parts:

$$\mathbf{v} = v_{\parallel} \frac{\mathbf{B}}{|\mathbf{B}|} + \mathbf{v}_d + \mathbf{c}_{\perp} \tag{1.18}$$

where $v_{\parallel}$ is motion along B, $\mathbf{v}_d$ is a uniform drift velocity, and $\mathbf{c}_{\perp}$ is the gyration. By taking a time average over $\mathbf{v}$, we can show that the drift velocity $\mathbf{v}_d$ is the average perpendicular velocity. Hence, the only effect of adding an electric field in addition to the magnetic field is for particles to drift with velocity v_d in the $\mathbf{E} \times \mathbf{B}$ direction. This is known as $\mathbf{E} \times \mathbf{B}$ drift, and has several notable features [Gurnett and Bhattacharjee, 2005]. First, the drift velocity is independent of particle charge, mass and energy. Second, since all particles have the same drift velocity, the $\mathbf{E} \times \mathbf{B}$ drift produces no net current. Finally, since contours of electrostatic potential are perpendicular to $\mathbf{E}$, the $\mathbf{E} \times \mathbf{B}$ drift velocity follows contours of constant potential. The $\mathbf{E} \times \mathbf{B}$ drift is consistent with the frame dependence of the electric field $\mathbf{E}' = \mathbf{E} + \mathbf{u}_F \times \mathbf{B}$, where u_F is the relative velocity of the frame transformation.

The drift of charged particles due to any force perpendicular to the magnetic field can be approximated by considering an equivalent electric field $\mathbf{E}_{\perp} = \mathbf{F}_{\perp}/q$. In this case, the drift velocity becomes:

$$\mathbf{v}_F = \frac{\mathbf{F}_{\perp} \times \mathbf{B}}{qB^2}. \tag{1.19}$$

Common examples of such a forces are the gravitational force $\mathbf{F} = m\mathbf{g}$ and pressure gradient $\mathbf{F} = -\nabla p$. Note that, unlike the standard $\mathbf{E} \times \mathbf{B}$ drift, $\mathbf{v}_F$ is oppositely directed for particles of positive and negative charge. Hence, the $\mathbf{F} \times \mathbf{B}$ drift results in a net current in the plasma and, for a plasma of finite size, charge polarisation at the plasma's boundary. In this case, the resulting electric field leads to an $\mathbf{E} \times \mathbf{B}$ drift in the direction of the polarising force $\mathbf{F}$.

Further drifts can arise as a result of gradients or curvature in the magnetic field due to variations in the instantaneous radius of curvature of the gyration. Consider a gradient in the magnetic field $\nabla \mathbf{B}$ perpendicular to the background field. The cyclotron radius is decreased in regions of strong magnetic field, and is increased in regions of weak magnetic field. Assuming the magnetic field variation is small, and that the particle trajectory is periodic in the $\nabla \mathbf{B}$ direction, the $\mathbf{v} \times \mathbf{B}$ force time averaged over a full gyration is zero:

$$\oint F_x dt = q \oint v_y B_z dt = 0, \tag{1.20}$$

where x is in the $\nabla\mathbf{B}$ direction, z is in the $\mathbf{B}$ direction, and y is perpendicular to both. Expanding the magnetic field about the guiding centre using a Taylor series yields:

$$B_z(x) = B_z(x_0) + \frac{\partial B_z}{\partial x}(x - x_0) + \dots. \tag{1.21}$$

Substituting this into Equation 1.20 gives:

$$B_z(x_0) \oint v_y dt + \frac{\partial B_z}{\partial x} \oint v_y(x - x_0)dt = 0. \tag{1.22}$$

The integral in first term gives Δy, the distance moved in the y-direction over one full orbit. The integral in the second term gives the area of the near-circular gyration such that

$$\oint v_y(x - x_0)dt = \oint (x - x_0)dy = -\frac{q}{|q|}\pi\rho^2. \tag{1.23}$$

Note that the $q/|q|$ term arises due to the oppositely directed gyration of oppositely charged particles, and so the path integral is performed in the reverse direction. Hence, we can write the drift velocity as

$$v_{\nabla B} = \frac{\Delta y}{\Delta t} = \frac{1}{\Delta t}\frac{1}{B_z}\frac{\partial B_z}{\partial x}\left(\frac{q}{|q|}\pi\rho^2\right). \tag{1.24}$$

With $\Delta t = 2\pi/\Omega$, this can be generalised in vector form as:

$$\mathbf{v}_{\nabla B} = \frac{m\Omega^2\rho^2}{2qB}\frac{\mathbf{B} \times \nabla\mathbf{B}}{B^2}. \tag{1.25}$$

The curvature drift can be calculated by considering that a particle moving along a curved magnetic field line is subject to a centrifugal force $F_C = mv_\parallel^2/R_C$, where R_C is the radius of curvature of the field line. Since this force acts parallel to the magnetic field, we can simply substitute the centrifugal force into the generalised perpendicular force drift, Equation 1.19. Hence, the curvature drift is:

$$\mathbf{v}_C = -m\frac{v_\parallel^2}{R_C^2}\frac{\mathbf{R}_c \times \mathbf{B}}{qB^2}. \tag{1.26}$$

The ∇B and curvature drifts are both inversely proportional to the scale length of the inhomogeneity in the magnetic field, and proportional to the kinetic energy of the particles. Hence, the magnitude of both drifts are controlled by the ratio of the gyro-radius to the length scale of the field inhomogeneity. The dependence of the drift velocities on the particle kinetic energies means that these drifts

dominate over the $\mathbf{E} \times \mathbf{B}$ drift for high energy (hot) particles. Additionally, since the drifts do not necessarily occur along contours of constant potential, these drifts can cause particles to gain or lose energy.

In these inhomogeneous fields, which are equivalent to time varying magnetic fields under a frame transformation, the magnetic moment mu of charged particles is approximately conserved. For a particle undergoing cyclotron motion, the magnetic moment is given by $mu = w_\perp/B$, where $w_\perp$ is the perpendicular kinetic energy. This conservation is equivalent to maintaining a constant magnetic flux through the cyclotron orbit. However, this invariant of the motion is not exact, and applies only if the electromagnetic fields vary sufficiently slowly, i.e. the magnetic moment is an adiabatic invariant of the system. For example, the magnetic moment is not conserved for resonant interactions of particles with waves, or for the interaction of particles with discontinuities in the magnetic field, as found in shocks.

1.2.2 The Vlasov Equation

Kinetic theories describe the behaviour of a plasma in terms of the particle motions described in Section 1.2.1 [Wesson, 2004]. As required by the plasma approximation, there are a large number of particles involved. The treatment is therefore statistical, and requires the use of a distribution function $f(\mathbf{x}, \mathbf{v}, t)$ defined as

$$dN = f(\mathbf{x}, \mathbf{v}, t)\, d^3x\, d^3y \tag{1.27}$$

where dN is the number of particles in the phase-space volume element $d^3x d^3v$ at a time t. The total number of particles is thus obtained by integrating the distribution function $f(\mathbf{x}, \mathbf{v}, t)$ over all phase space.

In order to obtain the macroscopic properties of the plasma, we must integrate over the distribution function in phase space. The average value of any quantity $g(\mathbf{x}, \mathbf{v})$ in a region R of phase space is given by:

$$\langle g(\mathbf{x}, \mathbf{v}) \rangle = \frac{1}{N} \int_R g(\mathbf{x}, \mathbf{v}) f(\mathbf{x}, \mathbf{v}, t)\, d^3x\, d^3v. \tag{1.28}$$

Hence, the number density can be calculated by integrating the distribution function over the velocity space, thereby taking the zeroth moment. For a species j:

$$n_j(\mathbf{x}, t) = \int_V f_j(\mathbf{x}, \mathbf{v}, t)\, d^3v \tag{1.29}$$

Similarly, the first-order moment can be used to calculate particle fluxes by multiplying by $\mathbf{v}$ then integrating over the velocity space. Hence the current density $\mathbf{J}$ is

given by:

$$\mathbf{J}_j(\mathbf{x},t) = q_j \int_V \mathbf{v} f_j(\mathbf{x},\mathbf{v},t)\, d\mathbf{v}. \tag{1.30}$$

From conservation of particles, we can write the rate of change of the exact distribution function F, which includes every particle in the system, as

$$\frac{DF}{Dt} = 0 \tag{1.31}$$

$$\frac{\partial F}{\partial t} + \mathbf{v}\cdot\nabla F + \dot{\mathbf{v}}\cdot\nabla_{\mathbf{v}} F = 0 \tag{1.32}$$

$$\frac{\partial F}{\partial t} + \mathbf{v}\cdot\nabla F + \frac{q}{m}(\mathbf{E}+\mathbf{v}\times\mathbf{B})\cdot\nabla_{\mathbf{v}} F = 0 \tag{1.33}$$

where we have include the Lorentz force, and $F = f + \delta f$ is the combination of the ensemble average $f = \langle F \rangle$ and small fluctuations for which $\langle \delta f \rangle = 0$ [Baumjohann and Treumann, 1996]. We can decompose the electromagnetic fields in a similar way, such that $\mathbf{E} = \langle \mathbf{E} \rangle + \delta\mathbf{E}$ and $\mathbf{B} = \langle \mathbf{B} \rangle + \delta\mathbf{B}$. Substituting these into 1.33 and taking the ensemble average gives the kinetic equation

$$\frac{\partial f}{\partial t} + \mathbf{v}\cdot\nabla f + \frac{q}{m}(\langle\mathbf{E}\rangle + \mathbf{v}\times\langle\mathbf{B}\rangle)\cdot\nabla_{\mathbf{v}} f = -\frac{q}{m}\langle(\delta\mathbf{E} + \mathbf{v}\times\delta\mathbf{B})\cdot\nabla_{\mathbf{v}}\delta F\rangle \tag{1.34}$$

for which the electromagnetic fields and phase space density f are dependent only upon phase space coordinates $(\mathbf{x},\mathbf{v},t)$ and not on the positions of each individual particle. To simplify this equation, we can neglect correlations between the fields and account only for collisions between particles. In this case, Equation 1.34 reduces to the Boltzmann equation, given by:

$$\frac{\partial f}{\partial t} + \mathbf{v}\cdot\nabla f + \frac{q}{m}(\langle\mathbf{E}\rangle + \mathbf{v}\times\langle\mathbf{B}\rangle)\cdot\nabla_{\mathbf{v}} f = \left(\frac{\partial f}{\partial t}\right)_c \tag{1.35}$$

where the term $(\partial f/\partial t)_c$ accounts for all changes in the distribution function due to particle collisions. Finally, we can neglect particle collisions to arrive at the Vlasov equation [Vlasov, 1945], given by

$$\frac{\partial f}{\partial t} + \mathbf{v}\cdot\nabla f + \frac{q}{m}(\langle\mathbf{E}\rangle + \mathbf{v}\times\langle\mathbf{B}\rangle)\cdot\nabla_{\mathbf{v}} f = 0. \tag{1.36}$$

Integration of this equation characterises kinetic models of plasma dynamics. One such method is described in Chapter 2.

1.2.3 Fluid Approximation

At large space and time scales, for which differences between individual particle gyrations are not important, and hence averaged quantities are sufficient, we make use of fluid models. The equations for a multi-fluid plasma, comprising k species such that the total distribution function $f = f_1 + f_2 + \cdots + f_k$, can be derived by taking moments of the Boltzmann or Vlasov equations [Krall and Trivelpiece, 1973]. To obtain the zeroth moment, we integrate the collisional Boltzmann equation for a species j over all velocity space:

$$\int \left(\frac{\partial f_j}{\partial t} + \mathbf{v} \cdot \frac{\partial f_j}{\partial \mathbf{x}} + \frac{e_j}{m_j} \left(\langle \mathbf{E} \rangle + \mathbf{v} \times \langle \mathbf{B} \rangle \right) \cdot \frac{\partial f_j}{\partial \mathbf{v}} \right) d\mathbf{v} = \int \left(\frac{\partial f_j}{\partial t} \right)_c d\mathbf{v} \tag{1.37}$$

$$\int \frac{\partial f_j}{\partial t} d^3v + \int \mathbf{v} \cdot \nabla f_j d^3v + \frac{1}{m_j} \int \mathbf{F} \cdot \nabla_{\mathbf{v}} f_j d^3v = \int \left(\frac{\partial f_j}{\partial t} \right)_c d\mathbf{v} \tag{1.38}$$

The first integral on the LHS can be re-written as the time derivative of the number density using Equation 2.5:

$$\int \frac{\partial f_j}{\partial t} d^3v = \frac{\partial}{\partial t} \int f_j d^3v = \frac{\partial n_j}{\partial t}. \tag{1.39}$$

Similarly, the second integral relates to the current density and Equation 1.30:

$$\int \mathbf{v} \cdot \nabla f_j d^3v = \nabla \cdot \int \mathbf{v} f_j d^3v = \frac{1}{q_j} \nabla \cdot \mathbf{J}_j. \tag{1.40}$$

The third integral can be rewritten as a surface integral using Gauss' theorem:

$$\int \mathbf{F} \cdot \nabla_{\mathbf{v}} f_j d^3v = \int \nabla_{\mathbf{v}} \cdot (\mathbf{F} f_j) d^3v = \int_S (\mathbf{F} f_j) \cdot d\mathbf{S}_v = 0, \tag{1.41}$$

which vanishes on the assumption that, for the distribution function f_j, $\Pr[V > v]$ converges as $v \to \infty$. Finally, the collisional term on the RHS vanishes since collisions cannot change the number density. Hence, Equation 1.38 reduces to the charge continuity equation:

$$\frac{\partial}{\partial t} \rho_j + \nabla \cdot (\rho_j \mathbf{v}_j) = 0, \tag{1.42}$$

where ρ_j is the mass or charge density for a species j.

The momentum equation can be derived by taking the first moment of the Vlasov equation. Multiplying by the momentum $m_j \mathbf{v}$ and integrating, we arrive at the equation

$$m_j \int \mathbf{v} \frac{\partial f_j}{\partial t} d^3v + m_j \int \mathbf{v}(\mathbf{v} \cdot \nabla f_j) d^3v + \int \mathbf{v}(\mathbf{F} \cdot \nabla_{\mathbf{v}} f_j) d^3v = m_j \int \mathbf{v} \left(\frac{\partial f_j}{\partial t} \right)_c d^3v. \tag{1.43}$$

The first integral can be rewritten as the time derivative of the bulk velocity field $\mathbf{U}_j$:

$$m_j \int \mathbf{v} \frac{\partial f_j}{\partial t} d^3v = \frac{\partial}{\partial t}(m_j n_j \mathbf{U}_j). \tag{1.44}$$

The second integral can be reduced to the divergence of the pressure tensor $\vec{\mathbf{P}}_j$ and outer product of the bulk velocity field:

$$m_j \int \mathbf{v}(\mathbf{v} \cdot \nabla f_j) d^3v = \nabla \cdot \vec{\mathbf{P}}_j + \nabla \cdot (m_j n_j \mathbf{U}_j \mathbf{U}_j). \tag{1.45}$$

On the assumption that the distribution function falls to zero sufficiently rapidly at infinite velocity, and using the property of the Lorentz force $\mathbf{F} \cdot \nabla_{\mathbf{v}} f_j = \nabla_{\mathbf{v}} \cdot (\mathbf{F} f_j)$, the third integral can be rewritten simply as:

$$\int \mathbf{v}(\mathbf{F} \cdot \nabla_{\mathbf{v}} f_j) d^3v = -q_j n_j (\mathbf{E} + \mathbf{U}_j \times \mathbf{B}). \tag{1.46}$$

Finally, the integral over the collision operator can be written as the rate of change of momentum per unit volume due to collisions: $(\partial \mathbf{p}_j / \partial t)_c$. Hence, the combined momentum equation becomes:

$$\frac{\partial}{\partial t}(m_j n_j \mathbf{U}_j) + \nabla \cdot (m_j n_j \mathbf{U}_j \mathbf{U}_j) = q_j n_j (\mathbf{E} + \mathbf{U}_j \times \mathbf{B}) - \nabla \cdot \vec{\mathbf{P}}_j + \left(\frac{\partial \mathbf{p}_j}{\partial t} \right)_c. \tag{1.47}$$

Defining the convective derivative evaluated along trajectories of a fluid element as

$$\frac{d}{dt} = \frac{\partial}{\partial t} + (\mathbf{U}_j \cdot \nabla), \tag{1.48}$$

we arrive at the common form of the momentum equation for species j:

$$m_j n_j \frac{d\mathbf{U}_j}{dt} = q_j n_j (\mathbf{E} + \mathbf{U}_j \times \mathbf{B}) - \nabla \cdot \vec{\mathbf{P}}_j + \left(\frac{\partial \mathbf{p}_j}{\partial t} \right)_c. \tag{1.49}$$

A similar analysis taking the second moment of the Vlasov equation by multiplying by the tensor $\mathbf{vv}$ and integrating leads to energy conservation equation of the fluid. These equations, coupled with Maxwell's equations and an equation of state for each species, are the equations of multi-fluid plasma theory, for which we

can treat all ion species and electrons separately.

1.2.3.1 Magnetohydrodynamics

Magnetohydrodynamics (MHD) models a plasma as a single, electrically neutral conducting fluid. In this case, we define mass density as the sum of the mass densities of all species $\rho_m = \sum_i \rho_{m,i}$, and the velocity field of the centre of mass as the mass weighted sum of the fields for each species $\mathbf{U} = (\sum_i \rho_{m,i}\mathbf{U}_i)/\rho_m$. The mass continuity equation and momentum equation follow from the multi-fluid model under the assumptions of quasi-neutrality and an isotropic pressure tensor:

$$\frac{\partial \rho_m}{\partial t} + \nabla \cdot (\rho_m \mathbf{U}) = 0 \tag{1.50}$$

$$\rho_m \frac{d\mathbf{U}}{dt} = \mathbf{J} \times \mathbf{B} - \nabla \cdot \vec{\mathbf{P}}_0 \tag{1.51}$$

Here, the total pressure tensor $\vec{\mathbf{P}}_0 = \sum_i \vec{\mathbf{P}}_{0,i}$, where the pressure for a species i is given by

$$\vec{\mathbf{P}}_{0,i} = \vec{\mathbf{P}}_i + \rho_{m,i}(\mathbf{U}_i - \mathbf{U})(\mathbf{U}_i - \mathbf{U}), \tag{1.52}$$

which includes both the ram pressure and thermal pressure, and allows for populations of different temperatures and anisotropies in the pressure tensor $\vec{\mathbf{P}}_i$. An Ohm's law arises for MHD from a combination of the electron and ion momentum equations under the assumption that differences in the velocity fields of the ions and electrons and small, and making use of the fact $m_e \ll m_i$:

$$\mathbf{J} = \sigma(\mathbf{E} + \mathbf{U} \times \mathbf{B}). \tag{1.53}$$

Maxwell's equations are reduced by two assumptions. First, under the low frequency limit for which temporal variations are assumed to be slow, the displacement current $\frac{1}{c^2}\partial\mathbf{E}/\partial t$ can be ignored compared to the conduction current $\mu_0\mathbf{J}$. Second, with macroscopic lengthscales $L \to \infty$, the plasma can be assumed to be electrically neutral such that charge density $\rho \to 0$. Under these conditions, Maxwell's equations reduce to:

$$\nabla \times \mathbf{B} = \mu_0 \mathbf{J} \tag{1.54}$$

$$\nabla \cdot \mathbf{B} = 0 \tag{1.55}$$

$$\nabla \times \mathbf{E} = -\frac{\partial \mathbf{B}}{\partial t} \tag{1.56}$$

$$\nabla \cdot \mathbf{E} = 0 \tag{1.57}$$

Finally, the equations can be closed with an equation of state, often assumed to be a power law of the form

$$\frac{d}{dt}(p\rho_m^{-\gamma}) = 0. \tag{1.58}$$

These equations define the limit known as resistive magnetohydrodynamics. Further reductions of the model are possible. For example, ideal MHD describes a fluid for which convection of the magnetic field dominates over diffusion such that magnetic field lines are "frozen in" to the fluid, and Ohm's law reduces to $\mathbf{E} + \mathbf{U} \times \mathbf{B} = 0$.

1.2.4 Plasma Instabilities

Plasmas may be subject to instabilities caused by the accumulation of free energy in inhomogeneous regions of phase space. These instabilities can be categorised into macro- and microinstabilities. At large spatial scales, those comparable to the scale lengths of the bulk plasma, macroinstabilities occur for accumulations of free energy in spatial inhomogeneities in configuration space. At small spatial scales, comparable to the inertial length or gyro-radii of particle species in the plasma, we observe microinstabilities for which kinetic effects are more important. In contrast to macroinstabilities, microinstabilities occur for accumulations of free energy in inhomogeneities in velocity space.

Here, we review the instabilities with relevance to the work presented in this Thesis.

1.2.5 Microinstabilities

Microinstabilities occur for plasmas with inhomogeneities in velocity space, and hence are important for populations with non-Maxwellian phase space distributions. Perhaps the simplest example is the electrostatic bump-on-tail or gentle beam instability. In this case, the growth rate of Langmuir waves is proportional to the slope of the electron distribution function f_e in velocity space, $(\partial f_e/\partial t)_v$. For a

Maxwellian distribution of electrons with thermal velocity v_{th}, the slope is negative everywhere, and thermal particles may damp the Langmuir waves in a process known as Landau damping (e.g. [Treumann and Baumjohann, 1997]). However, if we introduce a low-density, fast electron beam with velocity $v_b > v_{th}$ and narrow thermal spread, a region exists for which $(\partial f_e/\partial t)_v$ is positive and Landau damping is inverted, leading to unstable growth of Langmuir waves.

An electromagnetic microinstability with particular relevance to the work presented in this Thesis is the damping and instability associated with cyclotron resonances. Resonance occurs for low-frequency, parallel propagating electromagnetic waves with left- or right-circular polarisation. For these waves, the electric field is perpendicular to the magnetic field and rotates in the same sense as electron gyration for right-circular polarised waves such as the whistler wave, and in the same sense as ion gyration for left-circular polarised waves such as the ion cyclotron wave. Hence, particles with a particular parallel velocity will see a constant perpendicular electric field in their own frame of reference, and will interact strongly with the wave. This resonance condition can be expressed as

$$k_{\parallel} v_{\parallel} = \omega - n\Omega_i, \tag{1.59}$$

for the nth harmonic of the cyclotron frequency Ω_i.

The physical mechanism of the interaction is demonstrated in Figure 1.2. Here, we consider the case of the interaction of ions with a left-circularly polarised wave. For ions with parallel velocity greater than the wave phase speed, the wave will have negative phase speed in the ion guiding centre frame, and appear to rotate in a right-handed sense. Conversely, for ions with parallel velocity less than the wave phase speed, the electric field vector will appear to rotate in a left handed sense in the ion guiding centre frame. Hence, for slow ions the electric field rotates in the same direction as the ion gyration, and the ion will be accelerated by the wave electric field in the perpendicular direction. As a result of the transfer of energy from wave to particle, the wave will be damped. Fast ions do not see a stationary electric field, and hence do not interact. The inverse interaction occurs for a distribution function with an excess of particles at higher momentum than the wave. In this case, particles may be decelerated by the wave electric field. This interaction may lead to unstable growth of the resonant waves if the distribution function of the resonant particles includes a temperature anisotropy with excess in the perpendicular direction (e.g. [Treumann and Baumjohann, 1997]).

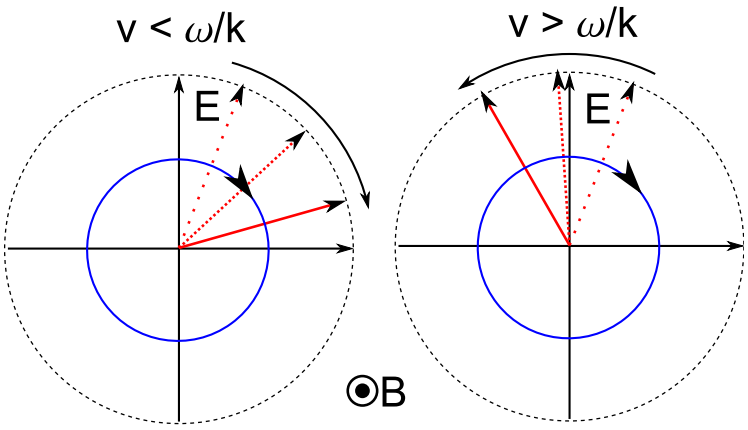

Figure 1.2: Illustration of the direction of rotation of the left-circularly polarised wave responsible for cyclotron damping of ions. The magnetic field and direction of propagation of the wave are out of the plane of the paper, and the ion gyration direction is shown in blue. Rotation of the wave electric field (red) as seen by ions with parallel velocity slower than the wave phase speed in shown on the left, and the same for ions faster than the phase speed is shown on the right.

1.2.5.1 Interchange Instability

Interchange instabilities are a class of plasma macroinstabilities which involve a specific kind of perturbation: the swap, or "interchange", of plasma between two adjacent magnetic flux tubes. These instabilities have been observed in many astrophysical and laboratory environments, including the Earth's magnetosphere [Southwood and Kivelson, 1987] and the edge region of tokamaks [Bisai et al., 2005; Russell et al., 2007]. We can derive the stability condition using a magnetohydrodynamic model [Gurnett and Bhattacharjee, 2005] by first considering the linearised form of the momentum equation:

$$\rho_{m0}\frac{\partial^2 \xi}{\partial t^2} = \frac{1}{\mu_0}\left[(\nabla \times \mathbf{B}) \times \mathbf{B}_0 + (\nabla \times \mathbf{B}_0) \times \mathbf{B}\right] - \nabla \delta p \tag{1.60}$$

where ξ is the perturbation displacement vector, the subscript "0" denotes background fields. We can eliminate the magnetic field and pressure perturbations from this equation by considering the induction equation and continuity equation respectively. From the linearised and time integrated form of the induction equation, we can derive

$$\mathbf{B} = \nabla \times (\xi \times \mathbf{B}_0), \tag{1.61}$$

and from the continuity equation, again linearised and time integrated with an

adiabatic equation of state, we find

$$\delta p = -\xi \cdot \nabla p_0 - \gamma p_0 \nabla \cdot \xi. \tag{1.62}$$

Hence, we can rewrite Equation 1.60 as

$$\rho_{m0} \frac{\partial^2 \xi}{\partial t^2} = \mathbf{F}(\xi), \tag{1.63}$$

where $\mathbf{F}(\xi)$ is the linear force operator defined by

$$\begin{aligned} \mathbf{F}(\xi) &= \frac{1}{\mu_0} \left[(\nabla \times \{\nabla \times (\xi \times \mathbf{B}_0)\}) \times \mathbf{B}_0 + (\nabla \times \mathbf{B}_0) \times \{\nabla \times (\xi \times \mathbf{B}_0)\} \right] \\ &\quad + \nabla \left[\xi \cdot \nabla p_0 - \gamma p_0 \nabla \cdot \xi \right]. \end{aligned} \tag{1.64}$$

To determine stability of perturbations ξ, we consider the conservation of energy $\delta K + \delta W = C$ where perturbed kinetic and potential energies are given by

$$\delta K = \frac{1}{2} \int_V \rho_{m0} \left(\frac{\partial \xi}{\partial t} \right)^2 d^3x, \tag{1.65}$$

$$\delta W = -\frac{1}{2} \int_V \xi^* \cdot \mathbf{F}(\xi)\, d^3x. \tag{1.66}$$

Here, we consider an initial displacement ξ with zero velocity. We require that this displacement makes δW negative, and it follows that the total energy $C < 0$. We now define the quantity

$$I(t) - \frac{1}{2} \int_V \rho_{m0} |\xi|^2 \, d^3x. \tag{1.67}$$

Taking the second derivative of I, and substituting in the equations for δK and δW, we arrive at

$$\frac{d^2 I}{dt^2} = 2(2\delta K - C). \tag{1.68}$$

By definition, δK must be positive at all times and C is negative as described above. This gives us the condition:

$$\frac{d^2 I}{dt^2} > -2C > 0. \tag{1.69}$$

This implies that I, and hence ξ, must increase without bound if the initial perturbation makes δW negative. Thus, $\delta W \geq 0$ is a necessary condition for stability.

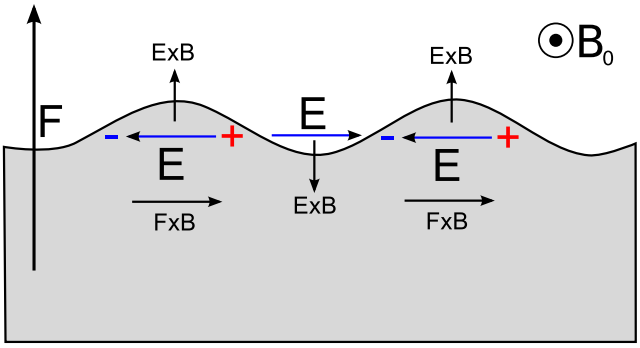

Figure 1.3: Relevant vectors described in the discussion of the mechanism of the interchange instability. The higher density region is shaded in grey.

In the case of interchange of plasma between adjacent flux tubes, we can thus conclude from Equation 1.66 that a displacement of a boundary between flux tubes is unstable if there exists a force with a component parallel to the displacement, i.e. $\xi \cdot \mathbf{F}(\xi) > 0$. These forces can include the gravitational force, in the case of a plasma supported against gravity by a perpendicular magnetic field, a pressure gradient resulting from inhomogeneities in density, temperature and magnetic field strength, the centrifugal force acting on a rapidly rotating plasma, and the magnetic curvature force on the outboard midplane of a tokamak.

The mechanism of the instability for models which permit charge separation can be understood by considering the effect of polarising drifts which result from these forces. The geometry for this discussion is presented in Figure 1.3. The force $\mathbf{F}$ responsible for the instability results in a $\mathbf{F}\times\mathbf{B}$ drift. Since the $\mathbf{F}\times\mathbf{B}$ is dependent on particle charge, electrons and ions drift in opposite directions, generating a net current. For a ripple-like perturbation on a boundary between regions of different number density, this drift causes charges to separate and accumulate at the ripple boundary, generating an electric field. $\mathbf{E}\times\mathbf{B}$ drift of particles in the $\mathbf{F}$ direction in the over-dense regions and $-\mathbf{F}$ direction in the under-dense regions causes the perturbation to grow.

1.2.5.2 Kelvin-Helmholtz Instability

The Kelvin-Helmholtz instability is a macroinstability which arises from the interaction of Alfvén waves across a shear boundary. This instability is ubiquitous in plasma physics, and has been observed in a wide variety of astrophysical and laboratory environments. These include the Earth's magnetosphere [Hasegawa et al., 2004; Nykyri and Otto, 2001], comets [Ershkovich, 1980], the solar corona [Foullon

et al., 2011; Ofman and Thompson, 2011], and the edge region of tokamak plasmas [Garbet et al., 1999; Chapman et al., 2012]. The condition for instability and the growth rate can be determined using the dispersion relation, which we derive here. Let us assume an ideal magnetohydrodynamic case, as described in Section 1.2.3.1, for which the ideal Ohm's law, induction equation, Ampère's law and momentum equation are given by:

$$\begin{aligned} \mathbf{E} &= -\mathbf{v} \times \mathbf{B} && (1.70)\\ \frac{\partial \mathbf{B}}{\partial t} &= -\nabla \times \mathbf{E} && (1.71)\\ \mu_0 \mathbf{J} &= \nabla \times \mathbf{B} && (1.72)\\ \rho \left(\frac{\partial}{\partial t} + \mathbf{v} \cdot \nabla \right) \mathbf{v} &= \mathbf{J} \times \mathbf{B} - \nabla p. && (1.73) \end{aligned}$$

Substituting 1.70 into 1.71 to eliminate $\mathbf{E}$ and 1.72 into 1.73 to eliminate $\mathbf{J}$, these become:

$$\begin{aligned} \frac{\partial \mathbf{B}}{\partial t} &= \nabla \times (\mathbf{v} \times \mathbf{B}) && (1.74)\\ \rho \left(\frac{\partial}{\partial t} + \mathbf{v} \cdot \nabla \right) \mathbf{v} &= \frac{1}{\mu_0} (\nabla \times \mathbf{B}) \times \mathbf{B} - \nabla p. && (1.75) \end{aligned}$$

By introducing a perturbation to these fields $\mathbf{B} = \mathbf{B}_0 + \delta\mathbf{B}$, $\mathbf{v} = \mathbf{v}_0 + \delta\mathbf{v}$, $p = p_0 + \delta p$ and linearising 1.74 and 1.75, we obtain the following equations which govern the perturbations:

$$\begin{aligned} \frac{\partial}{\partial t} \delta\mathbf{B} &= \nabla \times (\delta\mathbf{v} \times \mathbf{B}_0) && (1.76)\\ \mu_0 m_i n_0 \frac{\partial}{\partial t} \delta\mathbf{v} &= -\mu_0 \nabla \delta p + (\nabla \times \mathbf{B}_0) \times \delta\mathbf{B} + (\nabla \times \delta\mathbf{B}) \times \mathbf{B_0}. && (1.77) \end{aligned}$$

We now replace the plasma velocity perturbation $\delta\mathbf{v}$ with displacement vector $\mathrm{d}\delta\mathbf{x}/\mathrm{d}t$ and integrate in time:

$$\begin{aligned} \delta\mathbf{B} &= \nabla \times (\delta\mathbf{x} \times \mathbf{B}_0) && (1.78)\\ \mu_0 m_i n_0 \frac{\mathrm{d}^2}{\mathrm{d}t^2} \delta\mathbf{v} &= -\mu_0 \nabla \delta p + (\nabla \times \mathbf{B}_0) \times \delta\mathbf{B} + (\nabla \times \delta\mathbf{B}) \times \mathbf{B_0}. && (1.79) \end{aligned}$$

From both magnetic and gas pressures, the first order perturbation in the total

pressure is given by

$$\mu_0 \delta p_{\rm tot} = \mu_0 \delta p + \mathbf{B}_0 \cdot \delta \mathbf{B}, \tag{1.80}$$

and hence with the elimination of $\delta\mathbf{B}$ from 1.79 we obtain for $\delta\mathbf{x}$

$$m_i n_0 \left((\mathbf{v}_A \cdot \nabla)^2 - \frac{\partial^2}{\partial t^2} \right) \delta\mathbf{x} = \nabla \delta p_{\rm tot} - \delta\mathbf{B}\cdot\nabla\mathbf{B}_0 + \mathbf{B}_0 \cdot \nabla(\mathbf{B}_0 \nabla\cdot\delta\mathbf{x} + \delta\mathbf{x}\cdot\nabla\mathbf{B}_0), \tag{1.81}$$

where $\mathbf{v}_A = \mathbf{B}_0/\sqrt{\mu_0 m_i n_0}$ is the background Alfvén velocity. From the solenoid condition $\nabla \cdot \mathbf{B}_0 = \nabla \cdot \delta\mathbf{B} = 0$, the divergence of 1.81 can be written in terms of the total pressure perturbation as

$$\nabla^2 \delta p_{\rm tot} = -m_i \nabla \cdot \left(n_0 \frac{{\rm d}^2 \delta\mathbf{x}}{{\rm d}t^2} \right) + \frac{1}{\mu_0} \nabla \times (\delta\mathbf{B} \cdot \nabla\mathbf{B}_0 + \mathbf{B}_0 \cdot \nabla\delta\mathbf{B}). \tag{1.82}$$

If we assume now that the plasma is homogeneous on each side of the discontinuity such that pressure balance is satisfied everywhere except the boundary, the perturbation must be incompressible, i.e. $\nabla \cdot \delta\mathbf{v} = 0$. Hence the right hand side of 1.82 vanishes, giving us

$$\nabla^2 \delta p_{\rm tot} = 0, \tag{1.83}$$

and under the same homogeneity assumption, 1.81 becomes

$$m_i n_0 \left((\mathbf{v}_A \cdot \nabla)^2 - \frac{\partial^2}{\partial t^2} \right) \delta\mathbf{x} = \nabla \delta p_{\rm tot}. \tag{1.84}$$

We now seek a plane wave solution to 1.83 and 1.84 in the (x, z) plane on the shear boundary to derive the following equations for the displacement and pressure perturbations:

$$\delta\mathbf{x} = \frac{\nabla \delta p_{\rm tot}}{m_i n_0 [\omega^2 - (\mathbf{k} \cdot \mathbf{v}_A)^2]} \tag{1.85}$$

$$\delta p_{\rm tot} = p_0 e^{-k|y|} e^{-i(\omega t - k_x x - k_z z)} \tag{1.86}$$

Since the plasma must remain homogeneous either side of the boundary, the normal component of the displacement $\delta\mathbf{x}$ must be continuous. Additionally, pressure must be continuous across the discontinuity. From these boundary conditions and 1.85, and noting that normals to the boundary are oppositely directed for regions 1 and

2,

$$\frac{1}{n02[\omega_1^2 - (\mathbf{k}\cdot\mathbf{v}_{A1})]} + \frac{1}{n02[\omega_2^2 - (\mathbf{k}\cdot\mathbf{v}_{A2})]} = 0. \tag{1.87}$$

Finally, transforming to a frame in which region 2 is at rest and region 1 has background velocity $\mathbf{v}_0$, the wave frequency ω_1 is Doppler shifted such that $\omega_1 = \omega_2 - \mathbf{k}\cdot\mathbf{v}_0$ where $\omega_2 = \omega$ is the non-shifted frequency. Thus, we have derived the dispersion relation of the Kelvin-Helmholtz instability:

$$\frac{1}{n_{02}[(\omega - \mathbf{k}\cdot\mathbf{v}_0)^2 - (\mathbf{k}\cdot\mathbf{v}_{A1})]} + \frac{1}{n_{01}[\omega_2^2 - (\mathbf{k}\cdot\mathbf{v}_{A2})]} = 0. \tag{1.88}$$

We note here the two terms in 1.88 are Alfvén waves in regions 1 and 2 coupled across the boundary. The roots of this quadratic dispersion relation are as follows:

$$\omega = \frac{n_{01}\mathbf{k}\cdot\mathbf{v}_0}{n_{01}+n_{02}} \pm \sqrt{\left(\frac{n_{01}\mathbf{k}\cdot\mathbf{v}_0}{n_{01}+n_{02}}\right)^2 - \frac{n_{01}(\mathbf{k}\cdot\mathbf{v}_0)^2 - n_{01}(\mathbf{k}\cdot\mathbf{v}_{A1})^2 - n_{02}(\mathbf{k}\cdot\mathbf{v}_{A2})^2}{n_{01}+n_{02}}}. \tag{1.89}$$

Waves at the shear boundary will become unstable when the second term on the left hand side of 1.89 is imaginary, and hence the condition for Kelvin-Helmholtz instability is

$$(\mathbf{k}\cdot\mathbf{v}_0)^2 > \frac{n_{01}+n_{02}}{n_{01}n_{02}}\left[n_{01}(\mathbf{k}\cdot\mathbf{v}_{A1})^2 + n_{02}(\mathbf{k}\cdot\mathbf{v}_{A2})^2\right]. \tag{1.90}$$

This condition is satisfied for sufficiently large shear velocity $\mathbf{v}_0$. We also note that the condition is unconditionally satisfied for waves propagating perpendicular to the background magnetic field.

Equation 1.88 demonstrates that the dispersion relation for the Kelvin-Helmholtz instability contains those for shear Alfvén waves on either side of the boundary. In the kinetic case, and if we treat electrons as a massless fluid of temperature T_e, we can replace the fluid Alfvén waves with the oblique kinetic Alfvén waves with velocity [Baumjohann and Treumann, 1996]:

$$v_{KA\parallel} = v_A\left[1 + k_\perp^2\rho_i^2\left(\frac{3}{4} + \frac{T_e}{T_i}\right)\right]^{1/2} \tag{1.91}$$

$$v_{KA\perp} = \frac{k_\parallel v_A}{k_\perp}\left[1 + k_\perp^2\rho_i^2\left(\frac{3}{4} + \frac{T_e}{T_i}\right)\right]^{1/2}. \tag{1.92}$$

Usually, the parallel wavelength is much longer than the ion gyroradius, such

that $k_\parallel \gg k_\perp \propto \rho_i$. The field-aligned velocity $v_{KA\parallel}$ is larger than the fluid case, and $v_{KA\perp}$ is reduced due to the small ratio $k_\parallel/k_\perp$. Since the perpendicular waves are slowed, the K-H instability has a longer time to grow in the perpendicular $\mathbf{B}_0$ case. Additionally, the Doppler effect on the waves in the moving medium ($\omega_1 = \omega_2 - \mathbf{k}\cdot\mathbf{v}_0$) is dominated by $k_\perp$, as it is therefore large for perpendicular flow. In that case, the K-H instability condition is more easily satisfied, and the growth rate is larger than the fluid case. At small scales in the fluid case, instability occurs at all scales, with linear dependence of the growth rate on the wavenumber. However, finite Larmor radius effects in the kinetic case lead to a stabilisation of small scales, with a complete suppression of growth above a critical wavenumber [Nagano, 1979]. These kinetic effects are visible in the simulations discussed in Chapter 3, and are discussed further in Section 3.4.3.

1.3 Tokamaks

A tokamak is a device which confines a high-temperature plasma using, principally, a toroidal magnetic field. In order to balance magnetic and gas pressure across the device, to prevent ∇p, ∇B and curvature drifts of particles resulting in transport in the radial direction, tokamaks also employ a poloidal magnetic field generated mainly by the plasma's toroidal current. This toroidal current is driven by transformer action of a central primary coil. A current passed through this primary coil creates a magnetic flux change through the torus, and the induced electric field drives the current. The combination of these fields results in helical magnetic field lines on a toroidal surface. The shape of the magnetic field can be controlled further by the use of additional poloidal field coils. The positions of these coils are shown in Figure 1.4.

The plasma confined in a tokamak is heated using a number of different methods as the plasma temperature is increased. In the initial phase, ohmic heating by the current in the plasma raises the temperature to the order of a few keV. Further ohmic heating is difficult because the resistivity falls with an increase in temperature. Since we require temperatures on the order of $\gtrsim$10keV, subsequent heating is achieved using particle beams and resonances with electromagnetic waves. Once ignition of the plasma is achieved, energy released by the nuclear reactions can sustain the high temperatures, and the external sources of heating can be switched off.

The 14MeV neutrons produced by the nuclear reactions are absorbed by a lithium blanket. In addition to depositing heat in the blanket, each lithium-neutron

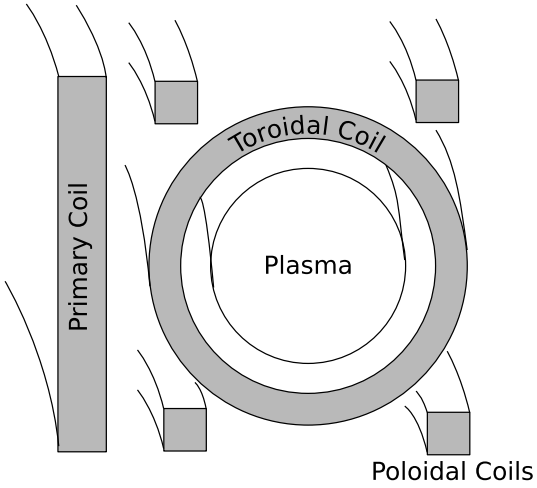

Figure 1.4: Position of the toroidal, poloidal and primary coils in a tokamak.

reaction produces a triton via nuclear fission, effectively breeding tritium fuel which cannot be found in nature. The heat from the blanket can be extracted by means of a fluid coolant, which in turn can be used to heat steam. The steam may then be used to drive a turbine to generate power by conventional means.

The transformer action of the tokamak's primary coil leads to inherently pulsed operation unless a current can be generated by additional means. Although a pulsed operation may be effective if shut down periods are short, a more steady state operation can be achieved by non-inductive current drive using particle beams and resonances with electromagnetic waves. For example, an off-axis beam of neutral particles leads to a transfer of momentum to ions in the toroidal direction which, if collisional losses to electrons are small, generates a net toroidal current. One of the most effective methods using wave resonances is lower hybrid current drive. Lower hybrid waves are longitudinal oscillations of ions and electrons in the plasma directed parallel to the magnetic field. These waves are resonant with high energy electrons on the condition that the electrons' parallel velocity matches the waves' parallel phase velocity. Absorption of the waves by Landau damping leads to momentum transfer to the electrons, generating a net current balanced by the momentum input and loss by collisions to the ions.

The interaction between a hot plasma and the vessel wall of a tokamak can damage internal components and add impurities to the burning plasma, which can cause radiation losses and dilute the fuel. Separation of the burning plasma from the vessel wall is therefore of critical importance to the successful operation of a tokamak. This has been achieved for past and current devices by use of a limiter or, as is more

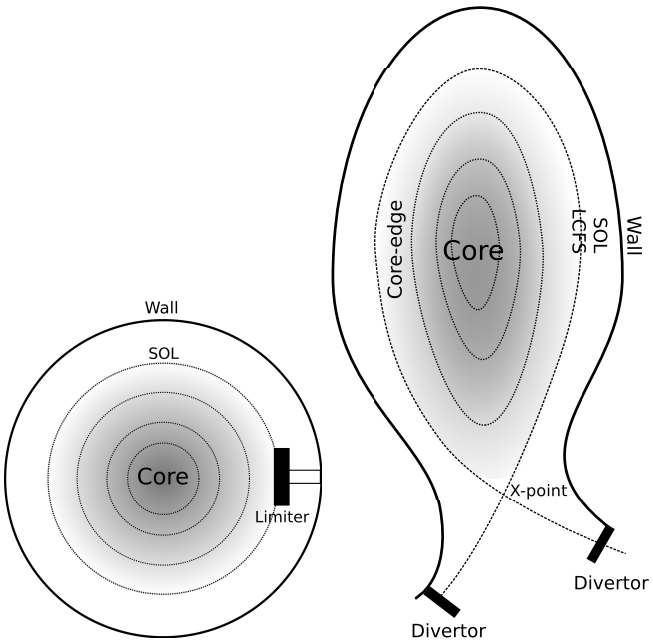

Figure 1.5: Schematic displaying the important regions of a tokamak employing either a limiter (left) or a divertor (right). Poloidal field lines are shown as dotted lines. The last closed flux surface (LCFS) separates the scrape-off layer (SOL) from the core, confined plasma.

common in modern devices, a divertor. A material limiter simply serves as a target which is separated from the vessel wall, and defines the outer limit of the plasma. A divertor target is separated from the main vessel, and requires a modification of the poloidal magnetic field to include at least one x-point. Both these methods define a "scrape-off layer" outside the core, confined region, within which magnetic field lines are connected to the limiter or divertor targets. Hence, particles in the scrape-off layer which have low cross-field transport compared to their speed along the field lines will also strike the targets. These targets are designed to accept heavy particle loads. Since the divertor is separated from the core plasma by means of a magnetic x-point, the return of impurities to the core plasma is significantly reduced over the limiter method. The poloidal magnetic geometry of tokamaks employing limiters and divertors, displaying the core, edge and scrape-off layer regions, is shown in Figure 1.5. The same for a real device, the Mega Ampère Spherical Tokamak, is shown in Figure 1.6.

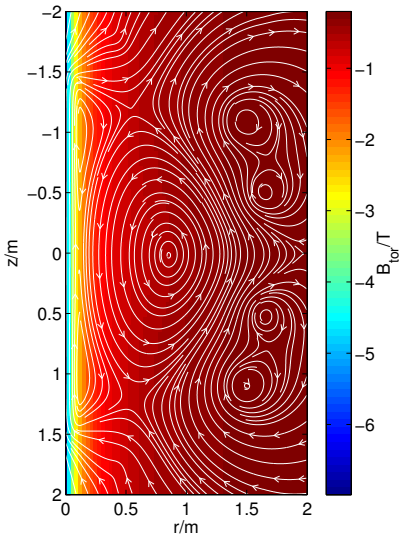

Figure 1.6: Magnetic field of MAST, with toroidal magnetic field in colour and the poloidal component of magnetic field lines overlaid in white. The central, primary coil is visible on the left, and the cross sections of the four poloidal field coils are visible on the right.

1.3.1 Turbulent Transport

One of the most significant challenges in achieving fusion energy is the reduction of radial, cross-field transport of particles and heat in the near-edge and SOL regions, thereby isolating the core, burning plasma and minimising its interaction the vessel wall and divertors. Cross field transport in the edge region occurs largely as a result of turbulent fluctuations characterised by highly irregular flows and a cascade of energy from large to small scales. Turbulent fluctuations arise from saturation of the drift wave and interchange instabilities present on the outboard side of the torus, which are driven by magnetic curvature and pressure gradients perpendicular to the magnetic field direction. These instabilities are suppressed on the inner edge where pressure gradients and curvature are oppositely directed. The turbulent fluctuations have amplitudes as large as 5-100% of the background fields in number density, electrostatic potential and electron temperature, with significantly smaller fluctuations occurring in the magnetic field [Zweben et al., 2007]. Observations of these fluctuations have been reported in for example [Nedospasov, 1992], and the universality of fluctuations demonstrating the turbulent cascade between devices has been reported in [Chen, 1965]. The power spectrum of the fluctuations has since been shown to be flat up to 10-100Hz, with a power law exponent in the region of

1-4 for shorter timescales [Pedrosa et al., 1999].

Associated with these turbulent fluctuations are intermittent, coherent filamentary structures known as "blobs". Polarising drifts within these blobs can lead to radial $\mathbf{E} \times \mathbf{B}$ cross-field transport from the confined near-edge region, where these structures form, to the SOL [Terry et al., 2003]. These blobs can account for 50% of particle transport [Boedo et al., 2001] to the vessel wall and divertor.

Turbulence in the edge region can be categorised in two regimes. The first, the low-confinement "L-mode", is characterised by relatively shallow gradients in number density and temperature, and strong fluctuations. The second, the high-confinement "H-mode", was discovered serendipitously in the ASDEX tokamak [Wagner et al., 1982], and is characterised by steep density and temperature profiles in the edge region, and significantly reduced turbulence due to the formation of shear flows [Biglari et al., 1990]. The steep gradients of the H-mode form a radial transport barrier, and the formation of coherent filamentary structures (blobs) is reduced. However, steep gradients can trigger edge-localised modes (ELMs): an instability of the MHD peeling-ballooning modes [Wilson et al., 2006; Connor, 1998] which leads to a rapid spill of hot, dense plasma into the SOL.

Although significant progress in the understanding of the role of edge turbulence in fusion plasma confinement has been made over the last few decades, there still remains uncertainty in the dimensionless scaling of the fluctuations, the causes of intermittency, the reason for the L-H transition, the relationship between shear flows and turbulence, and the transport processes which determine particle and heat fluxes on the vessel wall [Zweben et al., 2007].

1.3.2 Blobs

1.3.2.1 Theoretical Model

In the far scrape-off layer, the transport of blob plasma to the tokamak wall is governed, in the classical picture, by charge polarisation as a result of a net force $\mathbf{F}$ [Krasheninnikov, 2001]. The electrons and ions undergo $\mathbf{F} \times \mathbf{B}$ drift in opposite directions, which results in polarisation on the condition that $\mathbf{B}/B \cdot \nabla \times \mathbf{F} \neq 0$. Charge polarisation by this mechanism results in a poloidal electric field inside the blob, which in turn leads to $\mathbf{E} \times \mathbf{B}$ drift in the direction of the force $\mathbf{F}$. The dominant force may vary between scales and devices, but in general for tokamaks, $\nabla \mathbf{B}$ and magnetic curvature forces are most significant. Both these forces lead to radial transport of blob plasma towards the outer wall. This model for blob propagation is displayed in Figure 1.7.

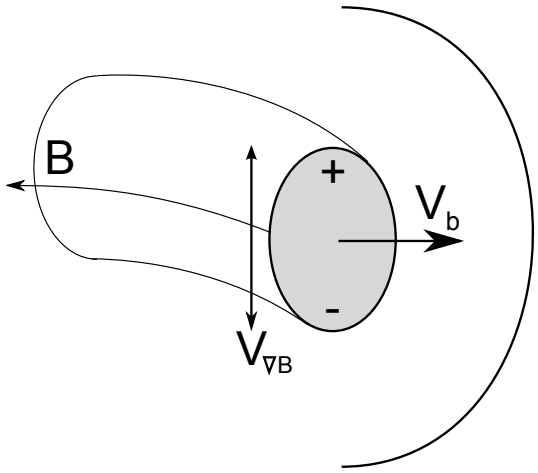

Figure 1.7: Geometry of blobs as in the Krasheninnikov model. Polarising $\nabla\mathbf{B}$ drifts $v_{\nabla B}$ and effective gravities cause charge polarisation of blob plasma. The resulting electric field causes radial $\mathbf{E}\times\mathbf{B}$ drift v_b of blob plasma towards the vessel wall.

In addition to $\nabla\mathbf{B}$ and curvature which dominate for toroidal plasmas, the centrifugal force in a rapidly rotating plasma, and the neutral wind frictional force [Krasheninnikov and Smolyakov, 2003], have been shown in experiment to drive blob transport in linear devices. Each of the forces described here may be represented as an effective gravity, where $\mathbf{F} = nm_i\mathbf{g}$ [Krasheninnikov et al., 2008]. For example, for the curvature force $g \sim c_s^2/R_c$, and for the neutral wind frictional force $g =\sim (N\mathbf{V})_{\text{bulk}}(K_{\text{bulk}}-K_{\text{wall}})$, where $N\mathbf{V}$ is the neutral particle flux, and K is the neutral-ion collision rate.

This model of blob propagation, i.e. charge polarisation due to an effective gravity, followed by $\mathbf{E}\times\mathbf{B}$ convection, is a new application of a similar phenomenon — the Rosenbluth-Longmire interchange instability [Rosenbluth and Longmire, 1957]. However, here we apply the instability to isolated filaments rather than sinusoidal density perturbations.

This model informs the basic properties of a blob in a tokamak, which are as follows [D'Ippolito et al., 2011]:

1. it has a single-peaked density distribution, with peak density much higher than the surrounding background plasma and fluctuations within the background;

2. it is aligned parallel to the magnetic field $\mathbf{B}$, and variation along the field is much weaker than in the perpendicular direction, with blobs forming an extended, filamentary structure;

3. it has a convective $\mathbf{E}\times\mathbf{B}$ velocity component, usually the result of a charge-

polarising force, with corresponding potential and dipole vorticity.

However, we note that this is not a robust definition. Blobs which do not satisfy some of these conditions have been measured in experiments.

A simple theoretical model of blob dynamics in the fluid regime can be derived using conservation of charge and density. First we split our definition of current into components parallel and perpendicular to the **B** field. We separate also the drift due to charge polarising force F such that

$$\mathbf{J}_\perp = \frac{1}{B^2}\mathbf{F}\times\mathbf{B} + \mathbf{J}_{\perp\mathrm{pol}}. \tag{1.93}$$

The perpendicular component of the divergence is then

$$\nabla_\perp\cdot\mathbf{J}_\perp = \frac{1}{B}\mathbf{b}\cdot\nabla\times\mathbf{F} + \nabla_\perp\cdot\mathbf{J}_{\perp\mathrm{pol}} \tag{1.94}$$

where $\mathbf{b} = \mathbf{B}/|B|$. From the charge conservation equation $\nabla\cdot\mathbf{J} = 0$ and the current density components above,

$$-\nabla_\perp\mathbf{J}_{\perp\mathrm{pol}} = \nabla_\parallel J_\parallel + \frac{1}{B}\mathbf{b}\cdot\nabla\times\mathbf{F} \tag{1.95}$$

$$\nabla\cdot\frac{d}{dt}\left(\frac{nm_i}{B^2}\nabla_\perp\Phi\right) = \nabla_\parallel J_\parallel + \frac{c}{B}\mathbf{b}\cdot\nabla\times\mathbf{F}, \tag{1.96}$$

where Φ is the electrostatic potential. The evolution of the overdense region, the blob, can at the lowest order be written as the following equation, which arises from mass continuity:

$$\frac{dn}{dt} \equiv \frac{\partial n}{\partial t} + \mathbf{v}_E.\nabla n \approx 0, \tag{1.97}$$

where $\mathbf{v}_E$ is the $\mathbf{E}\times\mathbf{B}$ drift velocity $\mathbf{v}_E = (\mathbf{b}\times\nabla\Phi/B)$.

The magnitude of the electric field induced by the force F is obtained, in the case of blobs in the far SOL, by considering the balance between the current source as a result of the charge polarising drift $\mathbf{F}\times\mathbf{B}$ and any parallel and perpendicular losses in the electrical circuit connecting the blob to the vessel wall. In a tokamak SOL, the parallel currents are dependant upon the sheath and plasma resistivity, magnetic geometry, and other parameters.

In the case of Gaussian density profiles in the perpendicular direction, charge polarising force arising from toroidal curvature and $\nabla\mathbf{B}$, and linearised sheath-connected parallel current closure $J_\parallel = ne^2c_s\Phi/T_e$, the solution to Equations 1.96 and 1.97 yields

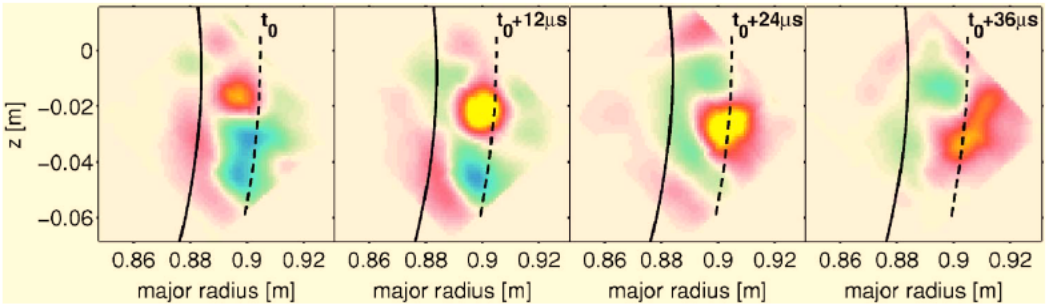

Figure 1.8: Observation of a blob in Alcator C-mod using D_α emission. Red and yellow correspond to positive density fluctuations, and green and blue to negative. The separatrix is indicated by a solid black line, and the projection of the limiter edge by a dashed line. Reproduced from [Grulke et al., 2006].

$$v_b = c_s \left(\frac{L_\parallel}{R}\right)\left(\frac{\rho_s}{\delta}\right)^2 \tag{1.98}$$

where c_s is the sound speed, ρ_s the corresponding ion gyro-radius, R and $L_\parallel$ are the radius of curvature and parallel connection length, and δ is the blob radius.

Although useful for approximating the behaviour of blobs in the far scrape off layer, the physics of blobs creation, detachment and propagation at the separatrix are beyond the scope of this model. These phenomena are described in more detailed in Chapter 5.

1.3.2.2 Observations

Observations of blobs in experiment are widespread in both fusion and basic plasma physics devices. Blobs have been directly imaged in, for example, the DIII-D [Boedo et al., 2003], Alcator C-mod [Grulke et al., 2006], NSTX [Myra et al., 2006], ASDEX Upgrade [Nold et al., 2010] and MAST [Kirk et al., 2006] tokamaks and in other laboratory experiments, for example [Windisch et al., 2011], among many others. Each of these observations demonstrate the intermittent, bursty nature of blob transport in time and space, which arises from edge turbulence. Crucially, radially convecting blobs have been shown to generate an order of unity fraction of the particle flux in the SOL [Boedo et al., 2001; Xu et al., 2005], implying that a more complete model of blobs is necessary for understanding heat and particle fluxes to the wall of fusion reactors. Figure 1.8 shows an observation of a propagating blob in the Alcator C-mod tokamak.

A variety of blob properties have been measured for blobs propagating the SOL, including a skewed, non-Gaussian probability density function (e.g. [Xu et al.,

2005] for TEXTOR, [Gonçalves et al., 2005] for JET), a necessary condition for the detection of intermittency and blobs; radial speed (e.g. [Boedo et al., 2001] for DIII-D); blob size (e.g. [Myra et al., 2006] for NSTX); birth rate (e.g. [Devynck et al., 2005] for Tore Supra); scaling of blob properties under differing plasma conditions (e.g. [Terry et al., 2003] for Alcator C-mod); and particle and heat flux associated with blobs (e.g. [Kirk et al., 2006] for MAST). Specifically, important results from observation of blob characteristics include:

- The absolute amplitude, electron temperature and radial velocity decrease with the radial coordinate [Boedo et al., 2003; Rudakov et al., 2005], suggesting the blob population consists of small blobs which are difficult to detect near the birthing region, but large and dominant out into the SOL and near the wall;
- There is no simple relationship between blob size and radial velocity. A combination of radial velocities associated with blobs of a given size for various tokamaks is shown in Figure 1.9;
- Blob properties compared between H-mode plasmas and L-mode plasmas vary with the device. In DII-D [Boedo et al., 2001] blob amplitude was reduced in the H-mode, and blob frequency was seen to be reduced in the H-mode of NSTX [Myra et al., 2006]. However, blob statistics were similar between H- and L-modes in ASDEX-Upgrade [Antar et al., 2008]. This demonstrates that blob scalings are best measured within a single device rather than with combined studies, until a more complete model of blob physics arises.

1.3.2.3 Simulations

Models for blob transport and evolution have principally focused on fluid and multi-fluid descriptions, and have had significant success modelling a blob's structure, the instabilities driving changes in that structure, and how these relate to the stability of a propagating blob. Many studies have been conducted which test for the dependence of blob structure and coherence as a function of the poloidal blob size; see, for example [D'Ippolito et al., 2002; Aydemir, 2005; Russell et al., 2004; Garcia et al., 2005; Yu et al., 2006; Higgins et al., 2012]. These simulations show that some blobs are unstable, and others propagate as coherent structures over relatively large distances. Three regimes are shown to exist, with their boundaries dependent on the dimensionless blob size $\hat{\delta} = \delta_b/\delta_*$, where δ_b is the blob radius, and the critical blob size $\delta_* = \rho_s^{4/5} L_\parallel^{2/5}/R^{1/5}$. These regimes are:

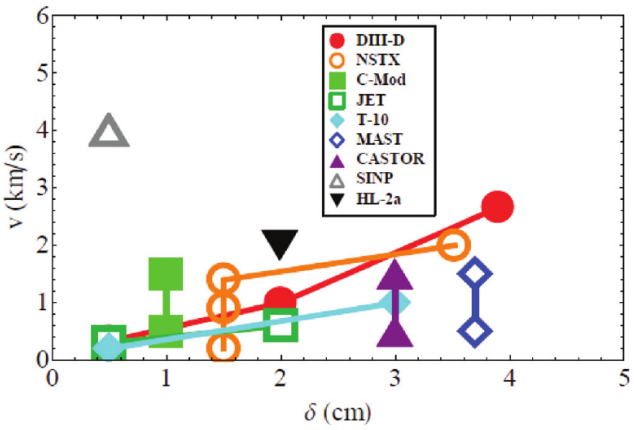

Figure 1.9: Radial blob speed v against blob size δ for several tokamaks. Note that results have not been differentiated by the differing definitions and analysis methods used by each study. (Reproduced from [D'Ippolito et al., 2011])

- $\hat{\delta} < 1$ — Stability for small-scale blobs is determined by the Kelvin-Helmholtz instability;
- $\hat{\delta} \sim 1$ — Blobs are the most stable, propagating radially with the most coherence;
- $\hat{\delta} > 1$ — Stability for large-scale blobs is determined by the curvature-driven interchange instability.

Simulations demonstrating each of these three regimes are shown in Figure 1.10. The interplay is evident from Equation 1.96:

$$\nabla \cdot \frac{d}{dt}\left(\frac{nm_i}{B^2}\nabla_\perp \Phi\right) = \nabla_\parallel J_\parallel + \frac{1}{B}\mathbf{b}\cdot\nabla\times\mathbf{F}. \tag{1.99}$$

At small scales, the vorticity advection term on the left-hand side is dominant. At large scale, the sheath conductivity ($J_\parallel$) and effective gravity due to curvature are dominant. The long lifetime of blobs with $\hat{\delta} \sim 1$ suggests these blobs will be those most commonly observed, which is consistent with experiment to within an order of magnitude.

The structure of unstable blobs has received theoretical attention via simulations, but little experimental data is available. In the case of small-scale, KH-dominated blobs, we see disruption into a mushroom shape. For large, curvature-dominated blobs, we see break-up into Rayleigh-Taylor fingers. The lifetime of these blobs is hence determined by the growth rate of these two instabilities. Simulations have shown that blobs can be stabilised against these secondary instabilities by

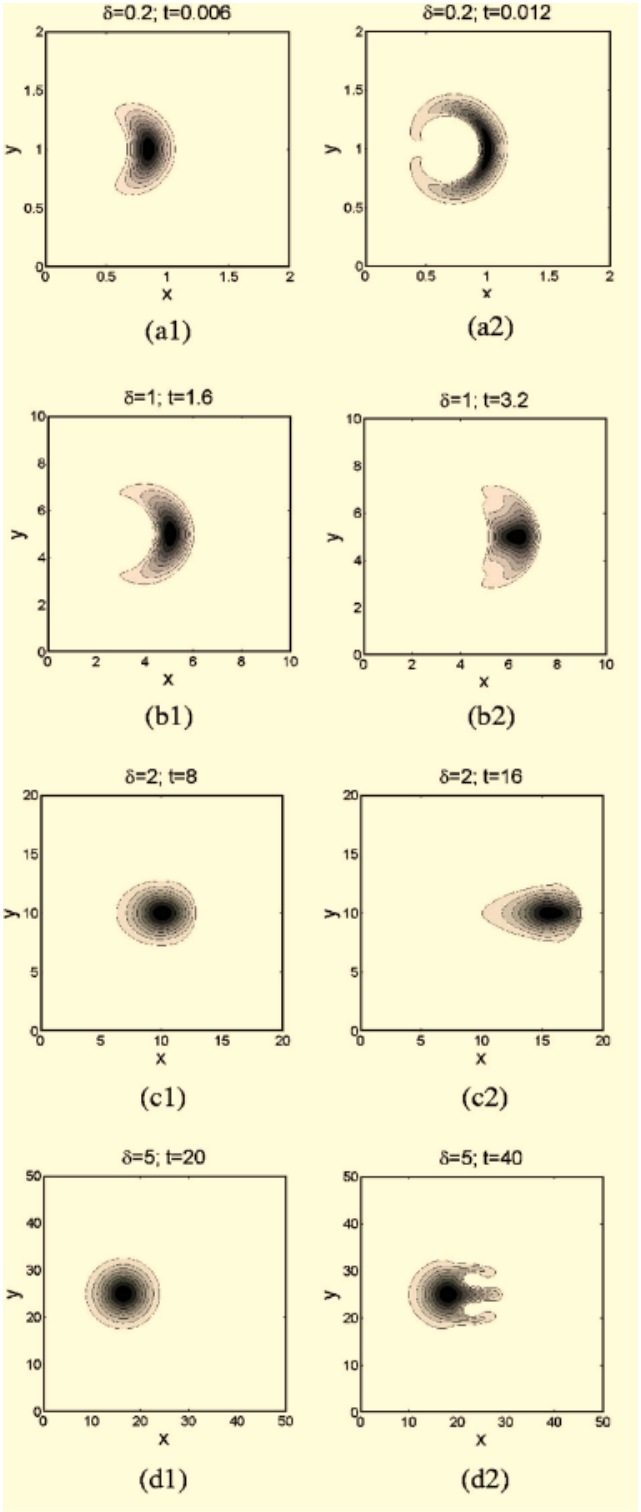

Figure 1.10: Comparison of the evolution of SOL blobs of different sizes $\hat{\delta} = 0.2, 1, 2, 5$ from top to bottom. The smallest blobs quickly develop a mushroom shape as a result as the K-H instability arising from velocity shear. The largest blobs develop fingers as a result of the curvature-driven interchange instability. Intermediate blobs for which $\hat{\delta} \sim 1$ are most stable. Reproduced from [Yu et al., 2006].

including: higher background density [D'Ippolito and Myra, 2003], larger sheath resistivity [Myra, 2007; D'Ippolito and Myra, 2003], and larger viscosity [Aydemir, 2005; Garcia et al., 2006].

1.3.2.4 Blob Creation

Intermittent detachment of coherent filamentary structures such as blobs and ELMs occurs as a results of the saturation of edge instabilities, with subsequent radial transport due to charge polarisation as discussed in Section 1.3.1. Blob creation differs between three important regimes: no shear, weak shear, and strong shear [D'Ippolito et al., 2011]. These sheared flows arise from momentum transport by Reynold's stress and blobs, or by transport barrier formation.

With no shear present, the curvature driven interchange instability results in the development of radial streamers [Russell et al., 2007]. These may become charge polarised and propagate in the same manner as blobs, described in [Krasheninnikov, 2001]. In this case, blobs are generated in the region of maximum linear growth rate, or equivalently at the maximum of the logarithmic pressure gradient $-\nabla(\ln p)$.

In the low-confinement L-mode with weak shear, the dominant mechanism for blob creation is again the curvature driven interchange instability [Bisai et al., 2005], However, here the weak shear can result in the break up of radial streamers into detached blobs. Similarly, larger blobs can be split into smaller ones by the action of shear flows. Streamers will break up on the condition that the shearing time must be shorter than the radial convection time [Bisai et al., 2005], or equivalently

$$\frac{\partial v_y}{\partial x}\delta_x^2 > v_x\delta_y, \tag{1.100}$$

where $v_{x,y}$ are the radial and poloidal velocity fields respectively, and $\delta_{x,y}$ are the blob sizes in each dimension. In the limit of isotropic blobs $\delta_x = \delta_y$ and with blob velocity $v_x = \gamma\delta$, where γ is the growth rate of the instability generating the turbulence, this relation reduces to

$$\frac{\partial v_y}{\partial x} > \gamma. \tag{1.101}$$

As with radial streamers in the regime with no shear, the blob birth zone is the region of maximum pressure gradient [Myra et al., 2006], with its position dependent upon the density [Terry et al., 2005]. For sufficiently high densities, the creation zone can lie inside the separatrix [Cheng et al., 2010]. The appearance of blobs within the LCFS of L-mode plasmas means that, in these cases, blobs are born by gradients, and not by physics associated with open field lines.

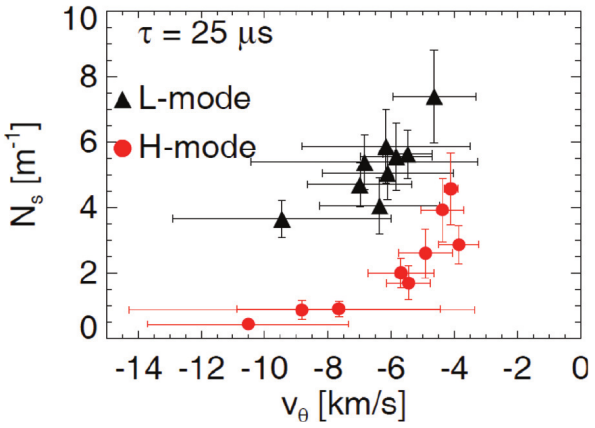

Figure 1.11: Linear spatial density of structures N_s in the NSTX tokamak with characteristic timescale $\tau = 25\mu s$ 1-2 cm outside the separatrix as a function of poloidal velocity v_θ for the L-mode and H-mode, where each point represents a different shot. Note the significantly reduced density of structures in the H-mode compared to the L-mode. Reproduced from [Agostini et al., 2007].

In the high-confinement H-mode, zonal flows with strong shear boundaries are self-generated by turbulence. These strong shears suppress the transport of blobs compared to the L-mode, either by trapping them in the shear layer [Myra et al., 2011] or by blobs being torn apart by the shear itself. The reduced production of blobs in the H-mode compared to the L-mode is demonstrated in Figure 1.11. Despite this suppression, there is experimental evidence to suggest that the strong shear boundary can play a role in blob creation in tokamaks such as JET [Xu et al., 2009], ASDEX-U [Nold et al., 2010] and TORPEX [Furno et al., 2008], where blobs are born in the sheared flow layer. In the H-mode, periods of intermittent blob creation are interrupted by violent radial transport events known as edge-localised modes (ELMs), for which filaments generated by the interchange instability spill large volumes of hot plasma in the SOL.

1.3.2.5 Generation Rates

The rate of intermittent blob creation, which is a relatively rare event, has been estimated by considering the size, and therefore particle content, of blobs compared to the observed particle flux across the separatrix [Krasheninnikov, 2001]. For blob particle content N_b and particle flux Φ, the blob creation rate is $F_b = N_p/\Phi$ which, for typical parameters, gives a creation rate $F_b \sim 10^6 \mathrm{s}^{-1}$. We can further characterise blob creation by considering the waiting time between events τ_w, and the

"packing fraction", or the fractional area perpendicular to the magnetic field occupied by blobs, estimated as

$$f_p \approx \sum_\tau \tau \frac{dN_\tau}{dt} \tag{1.102}$$

for timescales τ and number of blobs observed per unit time dN_τ/dt [Spolaore et al., 2004; Agostini et al., 2007], or equivalently

$$f_{pn} \equiv \frac{\bar{n}_e}{n_b} = \frac{2\delta_b}{\Delta x} = \frac{\tau_b}{\tau_w}, \tag{1.103}$$

where $\bar{n}_e$ is the time and poloidally averaged electron density, $n_b = \bar{n}_e(x_b)$ is the average blob electron density at birth location x_b, and $\Delta x = v_{xb}\tau_w$ is the spacing between consecutive blobs. In the ideal case of equally spaced square-pulse blobs in the highly intermittent limit, the packing fraction is related to the skewness of the density fluctuation PDF S by $f_p \sim 1/S^2$. Since shear flows have been shown to reduced the number of blobs entering the SOL, the packing fraction should decrease as shear is increased. Observations have reported packing fractions either directly, as in [Agostini et al., 2007] and indirectly via measurements of density fluctuation skewness or burst rates and duration as in [Müller et al., 2007; Furno et al., 2008; Nanobashvili et al., 2009]. Radial profiles of skewness and packing fraction have been reported in observation [Agostini et al., 2007] and using simulations [Russell et al., 2007]. The radial dependence of the packing fraction has been measured for NSTX [Agostini et al., 2007], and shows a peak packing fraction of 0.2 in the far SOL.

1.3.2.6 Gyro-scale Blobs

In this thesis, we study the properties of blob which exist on ion gyro-scales in order to address their role in cross-field particle and heat transport in tokamaks. We first introduce the numerical tools developed for this study in Chapter 2. We then present a study of the phenomena unique to the evolution of ion gyro-scale blobs in 3, and follow with a study of their role in heat transport in Chapter 4. Finally, we discuss the statistics of their creation in Chapter 5.

Chapter 2

Numerical Methods: Hybrid Particle-in-Cell Codes

2.1 Introduction

Analytic solutions in plasma physics are valid only under specific limits, and hence are highly specialised. If the physics we intend to study is non-linear, we must seek solutions to the full non-linear equations which govern plasma dynamics. In these cases analytic solutions are generally not tractable, and we are required to obtain solutions using numerical methods. The wide range of spatio-temporal scales over which plasmas can and do exist means that a wide variety of numerical tools are required, and are often tailored to the specific problem being studied. The scales, plasma parameters, model assumptions and the phenomena we intend to study inform our choice of simulation method.

In a tokamak, three important length scales indicate the level of approximation required for simulations of fusion plasmas. In descending order, these are the macroscopic length scale L, defined by either the size of the device or the background gradients, and the ion and electron gyro-radii $\rho_{i,e}$. Relevant timescales, in descending order, include the collision timescale t_ν, the ion cyclotron period t_{Ω_i}, and the electron cyclotron period t_{Ω_e}. For global simulations, for which $L \gg \rho_i \gg \rho_e$ and $t_\nu > t \gg t_{\Omega_i}$, individual particle gyrations may be neglected, and fluid models for which we average over particle properties are appropriate. If we wish to simulate microscopic regions of the tokamak, for which our macroscopic lengthscale is defined by local inhomogeneities, we may find $L \gtrsim \rho_e$ and $t \gtrsim t_{\Omega_e}$. In these cases, relevant to core microinstabilities, we require fully kinetic particle-in-cell or Vlasov solvers. Intermediate scales for which $L \sim \rho_i$ and $t \sim t_{\Omega_i}$, which occur for gradients and

turbulent structures in the edge region, require hybrid treatments such as hybrid particle-in-cell codes and gyro-kinetics. For this work, we will be making use of a hybrid particle-in-cell code with application to ion gyro-scale inhomogeneities in the near-edge region. This code is described in detail in this Chapter.

2.2 Particle-in-Cell Codes

2.2.1 Theoretical Basis

To understand the theory that underlies particle-in-cell codes, we first consider the Liouville equation which governs the evolution of this phase space density, or distribution function f:

$$\frac{df}{dt} = \frac{\partial f}{\partial t} + \sum_{i=1}^{n} \left(\frac{\partial f}{\partial q_i} \dot{q}_i + \frac{\partial f}{\partial p_i} \dot{p}_i \right) = 0 \tag{2.1}$$

where q_i are the canonical coordinates and p_i are the conjugate momenta of the Hamiltonian system. With appropriate substitution of the Lorentz force and the plasma approximation $\mathbf{E} = \langle \mathbf{E} \rangle + \delta \mathbf{E}$, this equation becomes the Vlasov equation. Since the convective derivative df/dt is zero in the absence of collisions, this implies that the phase space density is constant along the particle trajectories. This principle is known as Liouville's theorem.

In a particle-in-cell code, the initial distribution function is sampled by a large number of "pseudoparticles". Each pseudoparticle, in the simplest form, represents a delta function in phase space such that the full distribution function is given by

$$f(\mathbf{x}, \mathbf{v}) = \sum_{k} \delta(\mathbf{x} - \mathbf{x}_k)(\mathbf{v} - \mathbf{v}_k). \tag{2.2}$$

This sampling of the phase space results in a significant reduction in computational load over codes which directly solve the Vlasov equation for a six-dimensional phase space on a regular grid. From Liouville's theorem, pseudoparticles remain on contours of constant phase space as the code advances, as shown in Figure 2.2.1, following the trajectories of the system governed by the Lorentz force. Hence, by sampling the initial phase space density, we can follow trajectories of pseudoparticles to reconstruct the phase space density at later times. This carries the advantage of allowing us to concentrate comparatively more computational resources in those regions of the phase space that most interest us. For example, we might initialise many pseudoparticles in a region of phase space in the far tail of a Gaussian distribution to study the evolution of high energy particles, or near a bump on the tail

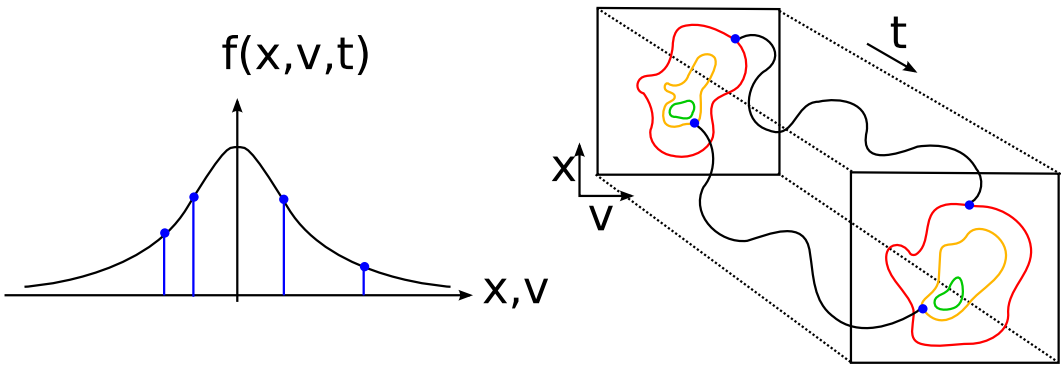

Figure 2.1: Illustration of a PIC code as a Vlasov solver. Left: pseudoparticles (blue) sample the continuous distribution function f in phase space. Right: Coloured contours of f in phase space follow the trajectories (black) of pseudoparticles as they evolve.

to study associated instabilities such as the two-stream instability.

If the plasma approximation holds, i.e. if the number of particles within the Debye sphere is large, electrons are able to effectively shield particles from potentials with centres further than the Debye length. In the case that the length scale of the plasma is much larger than the Debye length, this shielding implies that the trajectories of the system are dominated by global electric and magnetic fields caused by collective particle behaviour, rather than by individual particle collisions. For this reason, we can represent the electromagnetic fields on a discrete grid with cell size $\Delta x \gtrsim \lambda_D$. This significantly reduces computation over methods which require the calculation of the force on each particle exerted by all others.

2.2.2 Algorithm

A particle-in-cell code relies on the interaction of each pseudoparticle, acted upon by the Lorentz force, with a grid upon which we evolve the electromagnetic fields **E**, **B** and **J** using Maxwell's equations. The cycle of a single time step is as follows:

1. Integrate the equations of motion to accelerate and move particles:

$$F_i \rightarrow v_i \rightarrow x_i$$

2. Take moments of the particle distribution function calculate number and current densities:

$$(x, v)_i \rightarrow (\rho, J)_j$$

3. Integrate the field equations on the grid:

$$(\rho, J)_j \rightarrow (E, B)_j$$

4. Interpolate fields from the grid to the particle positions:

$$(E, B)_j \rightarrow F_i$$

5. Return to step 1 to begin a new time step.

where variables i are at particle positions, and j are on the grid and F_i is the Lorentz force on particle i.

The field equations to be solved for this method are Faraday's Law and Ampère's Law, respectively given by

$$\frac{\partial \mathbf{B}}{\partial t} = -\nabla \times \mathbf{E} \tag{2.3}$$

$$\frac{\partial \mathbf{E}}{\partial t} = \frac{1}{\varepsilon_0 \mu_0} \nabla \times \mathbf{B} - \frac{1}{\varepsilon_0} \mathbf{J} \tag{2.4}$$

where $\mathbf{E}$ is the electric field, $\mathbf{B}$ the magnetic field and $\mathbf{J}$ is the current density. We must also define the number density and current density as moments of the distribution function for the particles in the simulation:

$$n_\alpha = \int f_\alpha d^3 v, \tag{2.5}$$

$$\mathbf{J}_\alpha = \int q_\alpha \mathbf{v} f_\alpha d^3 \mathbf{v}, \tag{2.6}$$

for a species α, where q_α is the charge of particles of that species. Finally, we require the Lorentz force law to determine how the particles are accelerated by the fields:

$$m_\alpha \frac{d\mathbf{v}_\alpha}{dt} = q_\alpha (\mathbf{E} + \mathbf{v}_\alpha \times \mathbf{B}). \tag{2.7}$$

This can be modified for relativistic particles for which the relativistic mass m is no longer constant. In such a case, $m = \gamma m_0$ using the Lorentz factor $\gamma = 1/\sqrt{1 - v^2/c^2}$ and the rest mass m_0. However, using this formulation of the Lorentz factor is problematic because numerical errors may lead to a speed greater than or equal to the speed of light. Instead, we define a relativistic velocity $\mathbf{u} = \gamma \mathbf{v}$, so that $m\mathbf{v} = m_0 \mathbf{u}$ and $\gamma = \sqrt{1 + u^2/c^2}$. Hence, the Lorentz force equation becomes

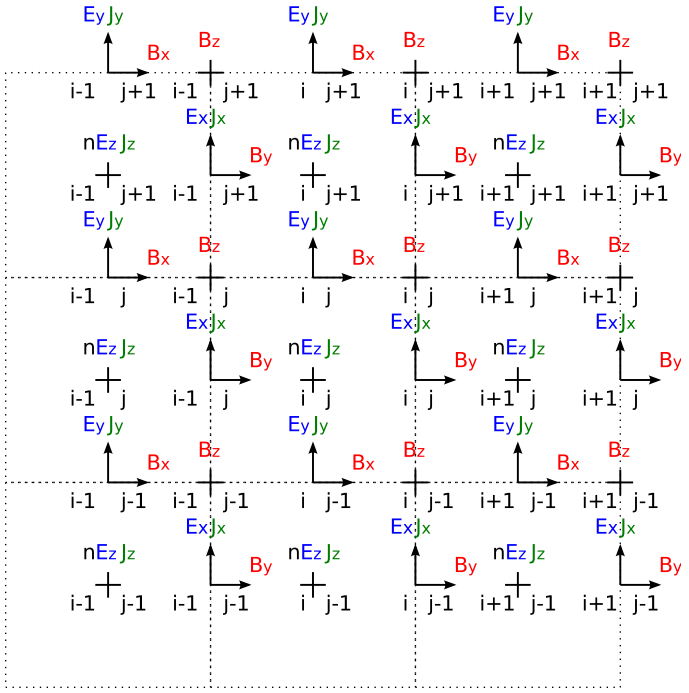

Figure 2.2: Yee grid showing the field staggering for a 2D simulation. The dotted lines mark the cell boundaries. The letter i denotes the cell number in the x direction, and j the cell number in the y direction.

$$\frac{d\mathbf{u}}{dt} = \frac{q}{m_0}(\mathbf{E} + \frac{\mathbf{u}}{\gamma} \times \mathbf{B}). \tag{2.8}$$

The fields, including the electric and magnetic fields, current and number density, are defined on a staggered grid called the Yee grid [Yee, 1966]. For a three dimensional simulation, the Yee grid is a cube with the electric field components defined at the centre of the faces, and the magnetic field components defined along the edges, or vice versa. Electric field and current density components are displaced half a cell from the cell's centre in direction of that field component. For example E_x is displaced half a cell in the x direction. Magnetic field components are displaced half a cell in every orthogonal direction. For example B_x is displaced half a cell in the y and z directions. The number density and temperature are cell centred. The Yee grid for a 2D simulation is shown in Figure 2.2. The use of this grid simplifies the integration of the electromagnetic fields.

Although a time stagger is common for particle-in-cell codes, for which the electric field is known at the full time step and the magnetic field at the half time step as in [Birdsall and Langdon, 2005], here we seek a time-centred integration

method for which both electric and magnetic fields are known at the full time step. Applying a time-centred finite difference technique to the field equations (Equations 2.3 and 3.6), we arrive at the following difference equations. First, we update both fields to the half time step:

$$\mathbf{E}^{n+\frac{1}{2}} = \mathbf{E}^{n} + \frac{\Delta t}{2}(c^2 \nabla \times \mathbf{B}^{n} - \mathbf{J}^{n}) \tag{2.9}$$

$$\mathbf{B}^{n+\frac{1}{2}} = \mathbf{B}^{n} - \frac{\Delta t}{2}(c^2 \nabla \times \mathbf{E}^{n+\frac{1}{2}}) \tag{2.10}$$

The particle pusher, in which we integrate the equations of motion for the pseudoparticles, is called after this half update. The particle motions are used to calculate the current $\mathbf{J}^{n+1}$ as discussed below. Following that, the fields are updated to the full time step using:

$$\mathbf{B}^{n+1} = \mathbf{B}^{n+\frac{1}{2}} - \frac{\Delta t}{2}(c^2 \nabla \times \mathbf{E}^{n+\frac{1}{2}}) \tag{2.11}$$

$$\mathbf{E}^{n+1} = \mathbf{E}^{n+\frac{1}{2}} + \frac{\Delta t}{2}(c^2 \nabla \times \mathbf{B}^{n+1} - \mathbf{J}^{n+1}) \tag{2.12}$$

where n represents the time step number. The initial fields required are $\mathbf{B}^n$ and $\mathbf{E}^n$.

Knowledge of the fields on the grid allows us to accelerate the particles using the Lorentz force in the particle pusher. This stage uses a leap frog method, which staggers the particle positions and velocities in time. Initially we have $\mathbf{u}^{n-\frac{1}{2}}$ and $\mathbf{x}^n$, and as the code progresses we know the speed at the half time step, and the position at the full time step.

To solve the Lorentz force equation for each of the particles, we require the following difference equation:

$$\frac{\mathbf{u}^{n+\frac{1}{2}} - \mathbf{u}^{n-\frac{1}{2}}}{\Delta t} = \frac{q}{m_0}\left(\mathbf{E}^{n}(\mathbf{x^n}) + \frac{\mathbf{u}^{n}}{\gamma^{n}} \times \mathbf{B}^{n}(\mathbf{x^n})\right). \tag{2.13}$$

This formulation presents a problem, since we do not know the particle velocities or magnetic field at the full time step. To find the velocity at the full time step, we take the mean of the velocities half a time step before and after that point, as follows:

$$\frac{\mathbf{u}^{n+\frac{1}{2}} - \mathbf{u}^{n-\frac{1}{2}}}{\Delta t} = \frac{q}{m_0}\left(\mathbf{E}^n(\mathbf{x^n}) + \frac{\mathbf{u}^{n+\frac{1}{2}} + \mathbf{u}^{n-\frac{1}{2}}}{2\gamma^n} \times \mathbf{B}^n(\mathbf{x^n})\right). \tag{2.14}$$

Then we define two velocities $\mathbf{u}^+$ and $\mathbf{u}^-$ using:

$$\mathbf{u}^{n-\frac{1}{2}} = \mathbf{u}^- - \frac{q}{2m_0}\mathbf{E}^n\Delta t \tag{2.15}$$

$$\mathbf{u}^{n+\frac{1}{2}} = \mathbf{u}^+ + \frac{q}{2m_0}\mathbf{E}^n\Delta t \tag{2.16}$$

Using these velocities, we can rewrite the Lorentz force law as

$$\frac{(\mathbf{u}^+ - \mathbf{u}^-)}{\Delta t} = \frac{q}{2\gamma^n m_0}(\mathbf{u}^+ + \mathbf{u}^-) \times \mathbf{B^n} \tag{2.17}$$

where γ is defined at $\mathbf{u}^-$. This equation constitutes a rotation of $\mathbf{u}$ without a change in the magnitude. For a coordinate j we then define a quantity τ_j as

$$\tau_j = \frac{q\Delta t}{2\gamma m_0}B_j \tag{2.18}$$

which allows us to rewrite the components of the Lorentz force equation as follows:

$$u_x^+ - u_x^- = \tau_y(u_z^+ + u_z^-) - \tau_z(u_y^+ + u_y^-) \tag{2.19}$$

$$u_y^+ - u_y^- = \tau_z(u_x^+ + u_x^-) - \tau_x(u_z^+ + u_z^-) \tag{2.20}$$

$$u_z^+ - u_z^- = \tau_x(u_y^+ + u_y^-) - \tau_y(u_x^+ + u_x^-) \tag{2.21}$$

We then use a matrix method to solve this set of equations for $\mathbf{u}^+$, given $\mathbf{u}^-$ and τ, i.e.

$$\vec{\mathbf{B}}\begin{pmatrix} u_x^+ \\ u_y^+ \\ u_z^+ \end{pmatrix} = \vec{\mathbf{C}}\begin{pmatrix} u_x^- \\ u_y^- \\ u_z^- \end{pmatrix} \tag{2.22}$$

$$\begin{pmatrix} u_x^+ \\ u_y^+ \\ u_z^+ \end{pmatrix} = \vec{\mathbf{B}}^{-1}\vec{\mathbf{C}}\begin{pmatrix} u_x^- \\ u_y^- \\ u_z^- \end{pmatrix} \tag{2.23}$$

Hence, the velocity can be advanced using the rotation matrix $\vec{\mathbf{A}} = \vec{\mathbf{B}}^{-1}\vec{\mathbf{C}}$. This gives us a three step process for acceleration as follows:

1. Update the velocity by a half acceleration according to the electric field:

$$\mathbf{u}^{-} = \mathbf{u}^{n-\frac{1}{2}} + \frac{q}{2m_0}\mathbf{E}^n \Delta t \tag{2.24}$$

2. Rotate the velocity according to the magnetic field:

$$\mathbf{u}^{+} = \vec{\mathbf{A}}\mathbf{u}^{-} \tag{2.25}$$

3. Update the velocity to the final point with a second half acceleration:

$$\mathbf{u}^{n+\frac{1}{2}} = \mathbf{u}^{+} + \frac{q}{2m_0}\mathbf{E}^n \Delta t \tag{2.26}$$

Next, to complete the computation of the fields, we need to calculate the current density on the grid, $\mathbf{J}^{n+1}$ to calculate the electric field in Equation 2.12. To compute components of the current which lie within the plane of the simulation domain, e.g. J_x and J_y in a 2D grid, we use the Villasenor and Buneman scheme [Villasenor and Buneman, 1992]. For this method, we also solve the charge continuity equation, given by

$$\frac{\partial \rho}{\partial t} = \nabla \cdot \mathbf{J} \tag{2.27}$$

where ρ is the charge density. The change in the charge density is calculated from the charges added and subtracted from cells when a particle passes a cell boundary.

After the particle push, the particles are advanced a further half time step using the updated velocities at timestep $n+1$. This gives the particle position at $t+\frac{3dt}{2}$. Using this position, and the position at $t+dt/2$ found in the particle push, we can calculate the time centred current to second order accuracy by solving Equation 2.27. The advantage of this scheme is that it conserves charge on the grid as well as for all the particles, and hence if Poisson's equation is satisfied initially, it will remain so throughout the simulation.

For the components of the current which are directed outside the grid, e.g. J_z in a 2D grid, we must take moments by integrating over all pseudoparticles as in Equation 2.6. This process is described in detail in Section 2.2.3.

A diagram summarising this section, showing the complete variable dependencies and flow of the code over a single time step is given in Figure 2.3.

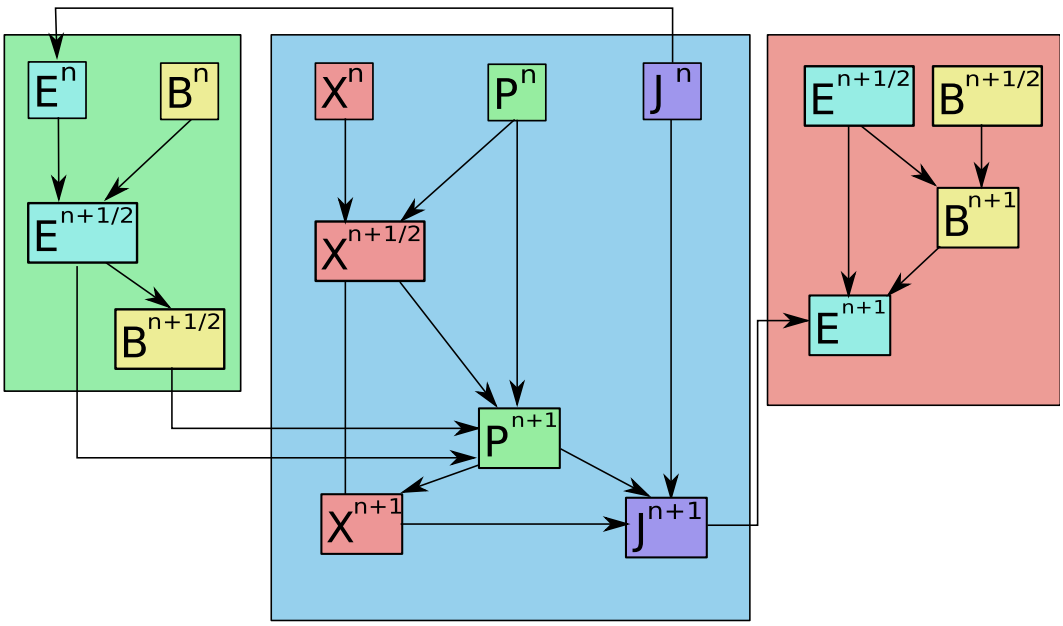

Figure 2.3: The dependencies and flow of the EPOCH particle-in-cell code over one time step. The green box represents the first half-update of the fields, the blue box is the particle push, and the red box is the final half-update of the fields.

2.2.3 Shape Functions

When taking moments over the distribution function to determine the current density $\mathbf{J}$, number density n and temperature T, each pseudoparticle is weighted onto the grid using a shape function. This shape function serves as the distribution of real particles which makes up a given pseudoparticle.

For the simplest method, nearest grid point (NGP) weighting, pseudoparticle properties are simply assigned to the nearest grid point. This effectively means the particles are rectangular in shape, with a width Δx. That is, particles uniformly fill the cell. This method is also called zero-order weighting, and though it is computationally the cheapest method, it produces noisy solutions.

The PIC and hybrid codes presented here make use of a second-order method which models pseudoparticles as a triangular cloud of width $2\Delta x$. This shape function is illustrated in Figure 2.4. Higher order shape functions using spline interpolation is possible, and results in a further reduction in noise. However, the computation significantly increases. To copy particle properties to the grid, we integrate the part of the shape function S which overlaps with the relevant cell. For example, the contribution of the jth particle with charge f to field variable F at the ith grid

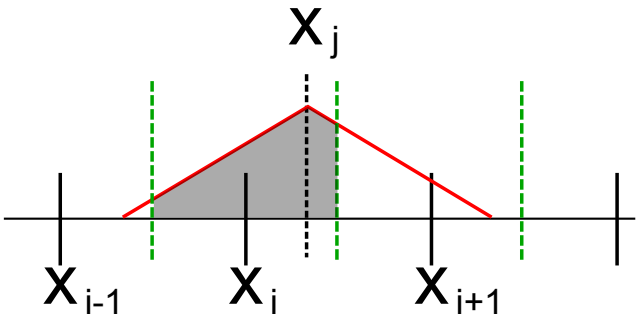

Figure 2.4: Triangular pseudoparticle for second-order weighting. The contribution of a particle at position x_j to grid point x_i is shaded.

point is given by:

$$F_i = f_j \int_{x_i - \frac{\Delta x}{2}}^{x_i + \frac{\Delta x}{2}} S(x_j - x) dx. \tag{2.28}$$

For the second-order weighting with a triangular shape function, the contribution becomes:

$$F_i = f_j \begin{cases} \frac{3}{4} - \frac{|x_j - x_i|^2}{\Delta x^2}, & |x_j - x_i| \leq \frac{\Delta x}{2} \\ \frac{1}{2}\left(\frac{3}{2} - \frac{|x_j - x_i|}{\Delta x}\right)^2, & \frac{\Delta x}{2} < |x_j - x_i| \leq \frac{3\Delta x}{2} \\ 0, & |x_j - x_i| > \frac{3\Delta x}{2}. \end{cases} \tag{2.29}$$

During the final steps for the code, we weight the fields to the particle positions, so that the Lorentz forces can be calculated at the particle positions. This time, we calculate the overlap between the pseudoparticle's shape function and the function representing the fields on the grid:

$$F_j = \int_{x_j - \Delta x}^{x_j + \Delta x} F(x) S(x_j - x) dx. \tag{2.30}$$

Here, the fields are approximated at first order such that the field is constant over each cell, and for a triangle shape function the integral reduces to:

$$
\begin{aligned}
F_j &= \frac{1}{2}F_{i-1}\left(\frac{1}{2}+\frac{x_i-x_j}{\Delta x}\right)^2 \\
&\quad +F_i\left(\frac{3}{4}-\frac{(x_i-x_j)^2}{\Delta x^2}\right) \\
&\quad +\frac{1}{2}F_{i+1}\left(\frac{1}{2}-\frac{x_i-x_j}{\Delta x}\right)^2 . \qquad (2.31)
\end{aligned}
$$

2.3 Hybrid Codes

The hybrid code described in this Chapter, and which is used for the work presented in the later Chapters of this Thesis, is part of a class of particle-in-cell code for which the electrons are treated as a fluid. The conversion of a fully kinetic particle-in-cell code to a hybrid code requires the removal of electrons as a particle species, and a change to the electromagnetic field solver to incorporate the electron fluid. The particle pusher and conversions between grid and particle properties using shape functions remain as detailed above. The electromagnetic field equations differ as follows [Winske et al., 2003].

To represent the electrons as a fluid, we require the electron fluid momentum equation:

$$
n_e m_e \frac{d\mathbf{v}_e}{dt} = -en_e(\mathbf{E}+\mathbf{v}_e\times\mathbf{B}) - \nabla\cdot\vec{\mathbf{P}}_\mathbf{e}, \qquad (2.32)
$$

where $\mathbf{v}_e$ is the electron fluid velocity, and $\vec{\mathbf{P}}_\mathbf{e}$ is the electron pressure tensor. This equation has omitted any resistive coupling between the electrons and the ion species. We now treat the fluid as inertia-less, such that the left hand side of Equation 2.32 is zero. We also assume the pressure tensor is isotropic, and that $\nabla\cdot\mathbf{E}$ is negligible on length scales of interest, implying charge neutrality such that $en_e = \Sigma_i q_i n_i$. For a plasma comprising only protons, $n_e = n_i = n$. This gives the following equation for $\mathbf{E}$:

$$
\mathbf{E} = -\frac{\nabla p_e}{en_e} - \mathbf{v}_e\times\mathbf{B} \qquad (2.33)
$$

We can eliminate the electron fluid velocity using Ampère's law with the low frequency, Darwin limit [Hewett, 1994]:

$$\nabla \times \mathbf{B} = \mu_0 \mathbf{J} \tag{2.34}$$
$$= \mu_0(\mathbf{J}_i - en_e\mathbf{v}_e), \tag{2.35}$$

where $\mathbf{J}_i$ is the total ion current. Hence, by substituting Equation 2.35 into 2.33, we arrive at an Ohm's Law which allows us to determine the electric field in the hybrid simulation:

$$\mathbf{E} = -\frac{1}{en_e}\left(\nabla p_e - \frac{(\nabla \times \mathbf{B}) \times \mathbf{B}}{mu_0} + \mathbf{J}_i \times \mathbf{B}\right). \tag{2.36}$$

For this work, we will be using an equation of state $p_e = n_e k_B T_e$ where T_e is the electron temperature, which remains a constant. This gives the following difference equation for the electric field:

$$\mathbf{E}^n = -\frac{1}{en_e^n}\left(k_b T_e \nabla n_e^n - \frac{(\nabla \times \mathbf{B}^n) \times \mathbf{B}^n}{\mu_0} + \mathbf{J}_i^n \times \mathbf{B}^n\right). \tag{2.37}$$

Note that this equation is not time dependent, so simply requires knowledge of all the fields at the required time step.

As with the particle-in-cell codes, the magnetic field is updated in time using Faraday's law, Equation 2.3. Since the hybrid code is being developed around the framework provided by the previously detailed particle-in-cell code, the scheme for the hybrid code operates in much the same way. The core algorithm of the particle pusher is identical, though the electromagnetic fields are solved in a different way. We still use the half acceleration method, except that since the electric field at the half time step is dependent on the magnetic field at the half time step, calculation of the magnetic field precedes that of the electric field. The code algorithm is hence as follows:

1. Update the magnetic field to the half time step using Faraday's law:

$$\mathbf{B}^{n+\frac{1}{2}} = \mathbf{B}^n - \frac{\Delta t}{2}(c^2 \nabla \times \mathbf{E}^{n+\frac{1}{2}}) \tag{2.38}$$

2. Update particle velocities to the half time step using the equations of motion. Using the velocities and positions at the half time step, take moments to calculate the current $\mathbf{J}^{n+\frac{1}{2}}$ and number density $n_e^{n+\frac{1}{2}}$.

3. Update the electric field to the half time step using the electron momentum

equation:

$$\mathbf{E}^{n+\frac{1}{2}} = -\frac{1}{en_e^{n+\frac{1}{2}}}\left(k_b T_e \nabla n_e^{n+\frac{1}{2}} - \frac{(\nabla \times \mathbf{B}^{n+\frac{1}{2}}) \times \mathbf{B}^{n+\frac{1}{2}}}{\mu_0} + \mathbf{J}_i^{n+\frac{1}{2}} \times \mathbf{B}^{n+\frac{1}{2}}\right) \tag{2.39}$$

4. Update the particle positions to the half time step and velocities to the full time step using the particle pusher. Calculate the current $\mathbf{J}^{n+1}$ using the Villasenor and Buneman method, and the number density n^{n+1} by taking moments.

5. Next, the fields are updated to the full time step using:

$$\mathbf{B}^{n+1} = \mathbf{B}^{n+\frac{1}{2}} - \frac{\Delta t}{2}(c^2 \nabla \times \mathbf{E}^{n+\frac{1}{2}}) \tag{2.40}$$

$$\mathbf{E}^{n+1} = -\frac{1}{en_e^{n+1}}\left(k_b T_e \nabla n_e^{n+1} - \frac{(\nabla \times \mathbf{B}^{n+1}) \times \mathbf{B}^{n+1}}{\mu_0} + \mathbf{J}_i^{n+1} \times \mathbf{B}^{n+1}\right) \tag{2.41}$$

6. Repeat from step 1.

This scheme is illustrated in Figure 2.5, which shows the full variable dependencies over a single time step.

2.3.1 Stability

The stability condition on a particle-in-cell code can be derived by considering a plane-wave solution to Maxwell's equations on the grid. For a 2D simulation staggered using the Yee grid in space, and with electric and magnetic fields staggered in time by half a time step, the differenced Maxwell's equations for the coupled E_x, E_y and B_z fields are as follows [Birdsall and Langdon, 2005]:

$$\frac{E_{x,j+1/2,k}^{n+1} - E_{x,j+1/2,k}^{n}}{\Delta t} = c\frac{B_{z,j+1/2,k+1/2}^{n+1/2} - B_{z,j+1/2,k-1/2}^{n+1/2}}{\Delta y} - J_{x,j+1/2,k}^{n+1/2}, \tag{2.42}$$

$$\frac{E_{y,j,k+1/2}^{n+1} - E_{y,j,k+1/2}^{n}}{\Delta t} = -c\frac{B_{z,j+1/2,k+1/2}^{n+1/2} - B_{z,j-1/2,k+1/2}^{n+1/2}}{\Delta y} - J_{y,j,k+1/2}^{n+1/2}, \tag{2.43}$$

$$\frac{B_{z,j+1/2,k+1/2}^{n+1/2} - B_{z,j+1/2,k+1/2}^{n-1/2}}{\Delta t} = -c\frac{E_{y,j+1,k+1/2}^{n} - E_{y,j,k+1/2}^{n}}{\Delta x} + c\frac{E_{x,j+1/2,k+1}^{n} - E_{x,j+1/2,k}^{n}}{\Delta y}, \tag{2.44}$$

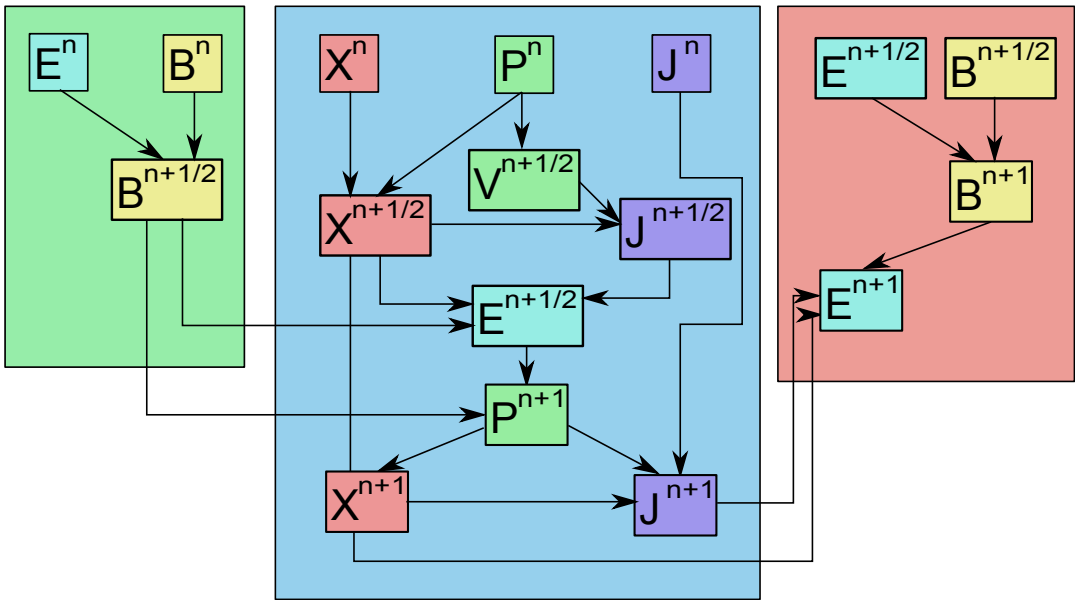

Figure 2.5: Dependencies and flow of the modified EPOCH hybrid code over one time step. The green box represents the first half-update of the fields, the blue box is the particle push, and the red box is the final half-update of the fields.

where Equations 2.42 and 2.43 are Ampère's Law, and Equation 2.44 is Faraday's Law. Substituting the plane wave solution $(\mathbf{E}, \mathbf{B}) = (\mathbf{E}_0, \mathbf{B}_0)\exp(i\mathbf{k}\cdot\mathbf{x} - i\omega t)$ into, for example, Equation 2.42, we arrive at:

$$\frac{E_x}{\Delta t}(e^{i\omega\frac{\Delta t}{2}} - e^{-i\omega\frac{\Delta t}{2}}) = \frac{cB_z}{\Delta y}(e^{ik_y\frac{\Delta y}{2}} - e^{-ik_y\frac{\Delta y}{2}}) \tag{2.45}$$

$$E_x\frac{\sin(\omega\Delta t/2)}{\Delta t} = cB_z\frac{\sin(k_y\Delta y/2)}{\Delta y}. \tag{2.46}$$

Extending the same analysis to the other difference equations, we can combine the resulting equations in the following way:

$$\Omega\mathbf{B} = c\kappa\times\mathbf{E} \tag{2.47}$$

$$\Omega\mathbf{E} = -c\kappa\times\mathbf{B} \tag{2.48}$$

where $\Omega = \sin(\omega\Delta t/2)/\Delta t$ and $\kappa_x = \sin(k_x\Delta x/2)/\Delta x$. By taking the cross product of Equation 2.47 with 2.48 and taking the dot product with κ, we can eliminate $\mathbf{E}$ and $\mathbf{B}$:

$$\Omega^2 = c^2\kappa^2 \tag{2.49}$$

$$\left(\frac{\sin\frac{\omega\Delta t}{2}}{c\Delta t}\right)^2 = \left(\frac{\sin\frac{k_x\Delta x}{2}}{\Delta x}\right)^2 + \left(\frac{\sin\frac{k_y\Delta y}{2}}{\Delta y}\right)^2. \tag{2.50}$$

The wave frequency ω is real, and hence the scheme is stable, on the condition that

$$(c\Delta t)^2 < \left(\frac{1}{\Delta x^2} + \frac{1}{\Delta y^2}\right)^{-1}. \tag{2.51}$$

This Courant-Friedrichs-Lewy (CFL) condition [Courant et al., 1928] defines the maximum timestep size in a particle-in-cell code. We note that the condition is dependent upon the fastest wave speed in the simulation, the speed of light c. This condition thus effectively prevents information from propagating across more than one grid cell within a single time step. The appearance of the $\mathrm{sinc}(k_x\Delta x/2)$ function in Equations 2.46 and 2.50 follows from the property that $\mathrm{sinc}(k_x\Delta x/2)$ is the Fourier transform of the rectangular step function of width Δx, which represents the size of the grid. Hence, a similar CFL condition arises for all simulation methods which employ a discrete grid in space and time.

In the hybrid case, we must consider the speed of whistler waves in the simulation. The dispersion relation for the whistler wave in a cold, magnetised plasma is given by:

$$c^2k^2 = \omega^2\left(\frac{\left(1+\frac{\omega}{\Omega_{ci}}\right)\left(1-\frac{\omega}{\Omega_{ce}}\right)}{\left(1-\frac{\omega}{\omega_+}\right)\left(1+\frac{\omega}{\omega_-}\right)}\frac{v_A^2}{c^2+v_A^2}\right)^{-1}, \tag{2.52}$$

which has a resonance at the electron cyclotron frequency Ω_{ce}, and hence damping of high frequency whistler waves. In the hybrid limit, for which $\Omega_{ce} \to \infty$, the whistler dispersion relation reduces to

$$c^2k^2 = \omega^2\left(\left[1+\frac{\omega}{\Omega_{ci}}\right]\frac{v_A^2}{c^2+v_A^2}\right)^{-1}. \tag{2.53}$$

In this case, no electron cyclotron resonance occurs. Here $\omega \propto k^2$, and the wave speed rises with k without bound. Hence at high frequency and wavenumber, whistler waves will break any CFL condition we impose. To prevent unstable growth of high k whistler waves and ensure the code's stability, we therefore employ a low pass filter which is applied to the electromagnetic fields at each time step. This curbs the growth of the waves at high k, and allows the low k waves which do not

break the CFL condition to propagate normally. Since transformations to Fourier space are computationally intensive for massively parallel codes, we take advantage of the convolution theorem to apply the filter in real space. The convolution theorem states:

$$\tilde{f} \cdot \tilde{g} = \widetilde{f * g}, \tag{2.54}$$

for functions f and g, their convolution $f * g$, and where a tilde represents a Fourier transform. Hence, for a field f and k-space filter function $\tilde{g}$, we can apply the same filter while remaining in real space by taking the convolution of the field f with the inverse Fourier transform of the filter function g. For a Gaussian low-pass filter of width σ, we therefore take the convolution of the field with a Gaussian function of width $1/\sigma$. The Gaussian function must be normalised in real space to conserve the energy of the electromagnetic fields. For the simulations presented in this Thesis, we convolve electromagnetic fields with a normalised Gaussian function of width $\Delta x/2$ in real space, where Δx is the width of the grid cell.

With the high k whistler waves damped, our CFL condition is a modification of Equation 2.51 with the speed of light replaced by the fast magnetoacoustic wave.

2.3.2 Testing

There are a number of useful diagnostics for plasma simulations. First, we will examine the hybrid code's ability to reproduce single particle dynamics, as a test of the code's particle pusher. We will then examine the propagation of waves in a uniform plasma.

2.3.2.1 Single Particle Dynamics

The gyro-radius, cyclotron frequency, and $\mathbf{E} \times \mathbf{B}$ drift velocity can be measured as a means of testing the code's ability to correctly reproduce single particle dynamics. These are most easily measured by tracking the trajectories of tracer particles in a simulation with uniform number density, temperature and electromagnetic fields.

Figure 2.6 shows the results of this test, with space and time coordinates normalised to the thermal gyro-radius and gyro-frequency. There we can clearly see the expected oscillation of the particle for the chosen electromagnetic fields. This confirms that the code is calibrated correctly for the fields on which those parameters depend, namely the magnetic field strength, temperature, and mass-to-charge ratio.

We test the $\mathbf{E} \times \mathbf{B}$ drift velocity by transforming to a frame of reference for which we expect no net background electric field, according to the non-relativistic

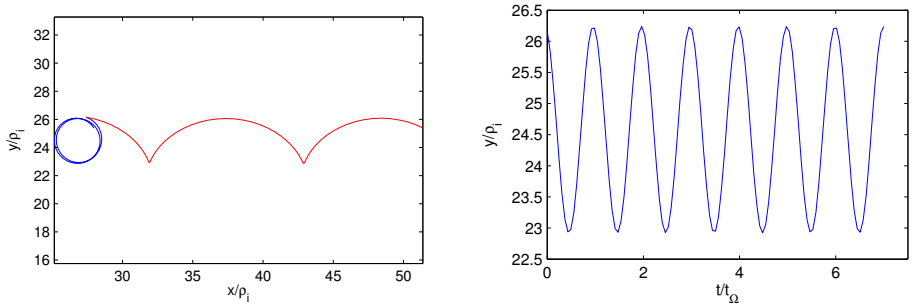

Figure 2.6: Left: Trajectory of a particle with thermal gyro-radius in the simulation frame (red) and in a frame moving with the $\mathbf{E} \times \mathbf{B}$ drift velocity (blue). Right: y-component of the trajectory as a function of time, demonstrating gyration at the correct frequency. Both these tests demonstrate the particle pusher is working correctly.

frame transformations $\mathbf{E}' = \mathbf{E} - \mathbf{v} \times \mathbf{B}$. Under such a frame transformation, the trajectory of charged particles will change from cycloid to circular. This is demonstrated in the left of Figure 2.6, and we can conclude the code correctly reproduces the effects of motional electric fields and frame transformations, as will become important in later chapters.

2.3.2.2 Wave Propagation

Here we examine the propagation of waves in a uniform background plasma in two ways. First, we excite a high amplitude Alfvén wave and directly measure the speed of the propagating wave front. Second, we calculate the dispersion relation of all waves able to propagate as a result of noise in the background.

The propagation of an Alfvén and a fast magnetoacoustic wave is demonstrated in Figure 2.7 for a proton plasma with $n_0 = 10^{27}\mathrm{m}^{-3}$, $T = 290\mathrm{K}$ and $B_0 = 10\mathrm{T}$. A high amplitude Alfvén wave is excited in the code by seeding the otherwise uniform initial conditions with a Gaussian perturbation in the component of the magnetic field perpendicular to the background field with amplitude $B_0/10$ and width $5\Delta x$. Likewise, the fast magnetoacoustic wave is seeded using a Gaussian perturbation in the parallel magnetic field. The code performs as expected, with the waves propagating at the Alfvén speed $v_A = B/\sqrt{m_p n \mu_0}$ and fast magnetoacoustic wave $v_f^2 = c_s^2 + v_A^2$.

We can extend this test to all possible wave modes by instead exciting a broad spectrum of wavenumbers and frequencies, and examining the dispersion relation which results. In a particle-in-cell code, noise generated by particle motion can

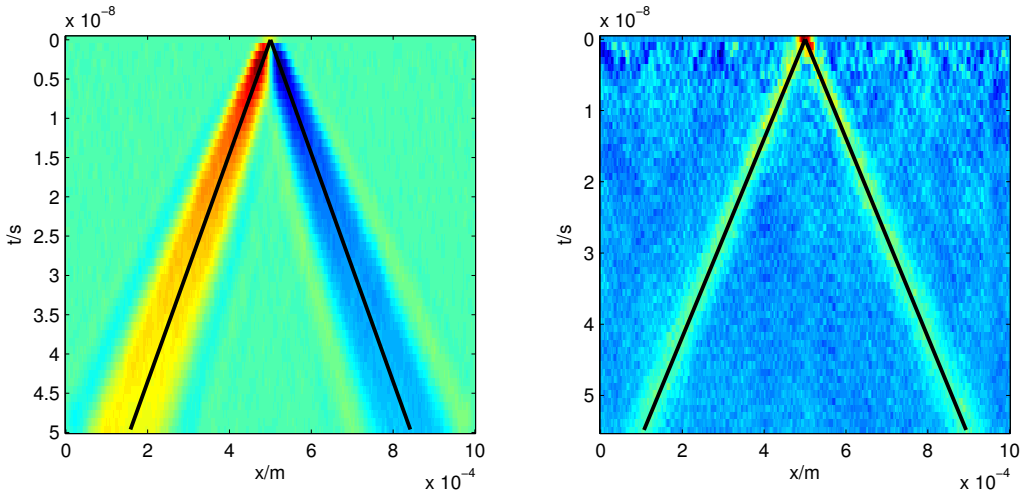

Figure 2.7: Colour maps displaying the evolution of a 1D slice of the z-component of the magnetic field over time, demonstrating the propagation of an Alfvén wave (left) and a fast magnetoacoustic wave (right). The respective wave speeds v_A and v_f are overlaid as solid black lines.

Character	Oscillator	Conditions	Wave
Electrostatic	Electrons	$B_0 = 0$ or $k \parallel B_0$	Langmuir wave
		$k \perp B_0$	Upper hybrid
	Ions	$B_0 = 0$ or $k \parallel B_0$	Ion acoustic wave
		$k \perp B_0$ (exactly)	Lower hybrid
Electromagnetic	Electrons	$B_0 = 0$	Light wave
		$k \parallel B_0$	Whistler mode
	Ions	$k \parallel B_0$	Alfvén wave
		$k \perp B_0$	Magnetoacoustic

Table 2.1: Wave modes in uniform plasmas.

excite small amplitude waves over this broad spectrum, and hence we can recover the dispersion relation by transforming one of the electromagnetic field variables from the space and time domain to $\omega - k$ space.

For a uniform plasma with a background magnetic field applied as an initial condition, there are a number of different modes we can expect to propagate. These are summarised in Table 2.1. The theoretical dispersion relations for these waves in a cold, magnetised plasma are shown in Figure 2.8. The frequencies associated with the ordinary (O), extraordinary (X), left- and right-polarised light modes, as well as upper and lower hybrid modes as seen in Figure 2.8, are as follows:

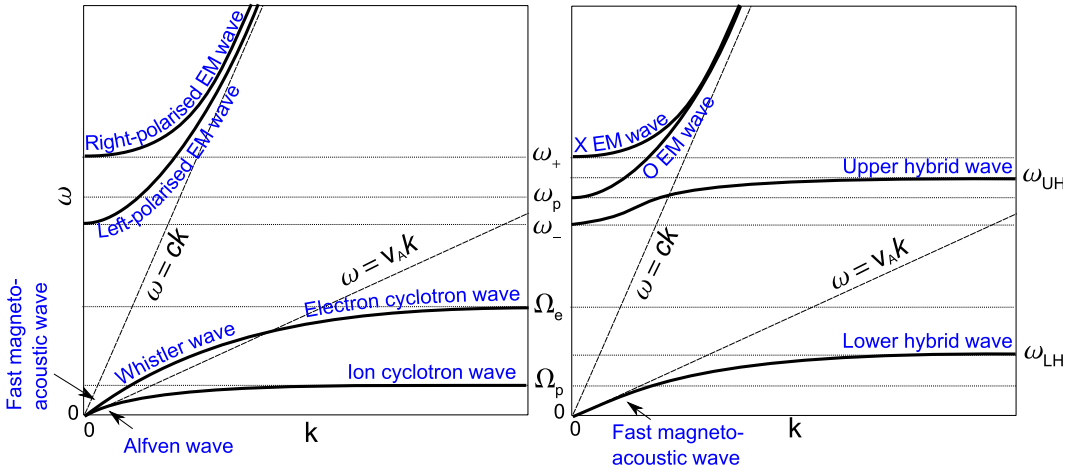

Figure 2.8: Dispersion relations for cold, magnetised plasmas, with propagation parallel (left) and perpendicular (right) to the background magnetic field.

$$\omega_{UH} = \sqrt{\omega_{pe}^2 + \Omega_{ce}^2} \tag{2.55}$$

$$\omega_{LH} = ((\Omega_{ci}\Omega_{ce})^{-1} + \omega_{pi}^{-2})^{-\frac{1}{2}} \tag{2.56}$$

$$\omega_{\pm} = \pm\frac{1}{2}(\Omega_{ce} + \Omega_{ci}) + \frac{1}{2}\sqrt{(\Omega_{ce} - \Omega_{ci})^2 + 4\omega_{pi}^2} \tag{2.57}$$

where the subscript 'e' denotes frequencies associated with the electron population, and 'i' the ion frequencies. In the case of a fully kinetic particle-in-cell code, all these waves are able to propagate. At high frequencies, the clearest waves are the light waves, which are shown in Figure 2.9. To generate this dispersion relation, we have used a simulations with background fields are $n_0 = 10^{19}\mathrm{m}^{-3}$, $T = 10\mathrm{K}$ and $B_0 = 0.4\mathrm{T}$.

In the case of the hybrid code, the electromagnetic waves are excluded as a result of taking the low-frequency Darwin limit. At lower frequencies, we can expect the propagation of Alfvén, magnetoacoustic and whistler waves. Such a dispersion relation has been generated from a simulation with background fields $n_0 = 10^{27}\mathrm{m}^{-3}$, $T = 10\mathrm{K}$ and $B_0 = 10\mathrm{T}$, and is shown in Figure 2.10. The figure also demonstrates ion cyclotron damping of the parallel Alfvén waves at the ion cyclotron frequency, manifesting as a horizontal turnover of that wave, the ion acoustic mode. Since we have neglected electron kinetic effects, the whistler wave is not damped at the electron cyclotron frequency as it is in Figures 2.8 and 2.9.

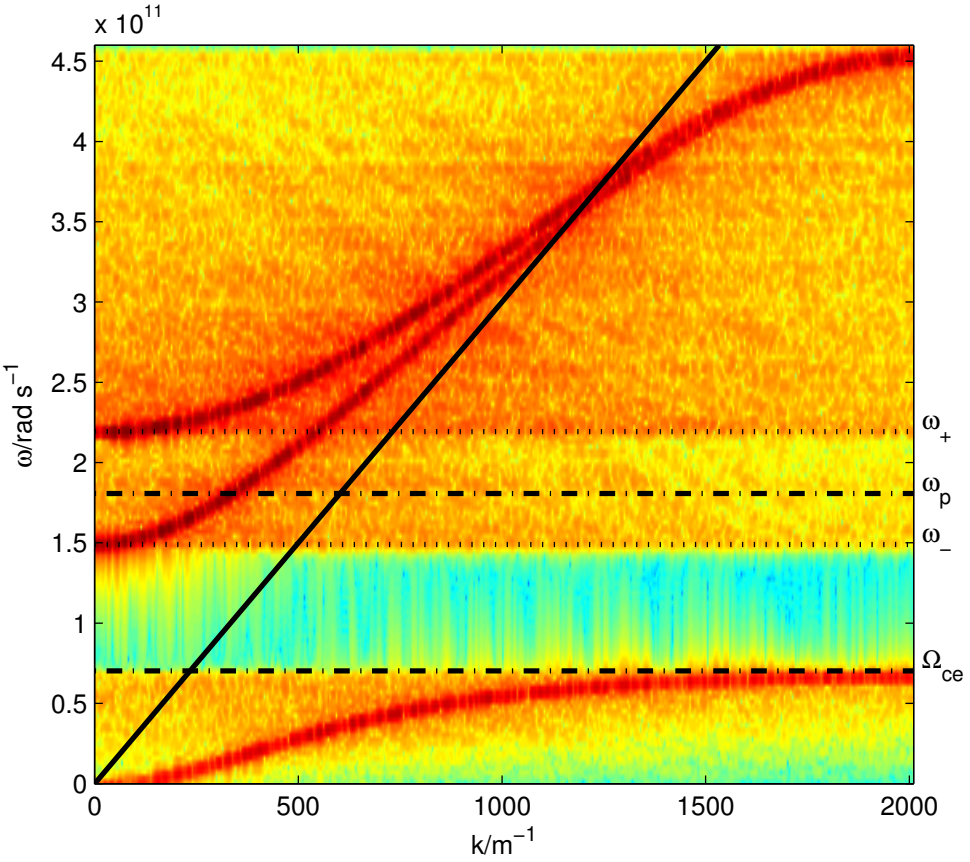

Figure 2.9: Dispersion relation from a uniform, cold, magnetised plasma simulated using the 1D fully kinetic particle-in-cell code, with the background magnetic field parallel to the simulation domain. The colour map marks the power of a given frequency component. This demonstrates the propagation of left and right polarised light waves in the code, including the cut-off at the ω_+ and ω_- plasma frequencies. The speed of light is overlaid as a black line.

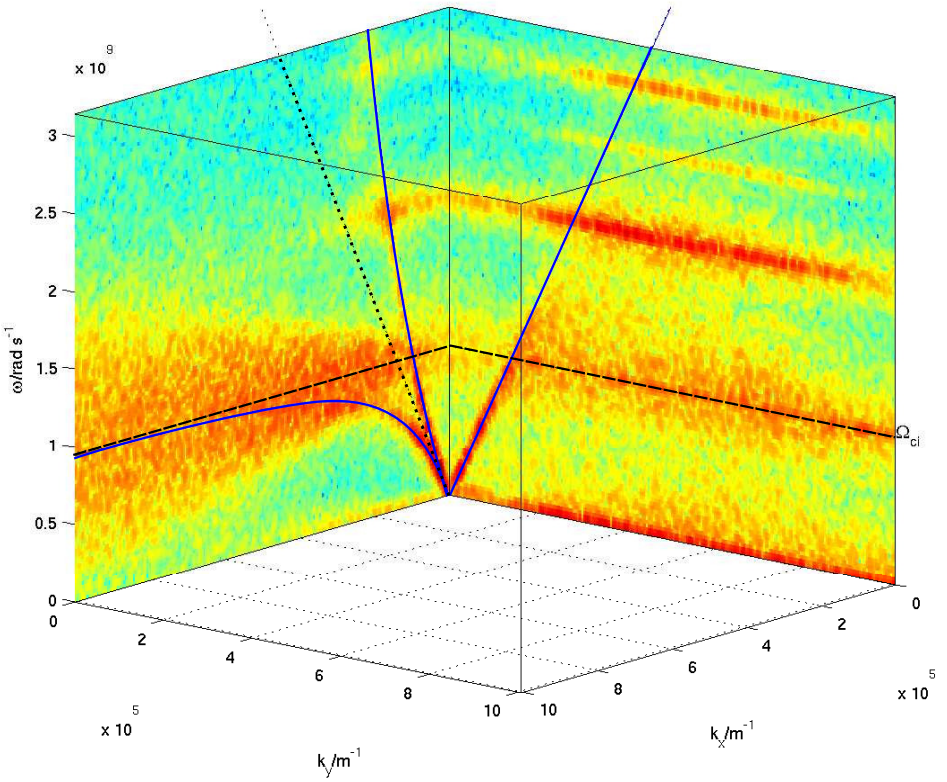

Figure 2.10: Dispersion relation for a uniform, cold, magnetised plasma simulated using the 2D hybrid code described in this chapter, with the background magnetic field in the x-direction. The colour map marks the power of a given frequency component. These conditions reproduce the dispersion relations for a cold, magnetised plasma both parallel and perpendicular to the magnetic field direction. The theoretical dispersion relations for Alfvén, magnetoacoustic and whistler waves are overlaid in blue, and show close correspondence with the code's output. A dashed horizontal black line marks the ion cyclotron frequency, and a diagonal dotted black line marks the Alfvén speed. Waves at high-k are removed by low-pass filtering to prevent their unstable growth, as discussed in Section 2.3.1.

2.3.2.3 Resolution

The number of pseudoparticles used to sample the phase space density of the plasma has a significant effect on the solution generated by a particle-in-cell code. A small number of particles per cell leads to a significant departure from the continuous, physical phase space density, and numerical noise may dominate. Hence, in order to have confidence in the code, we must take care to sufficiently resolve the phase space density using a high number of pseudoparticles per cell. However, we must balance this need against the increase in computational load associated with the use of more pseudoparticles. To find this balance between numerical noise and computational load, we present here several simulations of the evolution of 2D blob-like Gaussian perturbations in a background flow, typical of those presented in Chapters 3 and 4, differing only in the number of pseudoparticles per grid cell. The 2D simulation domain consists of 120 grid cells in x and y, with a resolution $\Delta x = 0.4\rho_i$, background magnetic field $B_z = 0.4T$, temperature $T = 4 \times 10^6$K, number density $n_0 = 10^{19}\mathrm{m}^{-3}$ and background flow speed $0.2v_A$. The Gaussian perturbations are initialised with radius 5_{ρ_i}, and peak density $n_b = 2n_0$.

A comparison of the evolution of simulations with an average of 5 to 200 particles per grid cell is given in Figure 2.11. For those simulations with low particles per cell, we find that the Gaussian blob breaks up over a shorter timescale. The coherency of the blob increases with more particles per cell, and we find all important features of the blobs are resolved, i.e. the solution converges, when we utilise between 50 and 100 particles-per-cell. The mushrooming structure we observe will be discussed in detail in Chapter 3. So that we can be confident in our results, we conduct the work presented in this Thesis using an average of 100 particles per cell, and note that in the region of the overdensity, the number of particles per cell is proportionally higher.

We now examine the effect of the grid resolution on the same initial conditions. In this case, the need to resolve full ion dynamics and high-k waves must be balanced against the need to reduce computational load. In Figure 2.12 we present the results of simulations with resolution δx ranging from 0.2 to $2\rho_i$. Note that since the shape function of the pseudoparticles extends over several computational cells, finite Larmor radius effects can still manifest when the resolution of the grid exceeds the thermal gyro-radius. For simulations of low resolution we note a significant increase in the noise present in the background, with an amplitude in the most extreme case in excess of the original Gaussian perturbation. Although the highest resolution simulation, with $\Delta x = 0.2\rho_i$, captures the most detail in the blob's evolution, it represents an order of magnitude increase in computational load. Hence, we

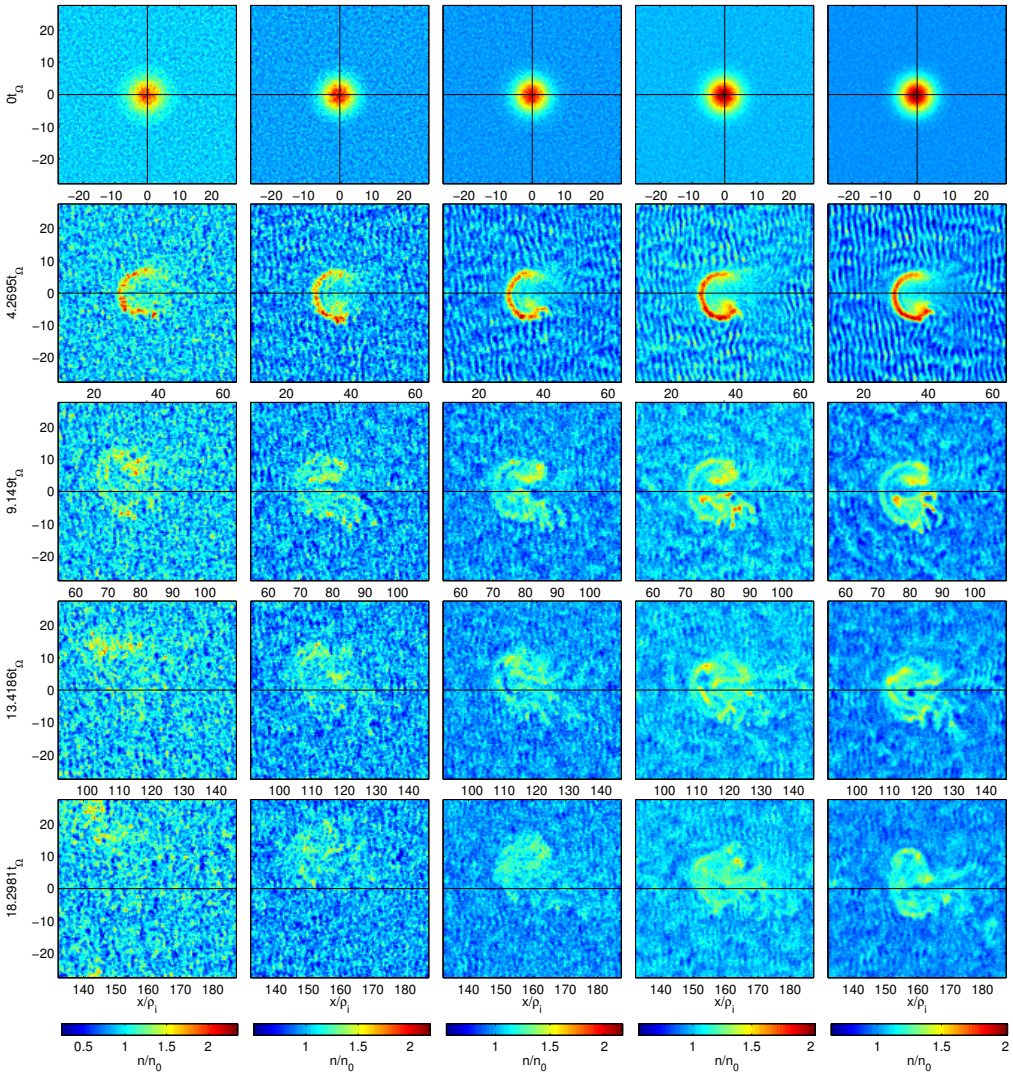

Figure 2.11: Evolution of a Gaussian density blob for simulations using 10, 20, 50, 100 and 200 particles per cell (left to right). Simulations utilising fewer than 50 particles per cell show have reduced lifetime and fail to resolve some features of simulations with more pseudoparticles.

choose a grid resolution $\Delta x = 0.4\rho_i$, for which the important features of the evolving blob are resolved, background noise is small compared to the blob and does not grow, and computational load is manageable.

2.3.3 Application

The first true hybrid code, comprising particle ions and fluid electrons, was applied to pinch experiments in laboratory plasmas[Chodura, 1975]. For that study, the aim was to properly model the reflection of ions from high Mach number shocks during the implosion of the cylindrical plasma, in the case that the ion gyro-radius is larger than the radius of the cylindrical tube. The hybrid algorithm was subsequently used for similar laboratory experiments, for example [Sgro and Nielson, 1976; Hamasaki et al., 1977], and soon generalised to two-dimensions [Hewett, 1980]. Despite early successes in laboratory plasmas, subsequent studies using hybrid codes have largely been within the scope of space plasma physics. Some of these applications will be discussed below.

Even before the first true hybrid code was developed by Choudra, simulations of the Earth's bow shock were conducted in [Auer et al., 1971], which modelled the ions as charged sheets, with the aim of finding the mechanism responsible for the heating of ions by collisionless shocks. The hybrid algorithm developed by [Sgro and Nielson, 1976] was first applied to the study of the quasi-perpendicular bow shock by [Leroy et al., 1981], and reproduced phenomena such as ion reflection and overshoots of the magnetic field and density, and the formation of a standing whistler wave [Leroy and Winske, 1983; Kan and Swift, 1983].

Hybrid codes have since been widely applied to the study of collisionless quasi-perpendicular and quasi-parallel shocks in a number of astrophysical environments, including cometary shocks [Lipatov et al., 1997], interplanetary and bow shocks [Burgess et al., 2012], stellar wind termination shocks [Kucharek and Scholer, 1995], the acceleration of cosmic rays [Bell, 1978], and for processes accompanying coronal mass ejections [Desai and Burgess, 2008]. The issue of ion acceleration at collisionless shocks is common to these environments, and hybrid simulations have proven successful in reproducing the observed populations of hot ions by satellites such as ULYSSES when passing collisionless shocks [Gloeckler et al., 1994]. The power-law spectra of hot ions was found to be inconsistent with expected heating mechanisms such as first-order Fermi acceleration, for which the multiple reflection of charged particles by a moving change in the magnetic field over the shock results in a large increase in energy. Fermi acceleration should also favour acceleration of heavier ions, which was not observed.

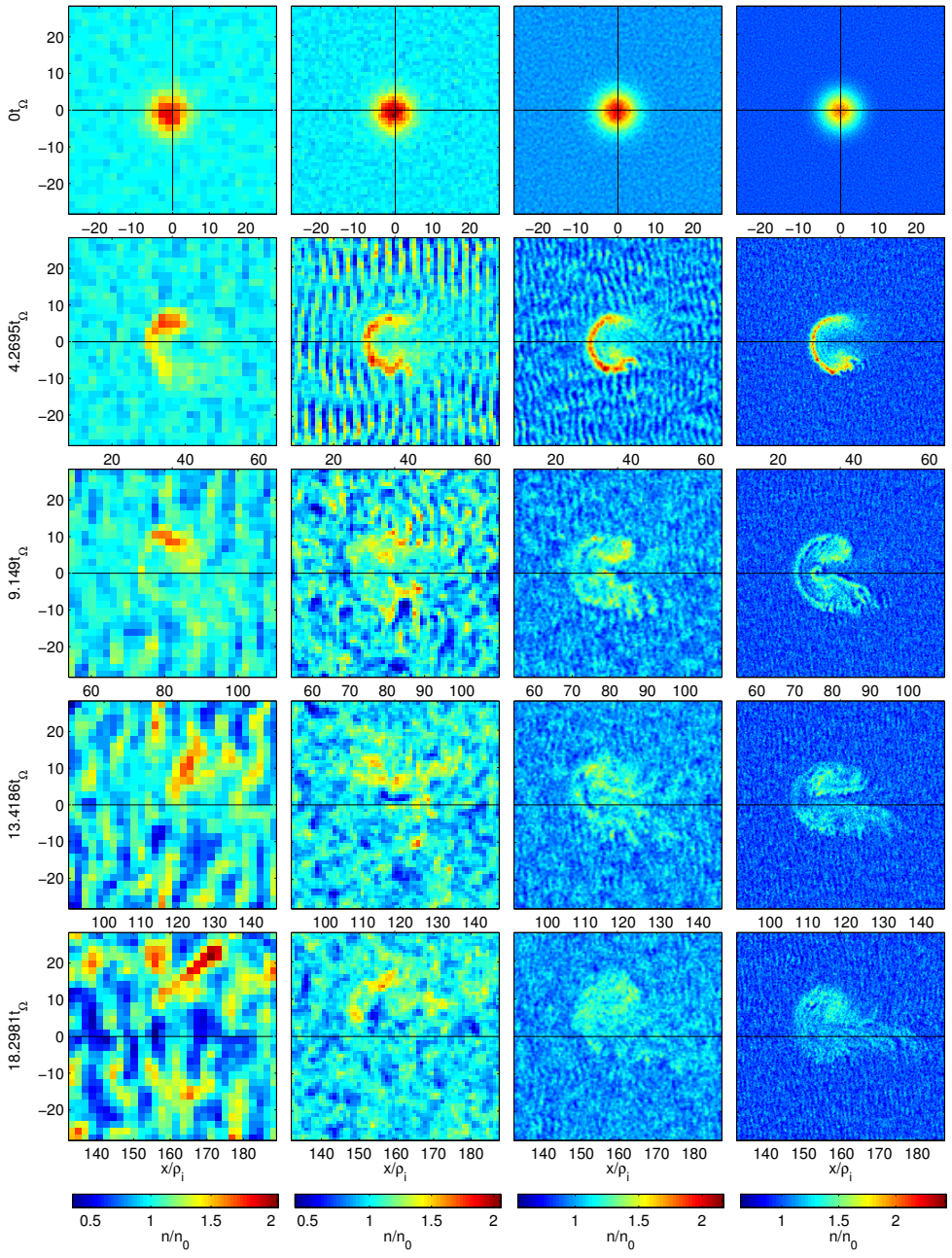

Figure 2.12: Evolution of a Gaussian density blob for simulations of resolution 1.6, 0.8, 0.4 and $0.2\rho_i$ (left to right). Simulations with lower resolution fail to capture the expected evolution of the density blobs, and background noise grows to a significant fraction of the blob's peak density.

Alternative heating mechanisms that have been proposed for accelerating pick-up ions at collisionless shocks include shock drift acceleration, shock surfing (as illustrated in Figure 2.13), and acceleration by upstream MHD turbulence. These mechanisms have been successfully simulated using hybrid codes in many cases [Forslund et al., 1984; Quest, 1985; Giacalone et al., 1994; Lipatov, 2002]. For example, shock reformation [Burgess, 1989] leads to the formation of structures on the ion gyro-scale. Heating of particles at collisionless shocks had been shown to occur using a hybrid code when gyrating particles are reflected between the shock and these reformed upstream structures [Su et al., 2012]. These particles hence remain in the region of the shock for many gyro-periods, and may be accelerated by the electric field.

However, we note that the study of collisionless shocks using hybrid codes has also revealed limitations of the method. In contrast to the shock solutions obtained using hybrid simulations, which are typically time stationary [Leroy and Winske, 1983; Burgess, 1989], fully kinetic PIC simulations have demonstrated dynamic shock structures which reform on the order of the ion gyro-period [Schmitz et al., 2002; Scholer et al., 2003; Lee et al., 2004]. In contrast, the generation of reforming structures under the hybrid limit is highly dependent on Mach number, grid size and resistive diffusion length scale [Quest, 1986]. Additionally, PIC simulations have demonstrated that the length scale of the shock potential steepens to electron scales [Scholer et al., 2003]. Hence, electronic kinetics play a significant role in shock dynamics that cannot be captured using hybrid codes. Specifically, if the steepness of gradients at electron scales is important to the physical processes we wish to study, as is the case for the acceleration of electrons by collisionless shocks, a hybrid model is insufficient, and PIC or Vlasov codes must be used instead.

There has also been much success using hybrid codes to simulate the interaction of the solar wind with strongly magnetised obstacles, such as the Earth's magnetosphere [Swift, 1995]. The codes successfully predicted features such as the bow shock, magnetopause and magnetotail, and also allow us to predict, with limited accuracy, the structure of the heliosphere [Lipatov, 2002]. Additionally, the generation of filamentary structures in the boundary layers of Earth's magnetosphere is observed to take place on ion kinetic scales [Nagano, 1979; Hasegawa et al., 2004; Sundkvist et al., 2005; Sundkvist and Bale, 2008] and has been the subject of kinetic simulations in recent years [Nykyri and Otto, 2001; Smets et al., 2007; Pritchett and Mozer, 2011].

The interaction between the solar wind and weakly- or un-magnetised gyro-scale obstacles such as Venus [Brecht and Ferrante, 1991; Terada et al., 2002], Mars

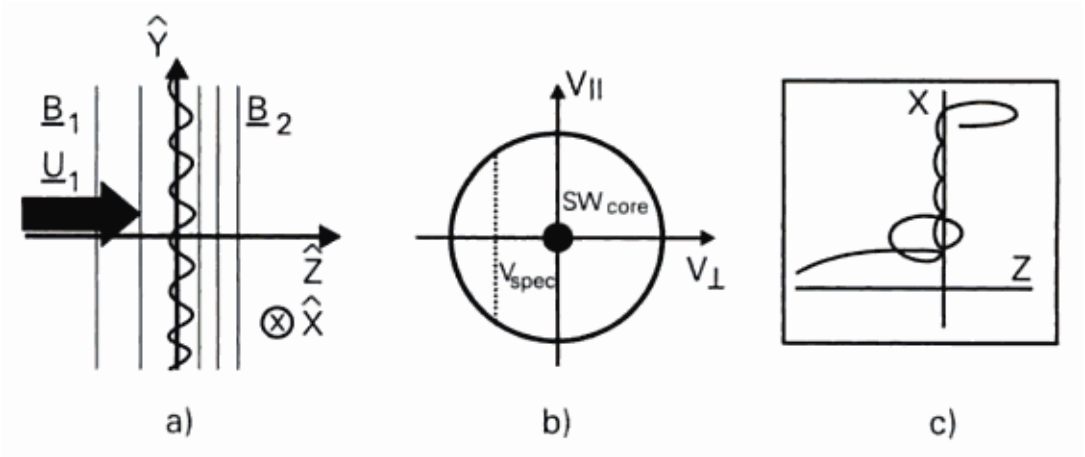

Figure 2.13: a) Geometry of a quasiperpendicular shock at $z = 0$, with subscript 1 for upstream and 2 for downstream of the shock. b) Idealised shell distribution for pick-up ions in the fluid frame, including the cold solar wind core and the velocity $V_{\rm spec}$ below which pick-up ions are reflected by the electrostatic shock potential barrier. c) Example trajectory of a pick-up ion showing multiple reflection at the perpendicular shock. (Reproduced from [Lipatov, 2002])

[Brecht, 1997; Motschmann and Kührt, 2006a; Kallio and Janhunen, 2002], comets [Lipatov et al., 1997; Bagdonat and Motschmann, 2002; Motschmann and Kührt, 2006b] and moons [Simon and Motschmann, 2009; Kriegel et al., 2009], and comparisons between these objects [Sauer et al., 1995; Shimazu, 2001], also continue to attract research. These simulations have demonstrated phenomena such as a multiple shock structure [Shimazu, 2001], the escape of ions through the magnetotail [Shimazu, 2001; Kallio and Janhunen, 2002], asymmetry in the Kelvin-Helmholtz instability at the ionopause [Terada et al., 2002], and pick-up ion tail structure [Lipatov et al., 1997; Simon and Motschmann, 2009; Kriegel et al., 2009].

Artificial solar wind obstacles, such as the AMPTE ion releases [Valenzuela et al., 1986], have also received considerable attention. Early observations noted significant deviations of the AMPTE releases from the expected behaviour for comets and planets [Brecht and Thomas, 1987]. An anomalous deflection of the release perpendicular to the solar wind background flow at early times, and an asymmetry in the shape of the tail of pick-up ions were later reproduced using hybrid simulations in 1D [Chapman and Schwartz, 1987], 2D [Harold and Hassam, 1991] and 3D [Delamere et al., 1999]. The success of these simulations is illustrated in Figure 2.14.

Magnetic reconnection plays an essential role in determining the configuration of magnetic fields in astrophysical and space plasmas, and is responsible for fast

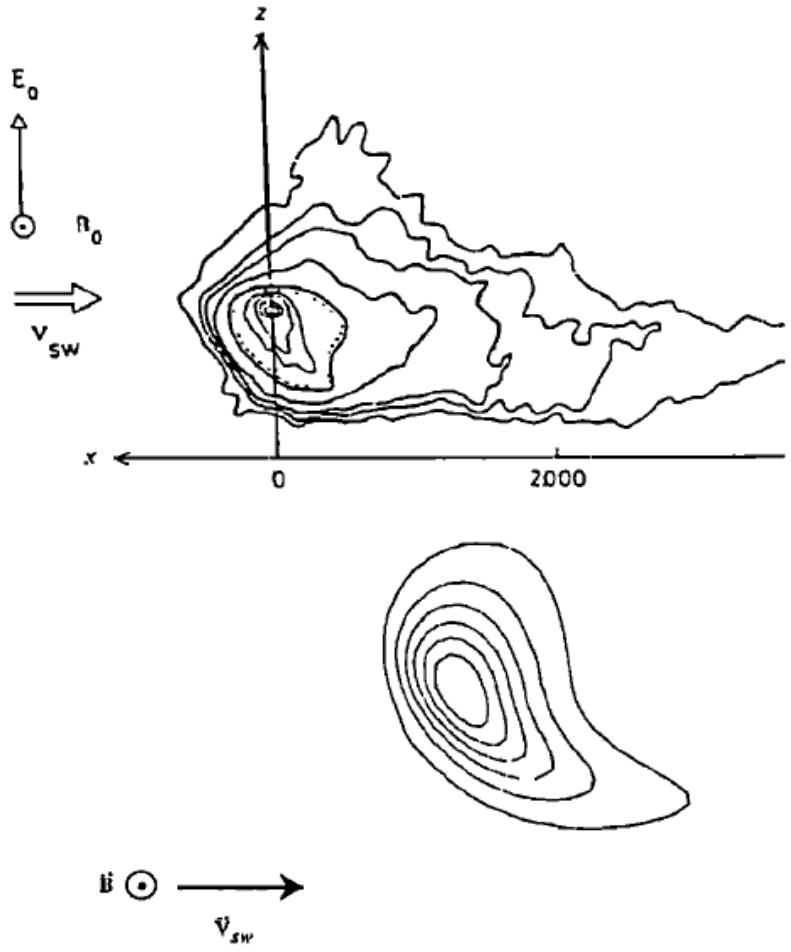

Figure 2.14: Top: Outlines of the comet head from the AMPTE release evolving in 15s intervals (Reproduced from [Valenzuela et al., 1986]). Bottom: Density contours for a 2D hybrid simulation of the AMPTE comet, reproducing the asymmetric tail at early times (Reproduced from [Harold and Hassam, 1991]).

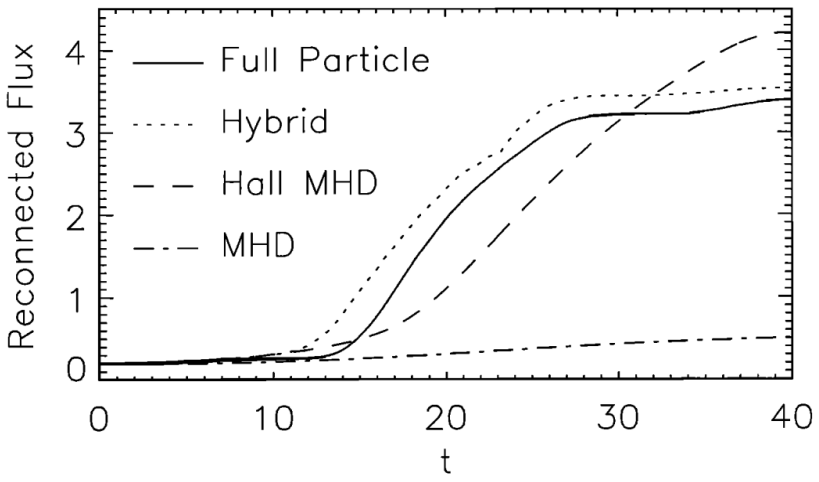

Figure 2.15: Reconnected magnetic flux as a function of time for fully kinetic, hybrid and fluid simulation models. There is close correspondence between models employing Hall physics. (Reproduced from [Birn et al., 2001].)

conversion of magnetic field energy to thermal and kinetic energy. In the Earth's magnetopause and magnetotail, current sheets at reconnecting regions exist with thickness on the order of the ion gyro-radius [Hesse and Winske, 1994]. Hence, ion kinetic effects cannot be ignored in these regions. As a result, hybrid codes have also been used to simulate collisionless magnetic reconnection [Hesse and Winske, 1994; Birn et al., 2005; Yin et al., 2001], allowing the study of kinetic effects on the ion tearing and beam instabilities, and asymmetries which develop in the magnetic structure of thin current sheets [Karimabadi et al., 2004].

As with shocks, subsequent fully kinetic PIC simulations of reconnection have revealed inconsistencies between hybrid simulations and those which resolve electron kinetic effects. A comprehensive comparison of reconnection methods has been presented in [Birn et al., 2001]. Though reconnection rates are closely matched for methods including Hall physics, as shown in Figure 2.3.3, the electron current layer was thinner for the hybrid model than for the PIC case by a factor of 2, and the ion jet was wider by a factor of 2 in the hybrid and PIC simulations compared to Hall MHD models. This demonstrates, again, that electron scales determine the validity of the hybrid method. However, in some cases hybrid codes may perform better than PIC codes for the study of reconnection. For example, in [Schmitz and Grauer, 2006], simulations using a Vlasov code demonstrated small scale structures in the electron current density that resembled those found in hybrid simulations, but had been smeared out by numerical noise in PIC simulations.

Chapter 3

Transport and Evolution of Ion Gyro-scale Blobs

3.1 Introduction

Coherent, propagating blobs have been observed to occur in the outer regions of tokamak plasmas, near the last closed flux surface. Some blobs may be the poloidal projection of magnetic flux tubes, or ropes, that extend along the direction of the magnetic field. These undergo radial transport, and can break free of the confinement region. Blobs with sufficient radial velocity can strike the walls of the tokamak, increasing local particle and energy fluxes, reducing divertor efficiency, and increasing impurity levels. Such blobs have been imaged in, for example the DIII-D [Boedo et al., 2003], Alcator C-mod [Grulke et al., 2006], NSTX [Myra et al., 2006], ASDEX Upgrade [Nold et al., 2010] and MAST [Kirk et al., 2006] tokamaks and in other laboratory experiments, for example [Windisch et al., 2011]. Polarising curvature drifts of ions and electrons, giving rise to an electric field that may not be shorted out by parallel motion under tokamak edge conditions, give rise in the classic picture to $\mathbf{E} \times \mathbf{B}$ radial blob motion. This theoretical model is described in more detail in Section 1.3.2.1, and discussion of observations of blobs can be found in Section 1.3.2.2 For a recent review of edge plasma physics in tokamaks we refer to [Krasheninnikov, 2011].

Current tokamak diagnostics offer clear observations of large scale blobs, however their limited resolution at present prohibits the observation of smaller blobs on scales of the order of the ion gyro-radius. In such cases, ion particle dynamics may play an important role in blob transport and evolution, inviting a kinetic numerical study. For plasma phenomena arising on the smallest length and time scales, ki-

netic methods such as particle-in-cell (PIC) codes are applicable. However the ion gyro-scales of interest here represent an intermediate phase between a fully kinetic treatment, and previous studies in the fluid regime. On these intermediate scales, it is necessary to capture the gyration of ions around magnetic field lines, while the gyration of electrons can be neglected. Hence a hybrid model is required for which ions are treated kinetically, and electrons as a fluid.

A hybrid model has numerous advantages which apply directly to the results presented here. These include: capturing the non-linear interaction between ion gyration and plasma inhomogeneity, cross-scale coupling between ion gyro-scale kinetic modes and fluid MHD-like modes, and the ability to resolve phenomena on much shorter timescales than fluid models. In addition to the ability to study inhomogeneities in configuration space, hybrid codes also enable the study of non-Gaussian ion velocity distributions, such as beams and their instabilities, while incorporating several distinct ion populations. Interaction and momentum transfer between these populations can lead to novel results that cannot be obtained in a single fluid description.

Although hybrid codes incorporating six-dimensional particle-in-cell ion kinetics are widely applied to the study of space plasmas, as discussed in Section 2.3.3, this work represents their first application to distinctive magnetic confinement fusion plasma regimes. In the fusion context, hybrid treatments[Park et al., 1999] typically involve ion kinetics that are gyro-averaged.

In the classical picture discussed in Section 1.3.2.1, blobs in the SOL are subject to a radial $\mathbf{E} \times \mathbf{B}$ drift resulting from a polarising drift within the blob [Krasheninnikov, 2001]. However, uncertainty exists in the range of positions at which blobs may be created [Nold et al., 2010; Krasheninnikov, 2011]. This uncertainty allows that some may propagate first through the confined plasma within the separatrix. In the following chapters, we simulate the evolution of those blobs which are born and propagate first within the confined plasma, which are not subject to the polarising drift and resulting radial force. The initial and boundary conditions include a background flow which interacts self-consistently with the blob. The motional electric field $\mathbf{E} = -\mathbf{u}_{\text{flow}} \times \mathbf{B}$ present in the flow imposes a potential difference across the blob, as shown in Figure 3.1. The motional electric field and resulting $\mathbf{E} \times \mathbf{B}$ drift can be considered equivalent to the $\mathbf{E} \times \mathbf{B}$ drift which results from polarisation of the blob due to charge separation in the SOL.

Simulations within the field of space plasma physics which most closely resemble the work presented here are those which deal with small unmagnetised releases in the solar wind [Lipatov et al., 1997; Valenzuela et al., 1986; Chapman and

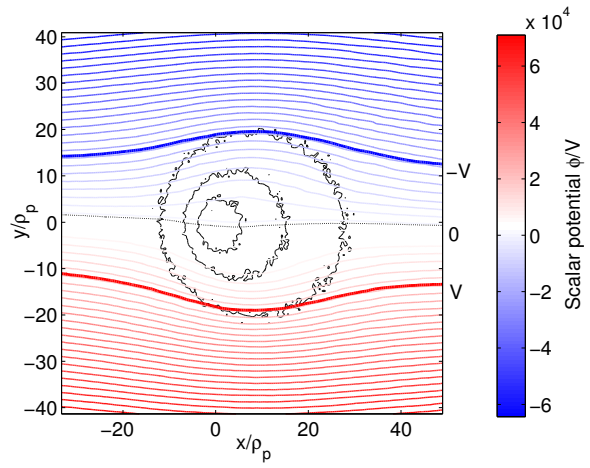

Figure 3.1: Contours of scalar potential ϕ (red and blue) and density (black) across a typical $10\rho_p$ proton plasma blob at an early time $t = t_\Omega$ in the simulation, in the blob's initial rest frame. We highlight scalar potential contours which pass along the top and bottom edge of the blob, corresponding to a cross-blob potential difference consistent with $u_{\text{flow}} = 0.2v_A$ and $B_0 = 0.4T$. Note that the gradient of the scalar potential is reduced inside the blob compared to the background flow, where the motional electric field is reduced.

Dunlop, 1986; Chapman and Schwartz, 1987; Hassam and Huba, 1987]. These simulations have addressed obstacles in fast, super-Alfvénic flows, with an obstacle size $R \ll \rho_i$, the ion gyro-radius. Here we present simulations for an unexplored intermediate range, applicable to tokamak blobs, for which we have a slow, sub-Alfvénic background flow, and obstacle size $R \gtrsim \rho_i$.

In this Chapter we examine the transport and evolution of ion gyro-scale blobs within the confined plasma, ranging from ρ_i to $10\rho_i$ in radius, where the background ion gyro-radius $\rho_i = \sqrt{2m_i kT_i}/qB_0$ for ions of mass m_i in a population with temperature T_i. We discuss the phenomena which arise both as a result of fluid-like bulk flow and the interaction of ions with gyro-scale inhomogeneities. These features include the advection of the blob with the flow, the development of an internal twin-celled vortex pattern, and Kelvin-Helmholtz instability in the tail produced downstream of the blob. The blobs are found to evolve asymmetrically due to the effects of finite ion Larmor radius, with a stronger effect for blobs of smaller radius. The work presented in this Chapter has been published in [Gingell et al., 2012].

3.2 Hybrid Model

A detailed description of the general hybrid method can be found in [Winske et al., 2003] and Chapter 2. The hybrid model treats ions kinetically as particles acted upon by the Lorentz force. These particles follow discretised trajectories in a continuous space space $(\mathbf{x}, \mathbf{v})$. Electric and magnetic fields are evolved self-consistently to second order accuracy in time and space, on a staggered grid. To derive this model, the following assumptions are made: inertia-less electrons; $\nabla \cdot \mathbf{E}$ is negligible on length scales of interest, implying charge neutrality such that $en_e = q_i n_i$ for a single ion species i; collisionless plasma; and an ideal, isothermal electron gas, $\nabla \cdot \vec{\mathbf{P}}_\mathbf{e} = \nabla p_e = kT_e \nabla n_e$. We take the Darwin limit[Hewett, 1994] of Maxwell's equations, which neglects displacement current and hence eliminates fast electromagnetic modes. It is important to note that, under these assumptions, electric fields cannot arise from charge separation; hence electric fields are purely motional in origin. This level of model description allows for the propagation of Alfvén and magnetoacoustic waves, ion cyclotron waves, lower hybrid waves and whistler waves. However, since whistler waves are undamped at the electron gyrofrequency due to the neglect of electron gyration, numerical damping must be applied to the electromagnetic fields to prevent their unstable growth, as discussed in Section 2.3.1.

3.3 Initial Conditions and Simulation Geometry

For the hybrid model presented here, each ion follows a trajectory in a six dimensional phase space. Vector fields **E**, **B** and **J** vary in two dimensional configuration space (x, y) and in time, and are evolved on a staggered two dimensional Cartesian grid with three components at each grid point, e.g. $E_{x,y,z}(x, y, t)$.

The grid size is chosen to be smaller than all ion gyro-scales in the system by approximately an order of magnitude. The box size is then chosen to be sufficiently large to capture the full evolution of the moving plasma blob and is typically 450 ion Larmor radii. The time step is determined by CFL condition and is on the order of 10^5 time steps per ion gyro-period. We use sufficient particles per cell to fully represent the ion velocity distribution and a typical simulation is 2×10^7 total computational particles.

Blobs are set up as flux ropes with Gaussian spatial profiles for enhancements of particle number density, and depressions of magnetic field strength out of the simulation plane, B_z (Figure 3.2). The magnitudes of the Gaussian enhancements and depressions are chosen such that blobs are set up in pressure equilibrium with the

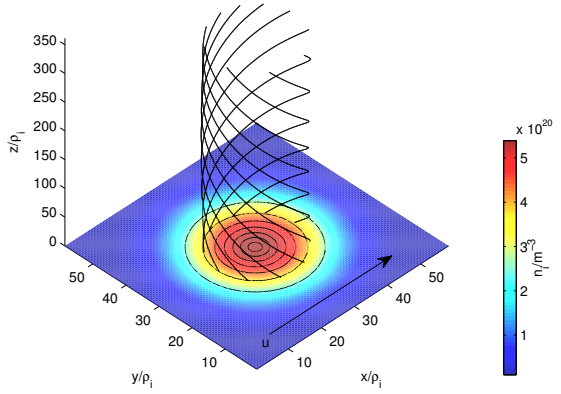

Figure 3.2: Initial conditions of the simulated blobs. Magnetic field lines are plotted in black, extended out of the simulation plane to display the flux rope structure, with the number density in colour for a blob of radius $10\rho_i$.

background flowing plasma, balancing combined gas and magnetic pressures. The incorporation of a finite Larmor radius kinetic description for the ions, however, leads to a small force imbalance for particles in inhomogeneous regions. The background plasma parameters are chosen to be approximately characteristic of edge conditions in a medium-size tokamak such as MAST, with number density $n_0 = 10^{19}\mathrm{m}^{-3}$, magnetic field $B_{z,0} = 0.4\mathrm{T}$, ion and electron temperature $T_0 = 4 \times 10^6\mathrm{K}$, and ion gyro-radius $\rho_i = 8 \times 10^{-3}\mathrm{m}$. Other parameters, notably those characterising the blobs and the background flow speed, are chosen with a view to achieving significant temporal evolution given the spatial resolution required and the computational resource available. The background is initialised flowing transversely to the magnetic field at speed $u_0 = 0.2v_A$, and the simulations are carried out in the initial rest frame of the blob. Conversely in the rest frame of the background flow, the blob initially moves transversely to the magnetic field with velocity $-u_0$. The initial distribution function of particles in the simulation is therefore given by

$$f_0(\mathbf{x},\mathbf{u}) \propto \left(n_0 + (n_{\mathrm{blob}} - n_0)\exp\left[-\frac{(\mathbf{x}-\mathbf{x}_c)^2}{2R_b}\right]\right)\exp\left[-\frac{(\mathbf{u}-\mathbf{u}_{\mathrm{bulk}}(\mathbf{x}))^2}{2u_{\mathrm{th}}(\mathbf{x})}\right] \quad (3.1)$$

where n_{blob} is the peak blob density, $\mathbf{x}_c$ is the position in configuration space of the blob's centre, R_b is the blob radius, $u_{\mathrm{th}}(\mathbf{x})$ is the thermal velocity, and the local

Table 3.1: Physical and numerical parameters for blob simulations in this paper.

Parameter	
Background ion gyro-radius, ρ_i	8×10^{-3}m
Background ion gyro-period, t_Ω	1.6×10^{-7}s
Spatial resolution, $\Delta x, \Delta y$	$0.4\rho_i$
Simulation domain	$960\Delta x$, $450\rho_i$
Total particles	2×10^7
Background magnetic field, $\mathbf{B}_0$	0.4T
Internal magnetic field, $\mathbf{B}_{\text{blob}}$	0.08T
Background number density, n_0	10^{19}m^{-3}
Peak number density, n_{blob}	$55n_0$
Temperature, T_0	4×10^6K
Background ion gyro-period, t_Ω	1.6×10^{-7}s
Alfvén speed, v_A	$2.8 \times 10^6\text{ms}^{-1}$
Sound speed, c_s	$2.3 \times 10^5\text{ms}^{-1}$
Internal plasma beta, β_{blob}	12
Background plasma beta, β_{flow}	0.01
Electron Debye length, λ_D	4.4×10^{-5}m

bulk velocity is given by

$$\mathbf{u}_{\text{bulk}}(\mathbf{x}) = \mathbf{u}_{\text{flow}} \left(1 - \exp\left[-\frac{(\mathbf{x} - \mathbf{x}_c)^2}{2R_b}\right]\right). \tag{3.2}$$

Numerical and physical parameters associated with this geometry and initial condition are listed comprehensively in Table 3.3.

As the initial $B_{x,y}$ magnetic field components of the flux rope structure is much smaller than the perpendicular B_z, wave modes are dominated by those which propagate for $\mathbf{B} \perp \mathbf{k}$. Thus magnetoacoustic waves dominate over Alfvén and whistler waves. Likewise, the magnetic tension force $(\mathbf{B} \cdot \nabla)\,\mathbf{B}$ is small compared to the magnetic pressure force $\nabla\left(B^2/2\right)$.

The six different scenarios are analysed in this paper, for blobs of radii varying from ρ_i to 10 ρ_i. In each case, the magnetic field strength and density at the blobs' centres are the same, such that the total mass of the blobs scales with the square of their radii.

3.4 Simulation Results

Here we present the results of hybrid code simulations of the evolution of ion gyroscale blobs over several ion gyroperiods. The simulations reveal five key elements of the evolution, to be discussed at greater length below: the advection of the

blobs downstream in the background flow; the development of an internal twin-celled convection pattern; the growth of ion gyro-scale structures, both internal and external to the evolving blob; asymmetry in the growth of a tail behind the blob; and the formation of an asymmetric Kelvin-Helmholtz instability in the tail.

The analysis begins with a description of the bulk evolution for a blob with radius $R_b \gg \rho_i$, for which fluid approximations are more appropriate, including the advection due to momentum transfer from flow to blob and the development of the twin convection vortices inside the blob. A detailed account of the asymmetry which develops in these vortices for smaller blobs with radius $R_b \sim \rho_i$ follows, together with a discussion of features unique to those blobs. Finally we examine the formation of the asymmetric Kelvin-Helmholtz instability and its dependence on blob radius.

3.4.1 Fluid-like Phenomena

Snapshots of the blobs in ion number density as they evolve in time are given for $R_b \gg \rho_i$ blobs in Figure 3.3. The clearest features of the evolution of these blobs, with radii ranging from 6 to 10 ion gyro-radii, are related to bulk plasma flow rather than ion kinetic effects due to individual ion particle interactions. Two of these features, the advection of the blob and vortex generation, are described below.

3.4.1.1 Bulk Evolution

As a result of the difference in velocity between the blob and background plasma flow, the background plasma is seen to pile up on the upstream edge, resulting in an increase in the number density in that region. The interaction between this background plasma and the blob, here acting as an obstacle, leads to momentum transfer in the flow direction from the background to the blob. In the initial frame of reference of the blob, as shown in Figure 3.3, this leads to advection of the blob plasma in the flow direction. Trajectories of the centre of mass for blobs of radius $R_b \gg \rho_i$ are given in Figure 3.4. These trajectories display approximately symmetric advection of the large blobs, with a maximum deviation of approximately $0.1\rho_i$ after seven ion gyro-periods.

In the case of an initially stationary blob of plasma with radius $R_b \gg \rho_i$ in a magnetic field, the expected solution under purely fluid assumptions is the deflection of background flow around the blob, with two oppositely directed vorticity cells within its upper and lower halves. Such a solution would be perfectly antisymmetric in the up-down direction (as in [Hill, 1894]). The vorticity cells may be generated in part by momentum transfer around perturbations which grow with the onset of

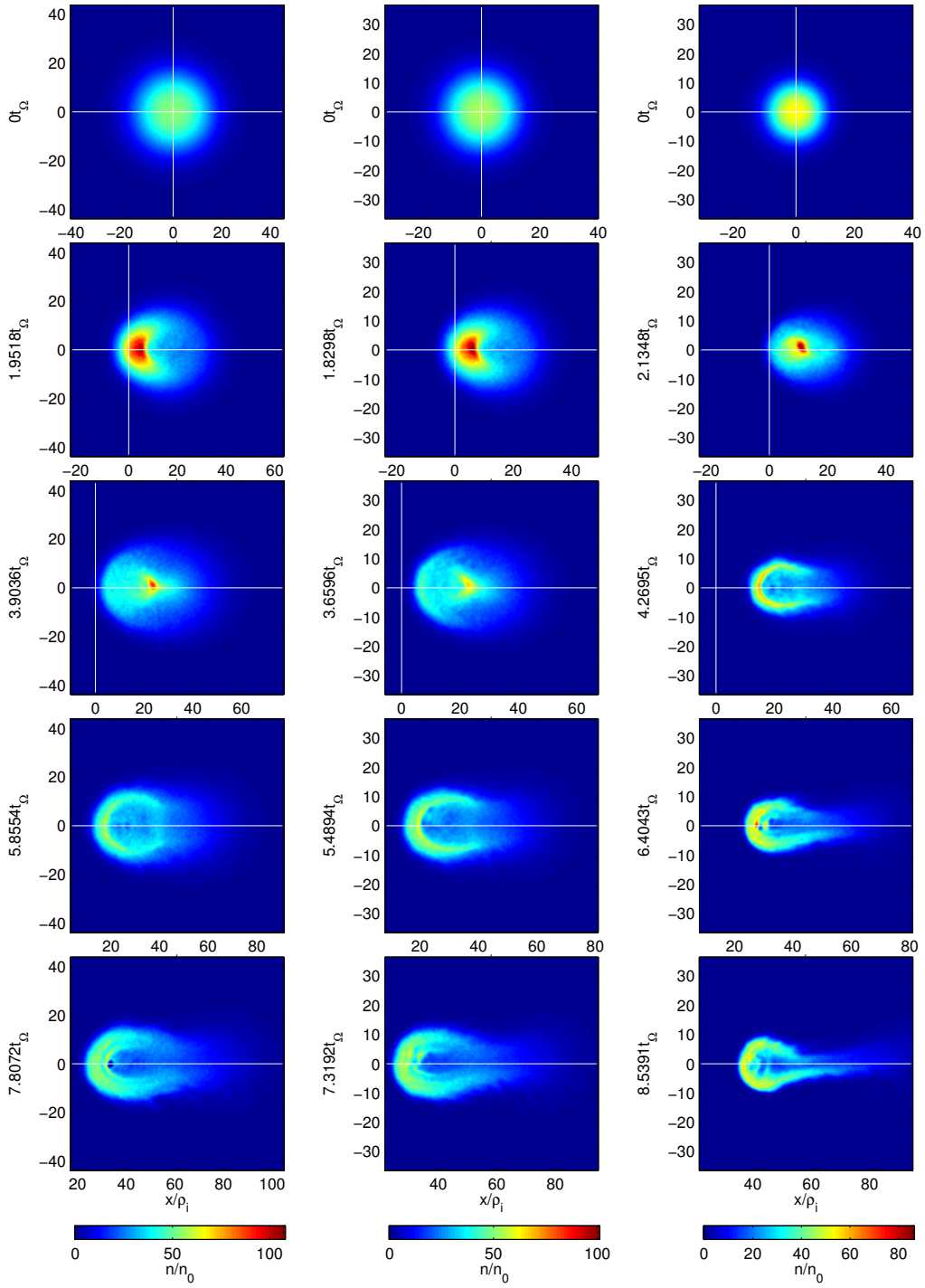

Figure 3.3: Number density colour maps for the time evolution of blobs with radii $R_b/\rho_i = 10$ (left column), 8 (centre), 6 (right). The white lines mark the starting position of the blob in the x- and y-direction. These larger blobs are advected to the right, develop an asymmetric tail, and evolve internal structures on the order of the ion gyroradius. At late times, a Kelvin-Helmholtz instability grows on the lower edges of the blobs, and can be seen in greater detail in Figure 3.12.

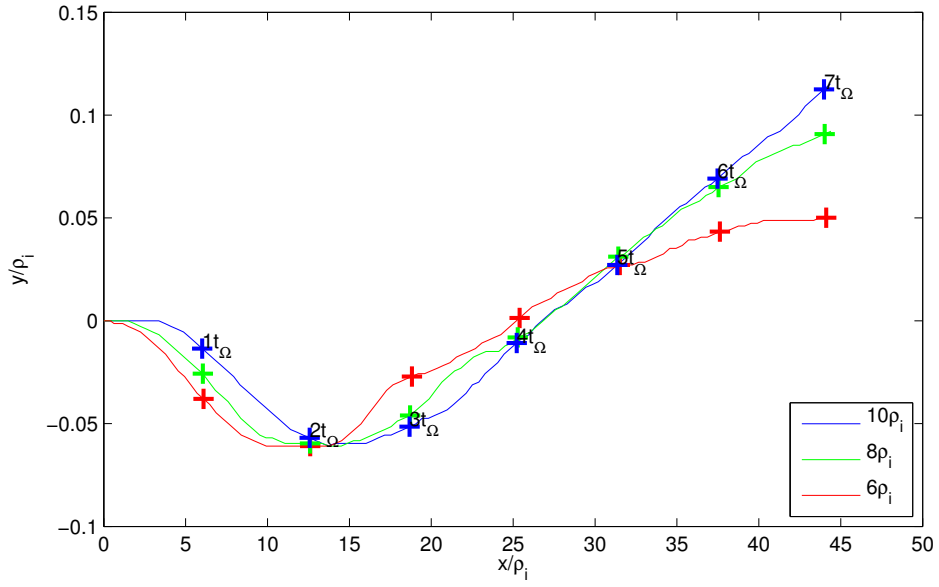

Figure 3.4: Trajectories in the x-y plane of the centre of mass for blobs of radius 6-10ρ_i from $t = 0$ until approximately 7 gyroperiods have elapsed. The centre of mass is calculated by taking moments over only those grid cells which have a number density greater than twice that of the background.

Kelvin-Helmholtz instability at the shear boundary between stationary blob plasma and flowing background plasma. Calculated streamlines for the largest blob, of radius 10ρ_i, are given in Figure 3.4.1.1, and display the twin-celled vortex pattern.

3.4.2 Kinetic Phenomena

For blobs with radius $R_b \sim \rho_i$, snapshots of their ion number density as they evolve in time are given in Figure 3.6. The clearest features of the evolution of these blobs, whose radii range from 1 to 4 ion gyro-radii, are the growth of structures on the ion gyro-scale, and the introduction of asymmetries into the fluid-like phenomena. This asymmetry is most clear in the tails that form downstream of the blob, with a larger, more dense tail forming on the lower edge of the blobs.

The asymmetry is also apparent in the trajectories of individual particles, as seen particularly for a blob of radius 2ρ_i in Figure 3.7, but also for a blob of radius 10ρ_i. The underlying physics behind this asymmetry is a direct consequence of the inclusion of ion gyration in the hybrid model, and is described in the following section.

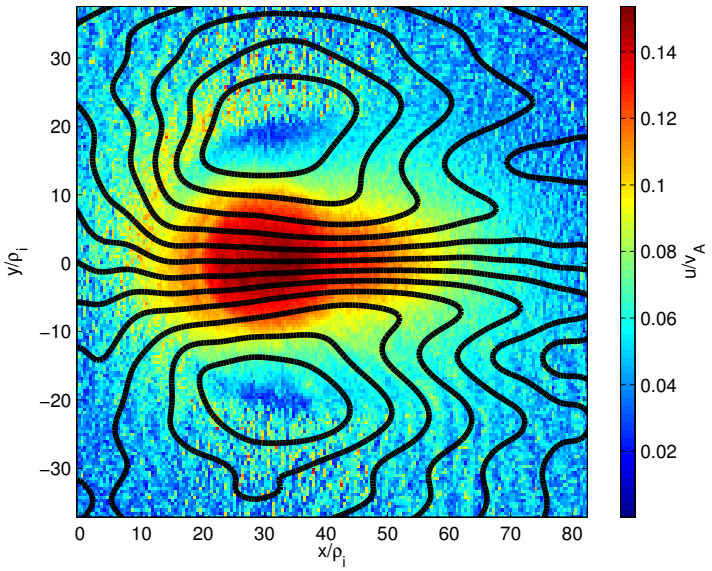

Figure 3.5: Approximate streamlines for a blob of radius $10\rho_i$ calculated under the assumption of incompressible flow, $\nabla \cdot \mathbf{u} = 0$. Streamlines are plotted in the rest frame of the flow, with the magnitude of the velocity also given in colour. Though we do not in fact have incompressible flow, these streamlines suffice to illustrate the two convection cells formed on the upper and lower sides of the blob by momentum transfer which may be due to Kelvin-Helmholtz instability.

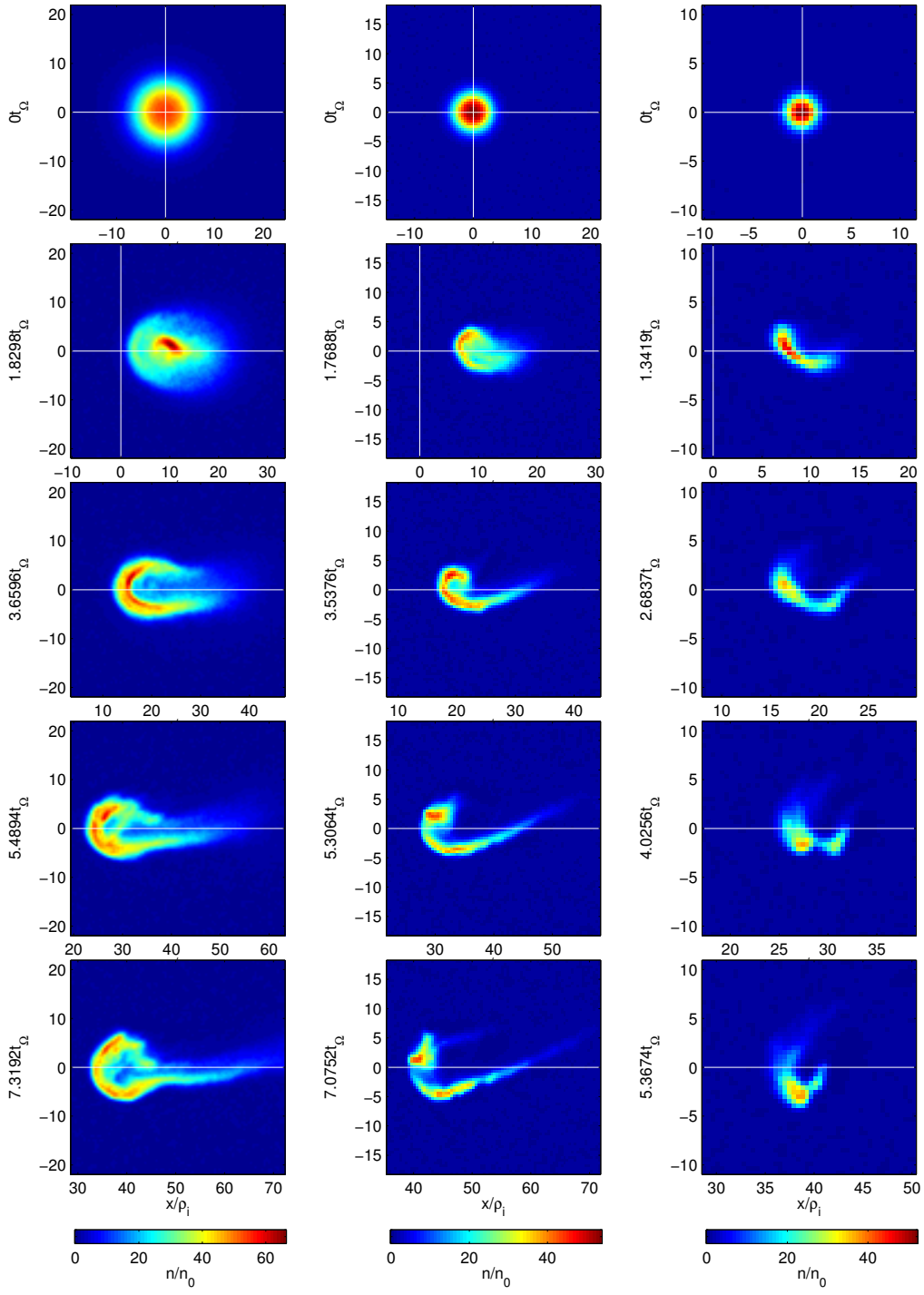

Figure 3.6: Number density colour maps for the evolution of a blob with radii $R_b/\rho_i = 4$ (left column), 2 (centre), 1 (right). The white lines mark the starting position of the blob in the x- and y-direction. The small blobs are advected to the right, along the direction of the background flow, and develop structures directly related to the gyration of individual ions. There is a clear up-down asymmetry in the growth of the tail that forms downstream of the blob as it evolves.

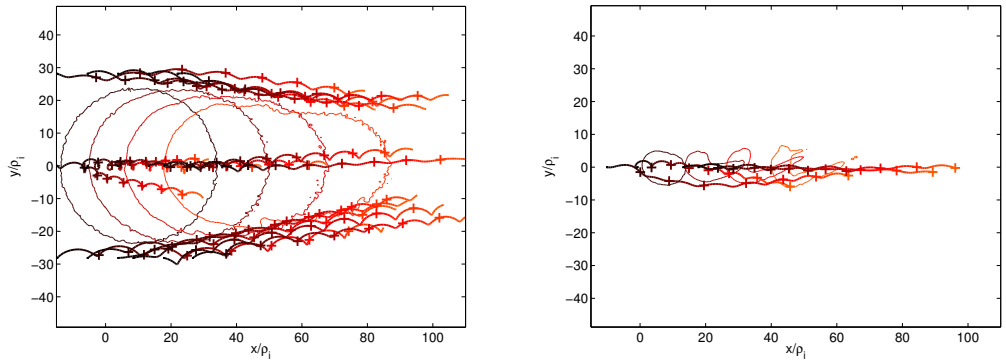

Figure 3.7: Particle trajectories in the $10\rho_i$ blob (left) and $2\rho_i$ blob (right), for particles positioned initially on lines on the centre, top and bottom, upstream and inside the blob, overlaid on contours of number density after 1, 3, 5 and 7 gyroperiods. The colour of the particle tracks and contours is related to the time, with black being the start of the simulation, and red the end. Ticks are given on the particle trajectories at each complete gyroperiod. Of those particles which begin on the central, symmetric line, many are pushed towards the lower edge of the blob by the FLR symmetry breaking effect within a few ion gyroperiods.

3.4.2.1 Finite Larmor Radius Symmetry Breaking

In the rest frame of the background flow, we have two distinct populations of ions in velocity space: these comprise the stationary background and the moving ion gyroscale blob. Since an ion traverses much of the blob as it gyrates in the magnetic field, we expect gyromotion to play a significant role in the dynamics and evolution of both ion populations. The chirality of ion gyration can thus break the symmetry of the evolution of an otherwise symmetric blob. We can describe this asymmetry mathematically as follows. From the Vlasov equation,

$$\frac{\partial f_\alpha}{\partial t} + \mathbf{v} \cdot \nabla f_\alpha + \frac{q_\alpha}{m_\alpha} \left(\mathbf{E} + \mathbf{v}_\alpha \times \mathbf{B} \right) \cdot \nabla_{\mathbf{v}} f_\alpha = 0, \tag{3.3}$$

taking the second moment by multiplying by $\mathbf{vv}$ and integrating over velocity space, we arrive at the bulk momentum equation for an ion species α:

$$n_\alpha m_\alpha \frac{\mathrm{d}\mathbf{v}_\alpha}{\mathrm{d}t} = q_\alpha n_\alpha \left(\mathbf{E} + \mathbf{v}_\alpha \times \mathbf{B} \right) - \nabla p_\alpha. \tag{3.4}$$

Using the Ohm's law for our hybrid method as in 2.37,

$$\mathbf{E} = -\frac{1}{e n_e} \left(k_b T_e \nabla n_e - \frac{(\nabla \times \mathbf{B}) \times \mathbf{B}}{\mu_0} + \mathbf{J}_i \times \mathbf{B} \right), \tag{3.5}$$

together with Ampère's law in the low frequency limit,

$$\nabla \times \mathbf{B} = \mu_0 \mathbf{J} = \mu_0 e \left(\sum_\alpha n_\alpha \mathbf{v}_\alpha - n\mathbf{v}_e \right), \tag{3.6}$$

$$\mathbf{v}_e = -\frac{\mathbf{J}}{en} + \frac{1}{n} \sum_\alpha n_\alpha \mathbf{v}_\alpha \tag{3.7}$$

and with a proton plasma, we can eliminate the electron fluid velocity $\mathbf{v}_e$ from Ohm's Law as follows:

$$\mathbf{E} = \left(\frac{\mathbf{J}}{en} - \frac{1}{n} \sum_\alpha n_\alpha \mathbf{v}_\alpha \right) \times \mathbf{B} - \frac{1}{en} \nabla p_e \tag{3.8}$$

Substituting 3.8 into 3.4, we can express the ion momentum equation in the form [Chapman and Dunlop, 1986]:

$$\begin{aligned} m_\alpha n_\alpha \frac{D\mathbf{v}_\alpha}{Dt} &= en_\alpha \left(\mathbf{v}_\alpha - \frac{1}{n} \sum_{\alpha'} n_{\alpha'} \mathbf{v}_{\alpha'} \right) \times \mathbf{B} \\ &\quad + \frac{n_\alpha}{n} \left(\mathbf{J} \times \mathbf{B} - \nabla p_e \right) - \nabla p_\alpha. \end{aligned} \tag{3.9}$$

While the last terms on the RHS arise from conventional single fluid MHD forces for ion species α, the first term on the RHS represents an asymmetry present only in spatially inhomogeneous regions in which there is a difference between the mean velocities of different populations of ions. In our case, these populations are the ions in the blob and those in the background plasma.

In order to understand the effect of the asymmetric term in Equation 3.9 on a plasma with finite ion Larmor radius, we can consider the effect of a moving frame of reference on individual particle dynamics, and the associated appearance of motional electric fields. Let us consider the two frames of reference shown in Figure 3.8. In Frame 1 the background plasma is stationary, with the blob plasma moving with velocity $\mathbf{v}$ in the $-x$ direction. Frame 2 is moving with velocity $\mathbf{v}$ with respect to Frame 1, such that the background plasma is flowing with velocity $\mathbf{u}_{\text{flow}} = -\mathbf{v}$ and the blob plasma is stationary. The simulations presented in this paper are carried out in Frame 2.

A test particle in the background plasma in Frame 1, with components of velocity in the x-y plane, will gyrate with a circular trajectory around the perpendicular magnetic field lines as shown in Figure 3.9. However if we transform into Frame 2, the electromagnetic fields are subject to the following transformations in

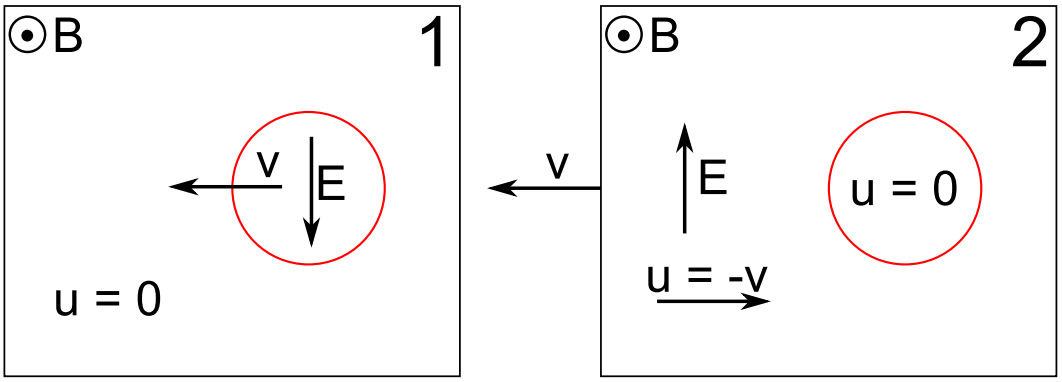

Figure 3.8: Vector directions internal and external to the blob (red) for the rest frames of the background flow plasma (Frame 1) and blob plasma (Frame 2).

the non-relativistic case:

$$\mathbf{B}_2 = \mathbf{B}_1 \tag{3.10}$$

$$\mathbf{E}_2 = \mathbf{E}_1 - \mathbf{v} \times \mathbf{B}_1. \tag{3.11}$$

In Frame 2, charged particles in the background are thus subject to a motional electric field $\mathbf{E}_2$ which arises as a result of a frame moving relative to a magnetic field. If the frame velocity $\mathbf{v}$ is perpendicular to $\mathbf{B}$, the gyrating particle in Frame 1 is, in this moving frame, subject to an $\mathbf{E} \times \mathbf{B}$ drift, and demonstrates a cycloid orbit as shown in Figure 3.9. This describes the trajectories of background particles in the simulations, and the source of the background electric field $\mathbf{E}_y$ in the absence of charge separation.

Particles which are stationary in Frame 2, i.e. those initialised in the blob, are accelerated by this motional electric field if they leave the spatial region that is dominated by blob ions and enter the background flowing plasma. This acceleration occurs initially in the direction of the motional electric field $\mathbf{E}_2$, and leads to a momentum gain of the blob particles in the $\mathbf{v} \times \mathbf{B} = -\mathbf{u}_{\text{flow}} \times \mathbf{B}$ direction. Ultimately, such particles are "picked-up" by the background flow, with a cycloid trajectory in the $\mathbf{E_2} \times \mathbf{B}$ direction with gyro-radius $2u_0/\Omega_{\text{c,i}}$.

Following the same analysis in the rest frame of the background flow, Frame 1, such that the blob is moving with velocity $\mathbf{v}$ and particles in the background are initially stationary, it becomes clear that in this frame, a motional electric field $\mathbf{E} = -\mathbf{v} \times \mathbf{B} = \mathbf{u}_{\text{flow}} \times \mathbf{B}$ exists within the blob. Hence, particles initially within the stationary flow, which subsequently enter the spatial region dominated by moving

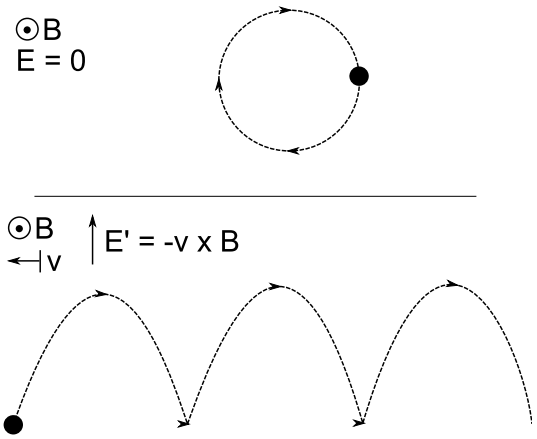

Figure 3.9: Single particle trajectories for an ion with velocity perpendicular to a background magnetic field in a stationary (top) and moving (bottom) frame of reference.

blob ions, are there accelerated in the $\mathbf{E}_1 = -\mathbf{E}_2$ direction and proceed with cycloid orbits in the $\mathbf{E}_1 \times \mathbf{B}$ direction. We emphasise again that the hybrid code calculate particle-field interactions directly and self-consistently at the level of each individual ion.

The overall effect of these motional electric fields is a deflection of the blob plasma in the $-\mathbf{u}_{\text{flow}} \times \mathbf{B}$ $(+y)$ direction at the upstream edge of the blob, and a deflection of the background flow plasma in the $\mathbf{u}_{\text{flow}} \times \mathbf{B}$ $(-y)$ direction. A net momentum gain for the blob or flow ion population in the y direction can only occur for finite Larmor radius ions: the gyration caused by the perpendicular magnetic field breaks the symmetry that would result from the asymmetric term in 3.9 under multi-fluid assumptions including zero Larmor radius. This form of finite Larmor radius symmetry breaking has been observed in the AMPTE artificial comets released into the solar wind in 1984 [Valenzuela et al., 1986], small scale natural comets [Terasawa et al., 1986] and the structure of the magnetospheres of Mars [Lundin et al., 1989] and Venus [Phillips et al., 1987]

3.4.2.2 Asymmetry in Bulk Evolution

As noted previously, blobs are advected downstream with the x-directed flow because momentum is transferred to the blob from the background. However if we examine the trajectory of the centre of mass for the blobs, an asymmetry in the y-direction becomes apparent. Figure 3.10 reveals that blobs with $R_b \sim \rho_i$ exhibit a small but measurable downward deflection of up to a full gyroradius over 5.5 gyroperiods, an order of magnitude greater than the negligible deflection for larger blobs seen in

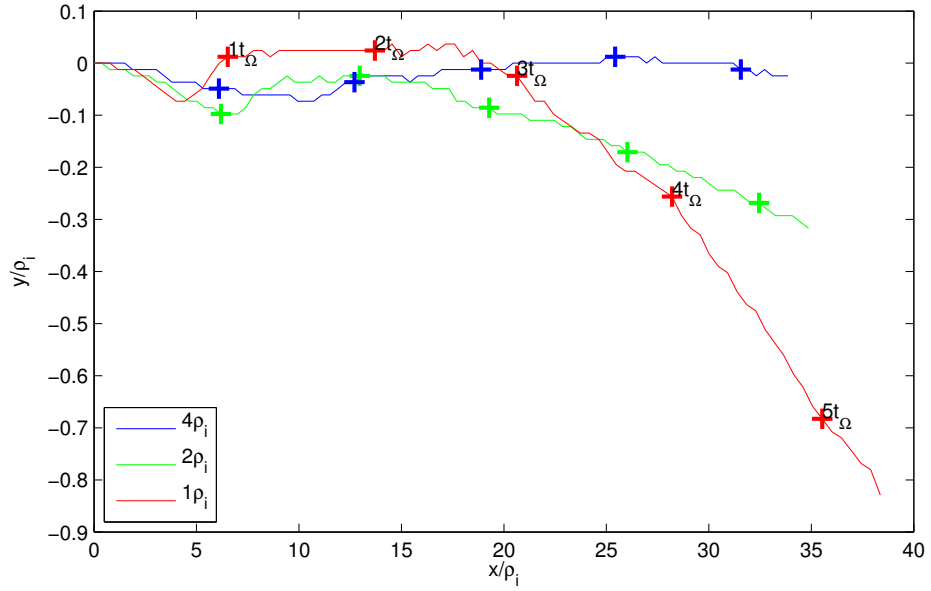

Figure 3.10: Trajectories in the x-y plane of the centre of mass for blobs of radius 1-4ρ_i from $t = 0$ until approximately 5.5 gyroperiods have elapsed. The centre of mass is calculated by taking moments over only those grid cells which have a number density greater than twice that of the background. There is greater poloidal deflection for smaller blobs.

the largely symmetric trajectories in Figure 3.4. This is a result of the downward deflection of the background flow by the FLR symmetry breaking mechanism, which then causes momentum transfer in the $\mathbf{u}_{\text{flow}} \times \mathbf{B}$ direction from the flow to the blob, pulling the blob plasma down. Local momentum transfer is mediated by the motional electric field associated with the locally dominant ion population.

We also see an asymmetry develop in the twin-celled convection pattern for the blobs with $R_b \sim \rho_i$. Due to the FLR symmetry breaking mechanism, the twin-vortex solution under a kinetic ion treatment deviates from the symmetric solution that would emerge from a purely fluid description. The difference in flow speeds between the upper and lower sides of the blob, which arises from the FLR symmetry breaking, causes the vorticity cells to grow asymmetrically, with a larger, faster flowing cell on the lower edge compared to a smaller, more slowly rotating cell on the upper edge. These asymmetric vorticity cells are shown in Figure 3.11, and are more pronounced for blobs of smaller radius. The difference in flow speeds at the leading edge of these vorticity cells contributes to the asymmetry which develops in the tails of the blobs for which $R_b \sim \rho_i$. Such blobs appear to have two tails, with a shorter tail forming on the upper edge, and a longer tail forming on the lower

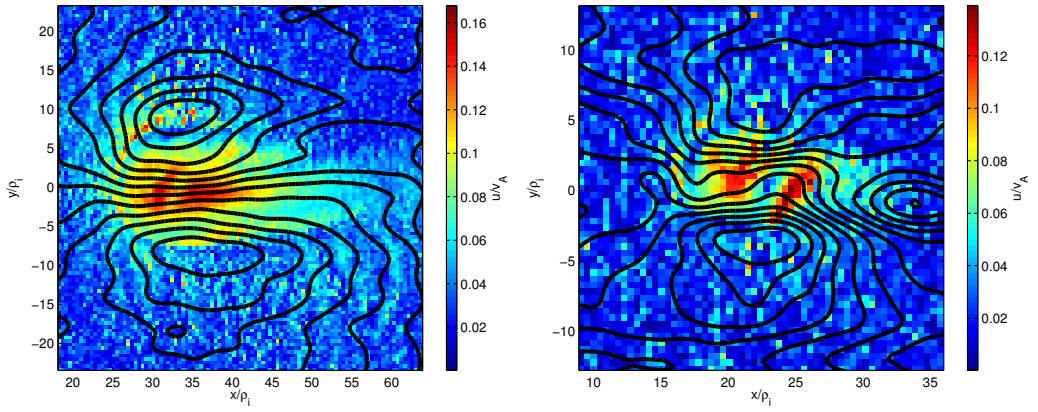

Figure 3.11: Approximate streamlines for blobs of radius $4\rho_i$ (left) and ρ_i (right) calculated under the assumption of incompressible flow, $\nabla \cdot \mathbf{u} = 0$, after approximately 6 and 3 gyroperiods respectively. Streamlines are plotted in the rest frame of the flow, with the magnitude of the velocity also given in colour. The twin-celled convection pattern internal to the blob is asymmetric, with a larger cell on the lower edge than the upper edge.

edge. For the smallest blob at $R_b = \rho_i$, no upper tail forms. This kind of clear asymmetry is not unique to these intermediate $R_b \sim \rho_i$ blobs, and has also been seen for obstacles with $R \ll \rho_i$. For example, the effect is visible in observations of the comet-like AMPTE solar wind releases [Valenzuela et al., 1986].

3.4.3 Kelvin-Helmholtz Instability

At the boundaries between the blob and background plasmas, the sheared flow develops a Kelvin-Helmholtz (K-H) instability with structures on the ion gyroscale. The consequences of the instability are visible on the lower edges of the tails of the larger blobs in Figure 3.3, and more clearly for a large blob in Figure 3.12.

The magnetised fluid K-H instability arises when [Treumann and Baumjohann, 1997]

$$(\mathbf{k}.\mathbf{v_0})^2 > \frac{n_1 + n_2}{n_1 n_2}\left[n_1\left(\mathbf{k}.\mathbf{v}_{A1}\right)^2 + n_2\left(\mathbf{k}.\mathbf{v}_{A2}\right)^2\right], \tag{3.12}$$

where $\mathbf{v}_0$ is the relative shear velocity, $n_{1,2}$ are the densities of the respective layers, and $v_{A1,2}$ are the Alfvén speeds. The condition 3.12 is more easily satisfied for faster shear velocities, and is unconditionally satisfied when the magnetic fields are perpendicular to the shear, which is the case for these blob simulations. This instability enables momentum transfer between the two sheared fluids, contributing

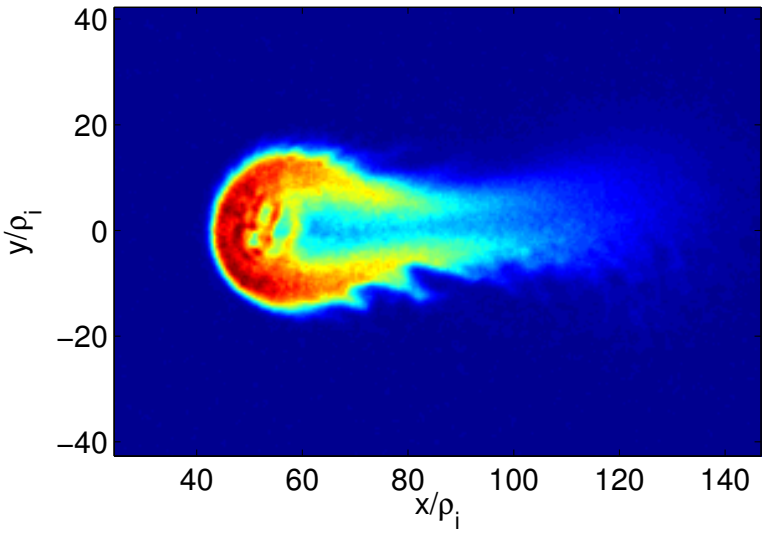

Figure 3.12: Number density plot for a blob of radius $R_b = 10\rho_i$ after 11 gyroperiods, demonstrating the asymmetric growth of a Kelvin-Helmholtz instability on the upper and lower edges of the blob, and in the tail. Note that the instability has grown much more quickly on the lower edge, and with associated structures whose size is much larger than those on the upper edge.

to the internal convection pattern described above.

An analytical expression for the growth rate of the Kevin-Helmholtz instability can be obtained for an MHD frame, with an infinitely thin boundary, incompressible media, and a simple geometry with velocities, magnetic field and tangential wave vector k_T aligned in the same direction. In this case, the growth rate is simply proportional to k_T [Belmont and Chanteur, 1989]. However, when we include compressibility and a more complex geometry, numerical and parametric studies are required. With the additional assumption of a finite boundary width a, such studies reveal the growth rate reaches a maximum value for $ka \approx 1$. Hence we expect the fastest growing mode to have a wavelength on the order of the radius of the blob.

An analytic expression can be derived for the growth rate of the K-H instability for the case of an incompressible plasma with a finite Larmor radius and a finite thickness of the boundary layer [Nagano, 1979]. The physics of finite ion Larmor radius enters through the magnetic viscosity $\nu = \rho_{\mathrm{i}}^2 \Omega_{\mathrm{c,i}}/4$. We define the non-dimensional parameters $\omega^* = \omega L_0/v_{A2}$, $k^* = kL_0$, $\alpha = \rho_{01}/\rho_{02}$, $M = u_{02}/v_{A2}$, $s = v_{A1}/v_{A2}$, and $\nu_i^* = \nu_i/v_{Ai}L_0$; here ρ_{0i} is the density in layer i, and L_0 is the characteristic length. The growth rate Γ^* is the real part of ω^*, as derived in [Nagano,

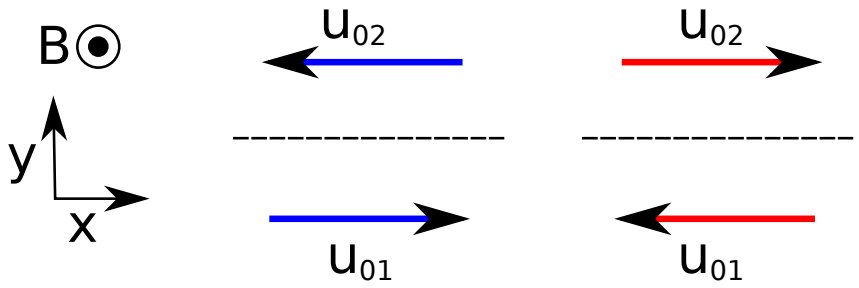

Figure 3.13: Background flow orientations for two cases described by Equation 3.13, for a background field **B** out of the plane of the paper. The boundary is represented by a dashed line. Velocities u_0 for layers 1 and 2 are orientated as on the left (blue arrows) for the case $j = 1$, and are orientated as on the right (red arrows) for the case $j = 2$.

1979], given by:

$$\Gamma^* = \frac{k^*}{\alpha+1}\left[(\alpha+1)\,M\left(M+(-1)^j 2\nu_2^* k^*\right) - \left(M-(-1)^j\left(\alpha\nu_1^* s-\nu_2^*\right)k^*\right)^2\right]^{1/2}. \tag{3.13}$$

The index $j = 1, 2$ corresponds to two cases for which the velocities on each side of the boundary are oppositely directed relative to the background magnetic field. An illustration of these two cases is shown in Figure 3.4.3. Here, the case $j = 1$ represents the $-y$, lower edge of the blob, and the case $j = 2$ represents the $+y$, upper edge of the blob.

Plots of the theoretical growth rates Γ^* for $j = 1, 2$, calculated using 3.13, for the parameters used in our simulations of a blob of radius $10\rho_i$ are given in Figure 3.4.3. The graph shows this analysis predicts a large disparity between the K-H growth rates and the characteristics of the fastest growing modes that arise on the upper and lower edges of the blobs. On the lower edge, 3.13 predicts a faster growth rate of the instability over all values of k, higher than that expected under MHD assumptions, for which Γ^* is proportional to k^*. For example, for a blob of radius $10\rho_i$ this model predicts a sharp cut off at $k^* = 6$, corresponding to a fastest growing mode with $\lambda = L_0$ which has a growth rate roughly 50 times greater than the fastest growing mode for the upper edge. The scale size of the fastest growing mode for the upper edge is, from this model, expected to be approximately an order of magnitude less than that for the lower edge. This large disparity in the scale sizes of the structures formed by the K-H instability can be observed for our simulations

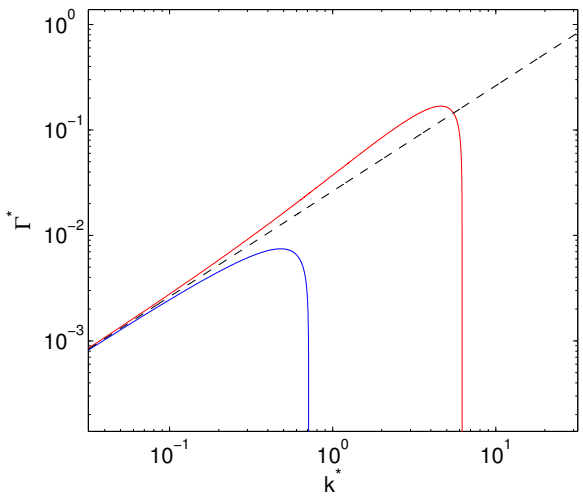

Figure 3.14: Growth rate Γ^* of the K-H instability for an incompressible plasma with the same flow speed on the upper and lower edges. Γ^* is plotted against dimensionless wavenumber k^* for the lower edge (red); upper edge (blue); and under MHD assumptions (dashed line). These theoretical growth rates have been calculated for a blob of radius $10\rho_i$.

in Figure 3.12.

3.5 Alternative Geometries

3.5.1 Hot Blobs

Previous sections of this chapter have discussed isothermal, "cold" blobs with no internal temperature profile. "Hot" blobs (and ELM filaments) which have an internal temperature profile which decreases monotonically from the centre of the blob are described here [D'Ippolito et al., 2004; Myra et al., 2004; Horacek et al., 2010]. In the SOL, hot blobs connected to the sheaths at the end plates acquire an internal radial electric field and thus will rotate. This spin tends to neutralise charge polarisation by mixing and hence increases coherence and decreases the blob's radial $\mathbf{E} \times \mathbf{B}$ velocity [Myra et al., 2004].

As above, we simulate these hot blobs before they cross the LCFS. Hence, these blobs are not sheath-connected, and will not rotate. However, the simulations presented here provide insight into the early life of hot blobs. The parameters of two hot blobs presented here, initialised with fast and slow background flows, are shown in Table 3.2. The magnetic field, temperature and density profiles are Gaussian, and initialised in combined pressure balance over the entire domain.

Description	Radius/ρ_i	n_{internal}/n_0	u_{flow}/v_A	$B_{\text{z,internal}}/B_{\text{z,0}}$	T_{internal}/T_0
hot, slow	10	5	0.2	0.2	25
hot, fast	10	5	1	0.2	25

Table 3.2: Parameters for hot blobs discussed in this section, where $n_0 = 10^{19}\text{m}^{-3}$, $B_{\text{z.0}} = 0.4\text{T}$ and $T_0 = 4 \times 10^6 K$.

Snapshots of the blobs in ion number density as they evolve in time are given in Figure 3.15. Although these blobs appear to evolve in a different manner to the blobs described in previous sections, the same basic physics are at work. Figure 3.16 demonstrates using fluid streamlines that the same fundamental dipole vorticity evolves within both the hot blobs as compared to the cold blobs. However, there are significant differences between hot and cold blobs in the evolution of the number density. At early times, a circular shell forms around both slow and fast blobs as a result of ballistic expansion of hot ions in the blob's core, which have a gyro-radius up to 5 times greater than the background ions, or half the radius of the blob itself. Once the ballistic shell has formed, we see a Kelvin-Helmholtz instability develop on the boundary between the shell and internal blob plasmas. This appears to dominate over the mushrooming effect of the same instability on the blob as a whole. The K-H instability on the shell grows more quickly for the fast blob than the slow blob, leading to faster disruption of its structure and a shorter liftime, consistent with the dependence of the growth rate on shear velocity.

Symmetry breaking as a result of finite Larmor radius effects is clearly visible for two aspects of the evolution in Figure 3.15. Firstly, the convection cell vortex on the lower side is seen to grow larger than that on the upper side, as seen for cold blobs in Figure 3.11. Secondly, a deflection of blobs below the line of symmetry is seen at late times. Although this effect has also been observed for small cold blobs in Figure 3.10, we note here the dependence of the deflection on the background flow speed ,as expected from Equation 3.9. The hot blob initialised in a faster flow is seen to be deflected in the $-y$ direction significantly more than its slower counterpart.

3.5.2 Holes

Holes are the inverse of the blobs presented in the previous sections of this chapter. They consist of a density depression and, in this case, a magnetic field enhancement. As above, these blobs are initially isothermal with the background plasma.

Holes can originate near the LCFS, like over-dense blobs, as a consequence of the interchange instability. The theoretical model described in Section 1.3.2.1 suggests that while blobs with higher density than the background plasma are trans-

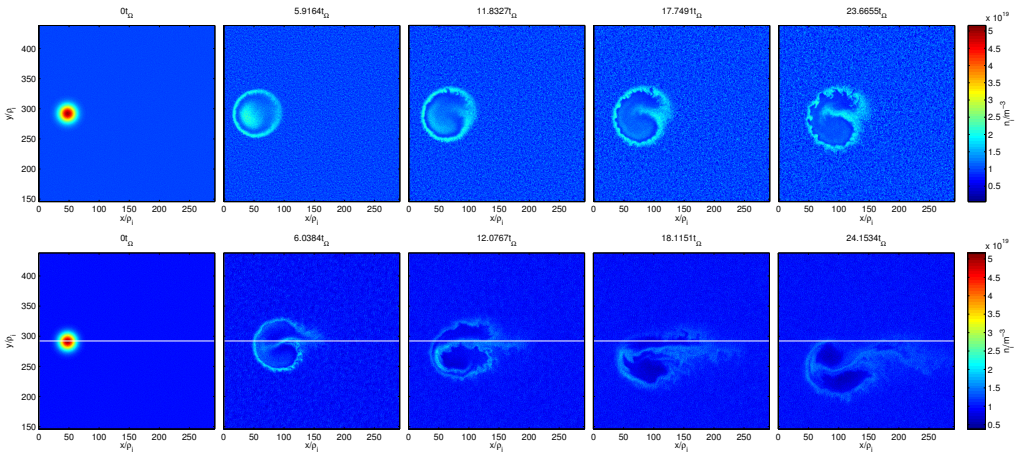

Figure 3.15: Number density color maps for the evolution of a blob in a background flow of $0.2v_A$ (top) and v_A (bottom), with background magnetic field perpendicular to the plane of the page. The white lines mark the starting position of the blob in the x- and y-direction. The frames are shifted in the x-direction to keep the blobs central. Here we see the blobs are advected to the right, along the direction of the background flow, and subject to a growing Kelvin-Helmholtz instability at the boundary between the flow and blob plasmas. An asymmetry in the growth of the K-H instability is visible between the upper and lower edges of the blobs, caused by finite Larmor radius effects as discussed above.

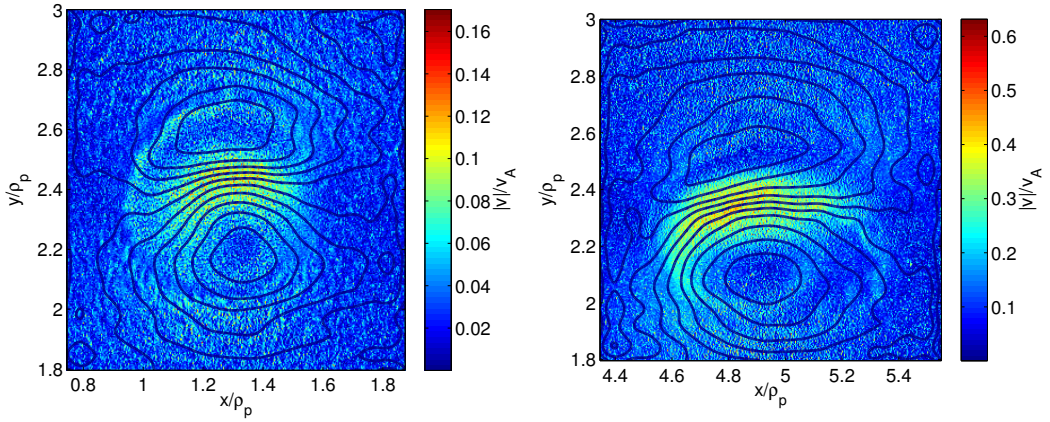

Figure 3.16: Approximate streamlines for hot blobs calculated under the assumption of incompressible flow, $\nabla \cdot \mathbf{u} = 0$. Streamlines are plotted in the rest frame of the blob, with the magnitude of the velocity also given in colour. Though we do not in fact have incompressible flow, these streamlines provide a qualitative indication of the two convection cells formed on the upper and lower sides of the blob by momentum transfer which may be due to the Kelvin-Helmholtz instability.

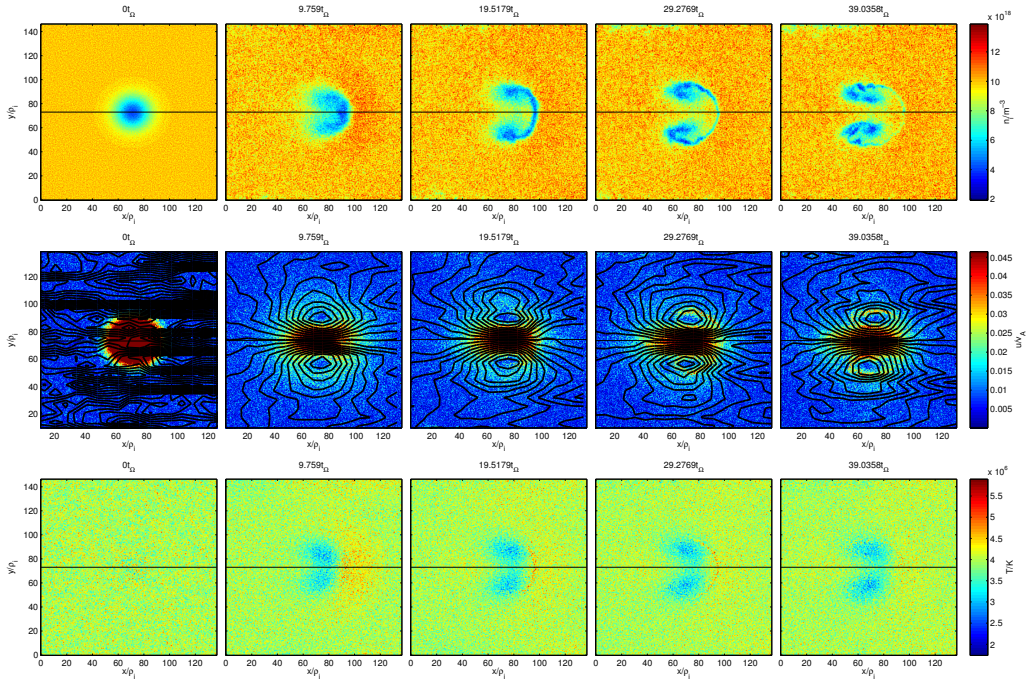

Figure 3.17: Evolution of a $10\rho_i$ hole. Unlike over-dense blobs, this simulation was run in the rest frame of the background, with the hole launched with velocity $0.2v_A$ to the right. As such, for these holes, we expect that the faster flow due to FLR symmetry breaking is on the upper rather than lower edge of the blob. Number density, bulk velocity field and temperature are shown from top to bottom respectively.

ported radially in the direction of the charge polarising force, regions of reduced density (holes) are transported in the opposite direction [Russell et al., 2007]. Just as blobs transport core plasma to the wall, theory suggests holes created near the wall may transport impurities toward the core plasma. Regions in which holes are more common than blobs display negative skewness of the density PDF. In some tokamaks, this has been observed towards the centre of the confined plasma [Boedo et al., 2003].

In general we can expect similar dynamics for holes as for blobs, though the gradients and hence forces and drifts internal to the blob are oppositely directed. Specifically, the density over the blob drops to $0.2n_0$, with associated but increase in the magnetic field strength B_z to maintain combined pressure equilibrium. The evolution of such a hole is shown in Figure 3.17. As with the blobs described in Section 3.4, these holes evolve a dipole vorticity structure, and form a mushroom shape consistent with the dominance of the Kelvin-Helmholtz instability.

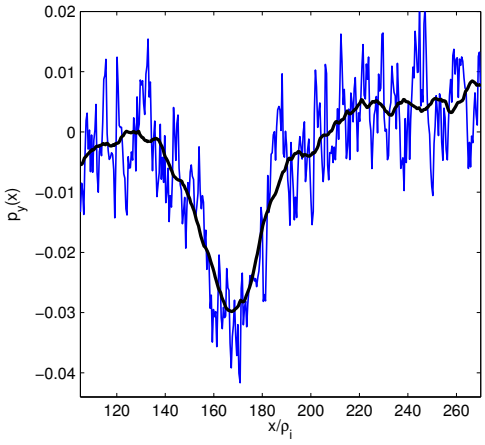

Figure 3.18: y-component of the momentum integrated over the x-direction, $p_y(x)$, for a hole after 40 gyroperiods. The moving average is overlaid in black. Here the asymmetry is oppositely directed due to the opposite flow direction to other blobs, so we expect from left to right a drop then rise in $p_y(x)$. Though the rise on the right is subtle, the drop on the left side of the hole is clear.

Due to the nature of the pressure balance required, the hole is made up of much shallower gradients than the other blobs discussed above, with only a 0.5% rise in magnetic field strength, and a 60% reduction in density over 10 ion gyroradii. Hence, the asymmetry due to finite Larmor radius effects is very weak compared to the other blobs, and even after 40 gyroperiods an asymmetry isn't clear in the density and velocity fields shown in Figure 3.17. A clearer display of the asymmetry is given in Figure 3.18, which shows the bulk y-momentum field $p_y(x)$ over a 1D cut through the intial line of symmetry of the hole. In the fluid case, the profile would be flat. Here, we note a reduction in $p(y)$ at the trailing edge, and an increase in $p(y)$ at the leading edge.

3.6 Conclusions

The preceding results demonstrate how the hybrid model (fluid electrons and fully kinetic ions) embodied in the code captures key elements of the plasma dynamics and the evolution of the fields in ion gyro-scale blobs. Many of the phenomena described above are common to a purely fluid approach to blob simulation, including the advection of blobs with the background flow, the development of a twin-celled vortex structure internal to the blob, and the growth of a Kelvin-Helmholtz instability in the tail formed from blob ejecta. However the substantial asymmetry which we find

develops in these evolving features underlines the need to study small scale blob propagation using a hybrid method. The emergence of structures and gradients on ion gyro lengthscales, both internal to the blobs and at the boundary between the blob and external flowing plasma, further demonstrates the value of such a model. The resolution of ion gyro-scale physics deepens understanding of the mechanisms for momentum transport into and within the evolving blobs, in terms of both the motional electric fields and the non-linear phase of fluid-type instabilities such as Kelvin-Helmholtz.

With regard to the evolution of individual blobs, we conclude that symmetry breaking arising from finite ion Larmor radius effects plays a significant role in the evolution of blobs, in the case where inhomogeneities and their associated gradients cause significant variation in bulk properties over the lengthscale of a single ion gyration. The consequences of this asymmetry include: a poloidal deflection of the blob plasma in the $\mathbf{u} \times \mathbf{B}$ direction; a difference in size between the twin vortices generated internal to the blob; and a difference in the growth rate of the Kelvin-Helmholtz instability between the upper and lower edges of the blob, caused by both a growth of momentum in the background in the $\mathbf{u} \times \mathbf{B}$ direction, and by FLR effects at the shear boundary.

Some of these phenomena are known to arise for $R \ll \rho_i$ obstacles studied in a space science context. However the generation of the internal vortex cells, and their subsequent asymmetry and effect on the blob evolution, is unique to the intermediate scales chosen for this paper; comet-like objects for which $R \ll \rho_i$ cannot form such clear structures.

From the simulations presented, it is clear that the strength of the asymmetry is strongly dependent on the radius of the blob with respect to the ion gyroradius, and hence on the gradient lengthscales of the inhomogeneities associated with the blob. The form of the asymmetry of the evolution of the blob in the flow is also clearly dependent on the size of the blob relative to the ion gyroradius. Blobs with $R_b \gg \rho_i$ display an asymmetry that is most strongly conditioned by FLR effects on the K-H instability in the tail, while blobs with $R_b \sim \rho_i$ are affected more strongly by asymmetric deflection of the flow at the upstream edge. Simulations of hot blobs have also shown that the asymmetric poloidal deflection is dependent on the background flow speed. The scaling of the asymmetric effects is consistent with the increasing effect of the asymmetric term in Equation 3.9 at small scales, and the dependence of that term on background flow speed.

Since ion gyro-scale blobs in the edge plasma are not easily resolved by current tokamak diagnostics, they constitute a population of structures which is likely

to exist, but whose number and distribution are at present unknown. Further investigation of the effects of small blobs, in particular on energy dissipation within, and transport across, the edge plasma is hence desirable. We present results on this topic in Chapter 4. Hybrid simulations will also assist the comparison between theory and observation as structures on this scale become resolved by future diagnostic advances.

Chapter 4

Heating by Multi-species Ion Gyro-scale Blobs

4.1 Introduction

As discussed in Chapter 3, coherent, propagating filamentary plasma structures, which appear in cross-section as "blobs", are observed in the edge region of tokamaks [Boedo et al., 2003; Grulke et al., 2006; Myra et al., 2006; Nold et al., 2010; Kirk et al., 2006]. Their potential importance to the local physics is significant, notably their heating effect and their role in energy and particle transport in the edge plasma [Podestà et al., 2008; Angus et al., 2012], which is important for future experiments such as ITER [Kukushkin et al., 2003]. Blob diameters extend down to ion gyro-scales, and some mechanisms for blob-driven heating arise from ion kinetic effects on these scales (see Chapter 3 and Gingell et al. [2012]). It is therefore important to understand how these effects, in combination, depend on plasma parameters, flow speeds, and blob characteristics. In tokamak edge plasmas [Krasheninnikov, 2011], some blobs may be the poloidal projection of detached magnetic flux tubes, or ropes, that extend along the direction of the magnetic field. Polarising curvature drifts of ions and electrons give rise in the classic picture [Krasheninnikov, 2001] to $\mathbf{E} \times \mathbf{B}$ radial blob motion. Models for blob transport and evolution relevant to magnetic confinement fusion have focused on fluid, multi-fluid and gyro-averaged kinetic descriptions, approached both analytically and numerically [D'Ippolito et al., 2002; Aydemir, 2005; Russell et al., 2004; Garcia et al., 2005; Yu et al., 2006; Higgins et al., 2012; Park et al., 1999]. There have been successful simulations of blob creation via interchange-ballooning modes [Aydemir, 2005]. However, fully self consistent ion kinetic simulations have only recently begun to be applied to the problem of blob

evolution in tokamaks [Gingell et al., 2012]. We consider small blobs on a range of spatial scales, from below to above the ion Larmor radius. As in Chapter 3, the scale sizes that we consider are below that at which curvature driven interchange instability is known to be important [Yu and Krasheninnikov, 2003], and the fluid-like behaviour is dominated by the K-H instability [Krasheninnikov et al., 2008; D'Ippolito et al., 2011].

Filamentary structures are also of interest in astrophysical plasmas as a means for transporting magnetic flux, plasma momentum and energy. In boundary layers of Earth's magnetosphere, for example, this is observed to take place on ion kinetic scales [Nagano, 1979; Hasegawa et al., 2004; Sundkvist et al., 2005; Sundkvist and Bale, 2008] and has been the subject of kinetic simulations [Nykyri and Otto, 2001; Smets et al., 2007; Pritchett and Mozer, 2011]. Finite Larmor radius effects are observed to be important in relation to small scale astrophysical as discussed in Section 2.3.3. The generation of filaments and blobs on ion kinetic scales is thus ubiquitous in natural and laboratory plasmas. The importance of processes on ion kinetic scales in blobs in tokamak plasmas is thus an open question.

Acceleration of particles by kinetic processes is also an important question for astrophysics, which continues to invite research in recent years. In particular, ion kinetic processes have been shown to be significant to particle acceleration in collisionless shocks such as the Earth's bow shock [Burgess et al., 2012] and cosmic rays [Bell, 1978]. Heating of particles at collisionless shocks can occur when gyrating particles are reflected between shocks and these reformed upstream structures, and hence remain in the region of the shock for many gyro-periods [Su et al., 2012].

To address the physics of small blobs that may exist on scales comparable to the ion gyroradius, we use here a hybrid treatment which self consistently evolves the full ion kinetics without gyro-averaging. First results, [Gingell et al., 2012] and Chapter 3, have shown that the interaction of blob ions with the background flow proceeds in a fundamentally different manner for blobs on fluid scales and ion kinetic scales. This raises the question whether the rate of acceleration of ions originating within blobs also depends on blob size. The impact of the multiple ion species present in a burning fusion plasma on these kinetic scale blobs has also not hitherto been explored. The work in this Chapter addresses these questions with two related studies. First, we investigate the phenomenology of deuterium-tritium plasma blobs, some with an α-particle impurity, compared to proton plasma blobs. Second, we investigate the integrated effects of blob evolution on the plasma, rather than the evolution of individual blobs as discussed in Chapter 3 and [Gingell et al., 2012]. We conduct these studies using simulations which incorporate six-dimensional

phase space particle-in-cell ion kinetics and an electron fluid. Our hybrid approach captures the nonlinear interaction between ion gyration and plasma inhomogeneity; cross-scale coupling between ion gyro-scale kinetic modes and fluid MHD-like modes; and non-Gaussian ion velocity distributions. It incorporates multiple distinct ion populations in velocity and configuration space.

In this Chapter we present the results of fully self-consistent ion kinetic simulations of small scale (kinetic) structures, representing proton and deuterium-tritium blobs with radius R_B ranging from ρ_p to $10\rho_\mathrm{p}$, where the background proton gyro-radius $\rho_\mathrm{p} = \sqrt{2m_\mathrm{p}kT_\mathrm{p}}/eB_0$. We also simulate deuterium-tritium blobs with an alpha particle impurity. We find that for smaller blobs, with $R_B \sim \rho_\mathrm{p}$, blob ions are accelerated at a faster rate than their larger counterparts for which $R_B \gg \rho_\mathrm{p}$. The mechanism for this energisation of the ions is found to be a consequence of ion pick-up at the upstream edge of the blob, and of momentum transfer between internal vortices and the background flow. We establish how acceleration of blob ions scales with background flow speed, enabling the result to be generalised. The work presented in this Chapter has been published in [Gingell et al., 2013].

4.2 Simulations

The hybrid model we use here is that discussed in detail in Chapter 2. As in Chapter 3, ions are treated kinetically in full 6D phase space, and three-dimensional electromagnetic fields are evolved self-consistently on a 2D grid in space (x, y) and time. The 2D grid of 960 cells in x and y is chosen with cell size $\Delta x = 3.75\times10^{-3}\mathrm{m} = 0.4\rho_\mathrm{p}$. The box size is chosen to be sufficiently large to capture the full evolution of the moving plasma blob and is typically $450\rho_p = 320\rho_D = 250\rho_T$. The time step is determined by the CFL condition and is on the order of 10^5 time steps per ion gyro-period. We use sufficient particles per cell to fully represent the ion velocity distribution and a typical simulation employs 10^8 total computational particles, or roughly 100 particles per cell.

The simulations represent blobs as flux ropes with Gaussian spatial profiles of particle number density, with peak density five times the background n_0. Corresponding to the local density enhancement is a local depression magnetic field energy density, such that initially the system is in combined pressure equilibrium everywhere. The background plasma parameters are chosen to be approximately characteristic of edge conditions in a tokamak: $n_0 = 10^{19}\mathrm{m}^{-3}$, magnetic field $B_{z,0} = 0.4\mathrm{T}$, ion and electron temperature $T_0 = 4\times10^6\mathrm{K}$, and proton gyro-radius $\rho_\mathrm{p} = 8\times10^{-3}\mathrm{m}$. The background is initialised flowing transversely to the magnetic field at speed

$u_{\text{flow}} = 0.2v_A$ for all simulations, where v_A is the background proton plasma Alfvén speed. Both the simulation plane and the background flow speed are perpendicular to the background magnetic field. These background parameters are the same as those used in Chapter 3, and related parameters are given in Table 3.3. The initial particle distribution function is likewise the same as that for simulations presented in Chapter 3, given in Equation 3.1.

Here, the background flow, which is in the x-direction, represents a vector combination of the velocity imparted to the blob in an approximately radial direction during its creation and the smaller velocity of the poloidal background flow within the LCFS. The y-coordinate is perpendicular to the x-coordinate and to $\mathbf{B}$ in this coordinate system. The background flow speed, which is sub-Alfvénic ($u_{\text{flow}} = 0.2v_A$), is chosen with a view to achieving significant temporal evolution given the spatial resolution required and the computational resource available. Here, the simulations are carried out in the initial rest frame of the blob. Conversely in the rest frame of the background flow, the blob initially moves transversely to the magnetic field with velocity $-u_{\text{flow}}$.

Simulations are performed for proton plasma blobs with sizes R_B ranging from 1-10ρ_{p}, and also, for the first time, for 50:50 mix deuterium-tritium (D-T) plasma blobs of the same size. The evolution of blobs is shown for proton plasmas in Figure 4.1, for D-T plasmas in Figure 4.2, and for DTα plasmas in Figure 4.3. Large blobs for which $R_B \gg \rho_{\text{p}}$, as in the upper sections of Figures 4.1, 4.2 and 4.3, are advected with the background flow and develop internal, anti-symmetric vortices as observed in [Katz et al., 2008]. Kelvin-Helmholtz instability develops on the lower edge of these larger blobs, creating corrugated structures at late times, visible at $16t_{\Omega_{\text{p}}}$ for the proton blob of radius $6\rho_{\text{p}}$. This instability grows more quickly on the lower edge than the upper edge as a result of finite Larmor radius symmetry breaking [Nagano, 1979; Gingell et al., 2012]. Smaller blobs, for which $R_B \sim \rho_{\text{p}}$ so that kinetic effects are more important, develop stronger asymmetries in y, and are deflected in the $-y$ direction as a result of ion pick-up as in [Chapman and Dunlop, 1986]. These effects are also described in Chapter 3. Small blobs also display a reduced lifetime, breaking up on shorter timescales.

We note that for multi-species blobs, differences that arise between populations within a single with different ion gyro-radii are significant. In that case of D-T plasma blobs, for example, regions within the blob may contain up to twice as many deuterons as tritons, and vice versa. This is demonstrated directly in Figure 4.4, which shows the difference in number density of deuteron and triton populations in plasma blobs of radius 10 and $2\rho_p$. The figures show that differences are both larger

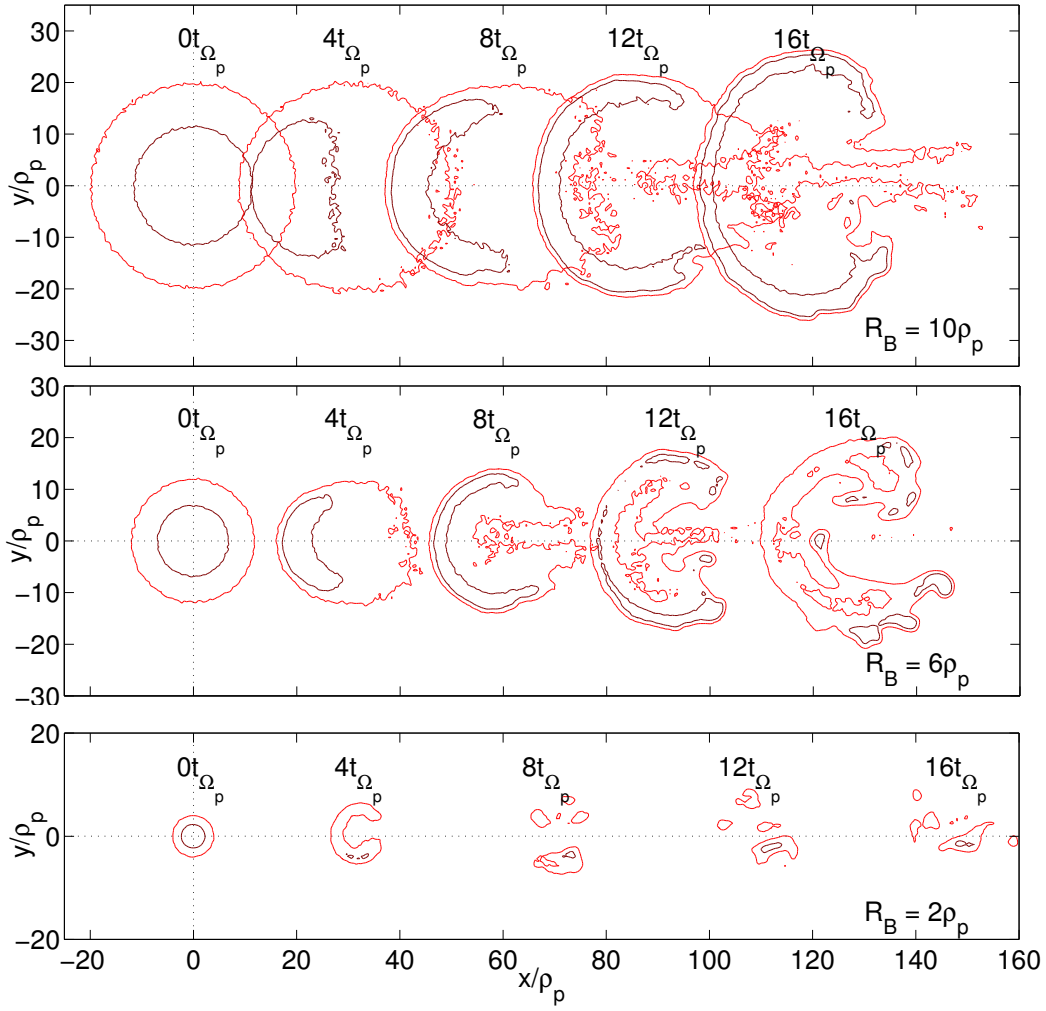

Figure 4.1: Number density contours for proton plasma blobs with radii 10, 6 and 2 ρ_{p} (top to bottom). Contours are displayed for number densities of $1.5n_0$ (light) and $3n_0$ (dark) at regular $4t_{\Omega_{\mathrm{p}}}$ time intervals. Dotted lines mark the initial position of the blobs. These contours display the evolution of the blobs, including advection with the background flow, generation of Kelvin-Helmholtz instability on the lower edge, deflection of blobs in the $-y$ direction, and the shorter lifetime of smaller blobs.

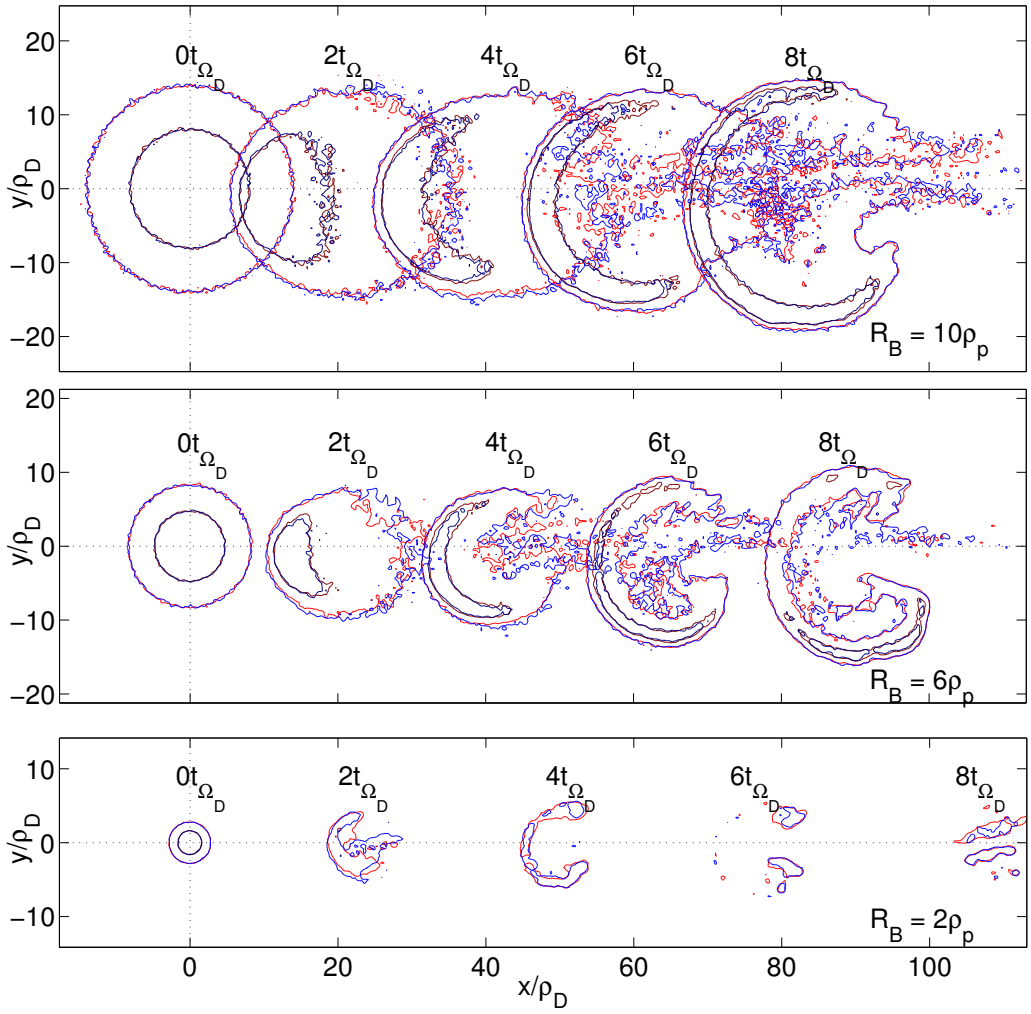

Figure 4.2: Number density contours for D-T plasma blobs with radii 10, 6 and 2 ρ_{p} (top to bottom). Contours are displayed for number densities of $1.5n_0$ (light) and $3n_0$ (dark) at regular $2t_{\Omega_{\mathrm{D}}}$ time intervals. Contours are given for both deuteron (red) and triton (blue) populations. Dotted lines mark the initial position of the blobs. These contours display the evolution of the blobs, including advection with the background flow, generation of Kelvin-Helmholtz instability on the lower edge, deflection of blobs in the $-y$ direction, and the shorter lifetime of smaller blobs.

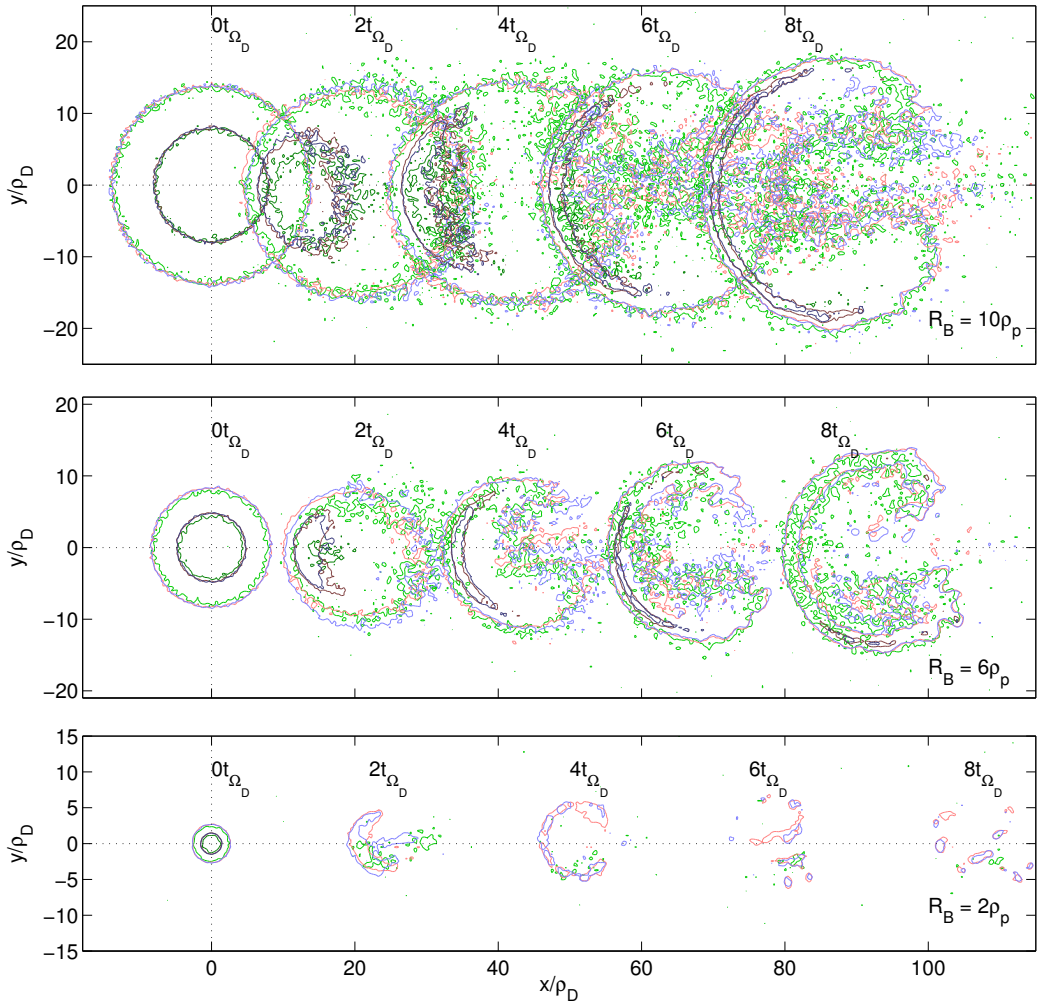

Figure 4.3: Number density contours for D-T plasma blobs with a 10% α particle impurity, with radii 10, 6 and 2 ρ_{p} (top to bottom). Contours are displayed for number densities of $1.5n_0$ (light) and $3n_0$ (dark) at regular $2t_{\Omega_{\mathrm{D}}}$ time intervals for each species. Contours are given for deuteron (red), triton (blue) and alpha particle (green) populations. Dotted lines mark the initial position of the blobs. These contours display the evolution of the blobs, including advection with the background flow, generation of Kelvin-Helmholtz instability on the lower edge, deflection of blobs in the $-y$ direction, and the shorter lifetime of smaller blobs.

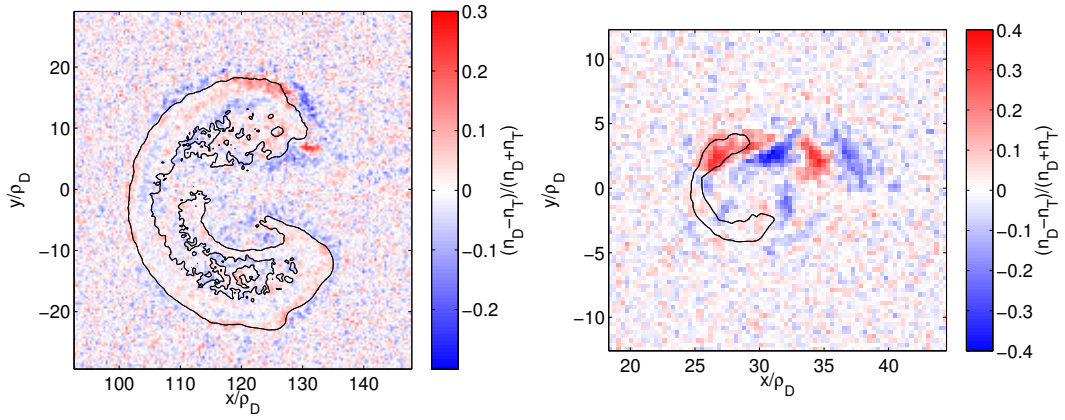

Figure 4.4: Difference between the number densities of deuterium and tritium populations normalised to total number density for D-T blobs of radius $10\rho_p$ (left) and $2\rho_p$ (right). Regions coloured in red are those which contain more deuterons than tritons, those coloured blue contain more tritons than deuterons. A black contour is drawn for deuteron number density at 1.5 times the background. Alternating enhancements in deuteron and triton number density downstream of the blob of radius $2\rho_p$ are created by shedding of Kelvin-Helmholtz vortices from the upper edge.

in size and of greater magnitude in blobs of smaller radii. Additionally, a further asymmetry is revealed: differences appear more on the upper edge of the blobs than on the lower edge. We also see a difference between ion populations in secondary evolutionary features, such as the trajectories of the centres of mass of each population. As in Chapter 3, we find that smaller blobs are deflected in the $-y$ direction more than larger blobs. However, we also find that populations with different gyro-radii are deflected by different amounts. The deflection is demonstrated for a small blob in Figure 4.5, which shows the trajectories of deuteron, triton and alpha-particle populations within a DTα blob of radius $2\rho_D$. In this case, the deuteron population is deflected more than the others. That these differences between populations arise further vindicates our use of a hybrid approach which incorporates ion kinetics to simulate these objects.

4.3 Ion Energisation

Let us focus on how acceleration of ions varies with blob size. From Poynting's theorem, we can obtain from the simulations the rate at which any subset of ions gains energy by calculating $\mathbf{J}_\alpha \cdot \mathbf{E}$, where $\mathbf{J}_\alpha$ is the current carried by that subset of ions. Hence we can calculate the cumulative energy transfer from the electromag-

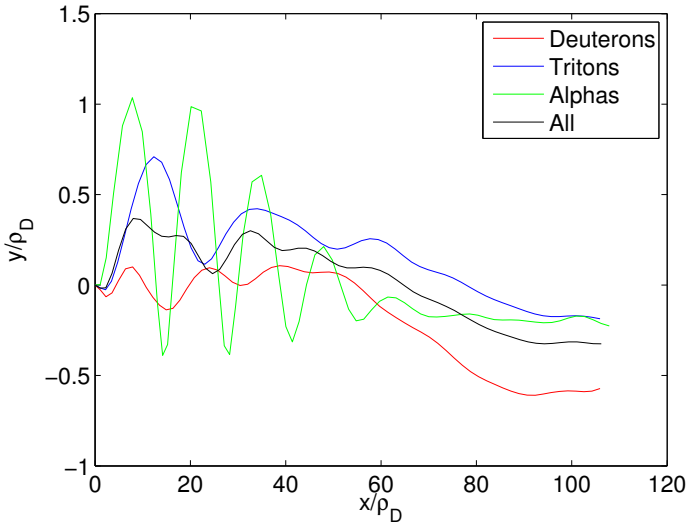

Figure 4.5: Trajectories of the centres of mass for deuteron, triton and alpha-particle populations in a blob of radius $2\rho_p$ over a period of $8t_{\Omega_D}$. After the initial period in which coherent particle gyration is dominant, up to about $4t_{\Omega_D}$, the population of deuterons is seen is deflect in the $-y$ direction more than the triton and alpha-particle populations. We note that the deflection of each species is not simply proportional to the mass or gyro-radius of each species.

netic fields to the blob ions as a function of time, by integrating over the simulation domain and time:

$$h(t) = \frac{1}{N_{\mathrm{B}}} \int_0^t \int \int_D \mathbf{J}_{\mathrm{B}} \cdot \mathbf{E} \, \mathrm{dxdy} \, \mathrm{dt}, \tag{4.1}$$

where N_{B} is the total number of particles originating in the blob, D is the full simulation domain, and $\mathbf{J}_{\mathrm{B}}$ is the current density for the blob ions. This energisation per blob ion $h(t)$ is plotted in Figure 4.6 for proton plasma blobs of varying radii. All the curves show net a energy increase, with $h(t)$ increasing with t, and small oscillations at the gyro-period. Importantly, there is a clear trend in the rate at which ions gain energy, which increases as blob size decreases. There is also a trend in the time at which significant energisation starts. At middle times, the two high density regions of the blob formed in the upper and lower vortices interact at the downstream side, leading to a temporary plateau or reduction in energy as blob ions in that region lose momentum. This period of evolution is displayed in figure 4.7.

Figure 4.8 examines this energy increase for 50:50 mix D-T plasma blobs, relevant to burning fusion plasmas. There are now two populations of singly charged blob ions with different gyro-radii. We gain insight into the underlying process by

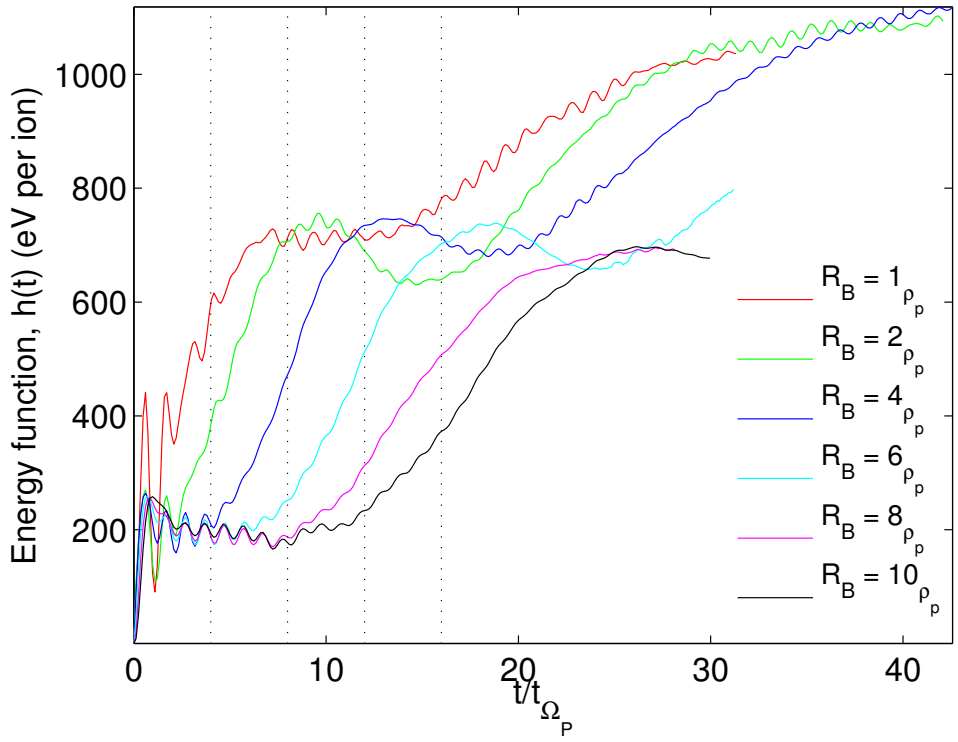

Figure 4.6: Energy transfer to blob ions plotted for proton plasma blobs of varying radii, calculated by integration of $\mathbf{E} \cdot \mathbf{J}$ for blob ions in space and time. Dotted lines mark times at which number density contours are plotted in Figure 4.1. The more rapid heating displayed for smaller blobs implies a greater ability of smaller blobs to heat the plasma.

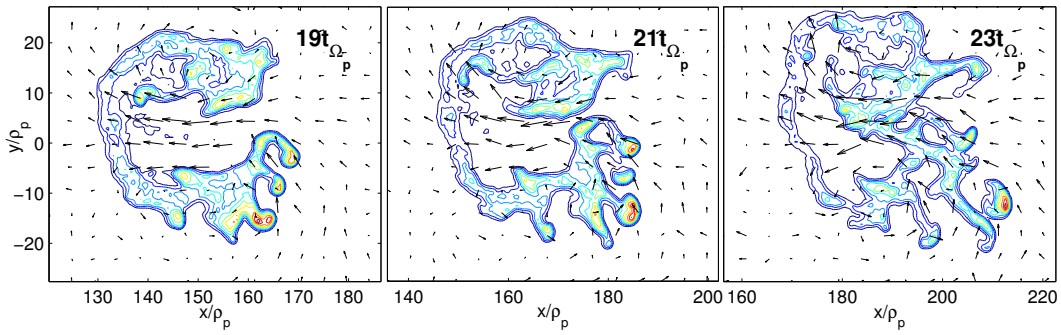

Figure 4.7: Evolution of a proton plasma blob of initial radius $6\rho_{\mathrm{p}}$ during the time interval (see Figure 4.6) associated with the reducing in the mean energy of blob ions. Number density contours are displayed with arrows representing the velocity field in the background flow frame. The colour scale indicates contour sequence from low (blue) to high (red). The interaction between the two coalescing high density regions at the downstream edge leads to disruption of the blob's vortex structure and loss of momentum of blob ions in that region.

normalising the energy function per ion, $h(t)$, to particle mass m_D and m_T for their respective species. This normalised energy function is plotted in the main panel of Figure 4.8 for D-T plasma blobs of radius ρ_{p} and $10\rho_{\mathrm{p}}$, with the energy function $h(t)$ inset. As in the proton plasma case, the ions in smaller D-T blobs are heated faster, however the energy increase for the tritium population is larger than for deuterium in the same blob. Remarkably, once normalised, we find close correspondence between the D and T populations — the only variation is in small oscillations on their respective gyro-periods. Therefore the energy increase scales with a factor common to both deuteron and triton populations.

Further insight into the effect of this energisation process can be gained by examining the spatial dependence of the temperature and $\mathbf{J}_i \cdot \mathbf{E}$ fields. The temperature and $\mathbf{J}_i \cdot \mathbf{E}$ fields are shown for proton plasma blobs of radii $R_b = 2\rho_p$ and $R_b = 10\rho_i$ in Figure 4.9. We note several important features of these figures. First, variation in the local temperature is observed at the boundaries between blob plasma and background flow plasma, and in the tail of ejecta on the downstream side. These regions are characterised by high levels of mixing between the blob and background populations, suggesting that the interaction of these populations can result in a highly localised temperature change. However, as shown in Figure 4.10, we see no net temperature increase when considering the mean temperature over each grid cell containing blob ions. The spatial dependence of the $\mathbf{J}_i \cdot \mathbf{E}$ fields demonstrates

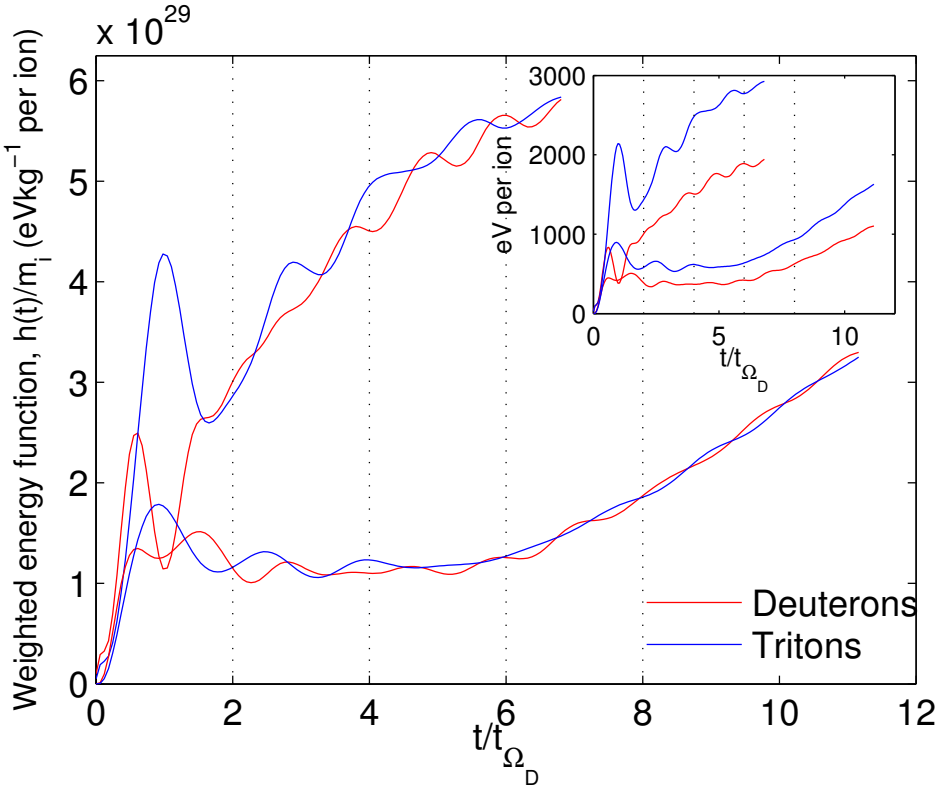

Figure 4.8: Energy transfer to blob ions in 50:50 mixed D-T plasma blobs of radius $1\rho_{\mathrm{p}}$ (upper curves) and $10\rho_{\mathrm{p}}$ (lower curves), normalised by particle mass; and inset with the energy transfer per ion as given in Figure 4.6. Dotted lines mark times at which number density contours are plotted in Figure 4.2. The correspondence between mass-normalised energy curves for deuteron and triton species demonstrates that the energy increase scales with a factor common to both species.

that the $\mathbf{J}_i \cdot \mathbf{E}$ energy increase seen in Figures 4.6 and 4.8 occurs preferentially at the upstream edge of the blob. Importantly, the $\mathbf{J}_i \cdot \mathbf{E}$ field is not strongly spatially correlated with the temperature for each blob. Hence, we can conclude that the measured energy increase manifests principally as fluid acceleration on scales on the order of the blob radius, rather than an increase in the velocity of isolated populations on scales smaller than a grid cell, for which we would observe a corresponding, localised increase in velocity dispersion (temperature).

4.4 Momentum Transfer

To investigate the mechanism for the observed increase in ion energies, we plot individual ion trajectories in Figure 4.11. For blobs of radius $R_B \gg \rho_\mathrm{p}$, the dynamics is fluid-like and heating can occur by momentum transfer around perturbations at the shear boundary between stationary blob plasma and flowing background plasma. For these larger blobs, a vortex pair forms, which would be antisymmetric in the fluid limit where ρ_p is not resolved. Here, however, finite Larmor radius symmetry breaking causes the lower vortex to expand to a larger size than the upper vortex. The Kelvin-Helmholtz instability, which develops from perturbations on the shear boundary of these vortices, grows faster on the lower edge. These asymmetric vortex cells can be seen in the ion trajectories, as in the left of Figure 4.11, which displays trajectories for particles initialised in the blob and background populations. Background ions deflect around the blob at the upstream edge, with a stagnation point along the line of symmetry, and blob ions follow the streamlines of internal vortices.

For blobs of radius $R_\mathrm{B} \sim \rho_\mathrm{p}$, Figure 4.11 shows that the primary mechanism of momentum transfer is ion pick-up at the upstream edge of the blobs. Particles initially within the stationary blob, which subsequently enter the spatial region dominated by the background flow, are accelerated in the $+y$ direction by the motional electric field in that region. Ultimately such particles are picked-up by the background flow, as discussed in Section 3.4.2.1, and execute a cycloidal trajectory in the direction of the $\mathbf{E} \times \mathbf{B}$, background flow, with relatively large gyro-radius $u_\mathrm{flow}/\Omega_\mathrm{i}$ and thermal velocity u_flow. The momentum transfer which occurs between blob and background ions as a result of this mechanism can be seen by writing the

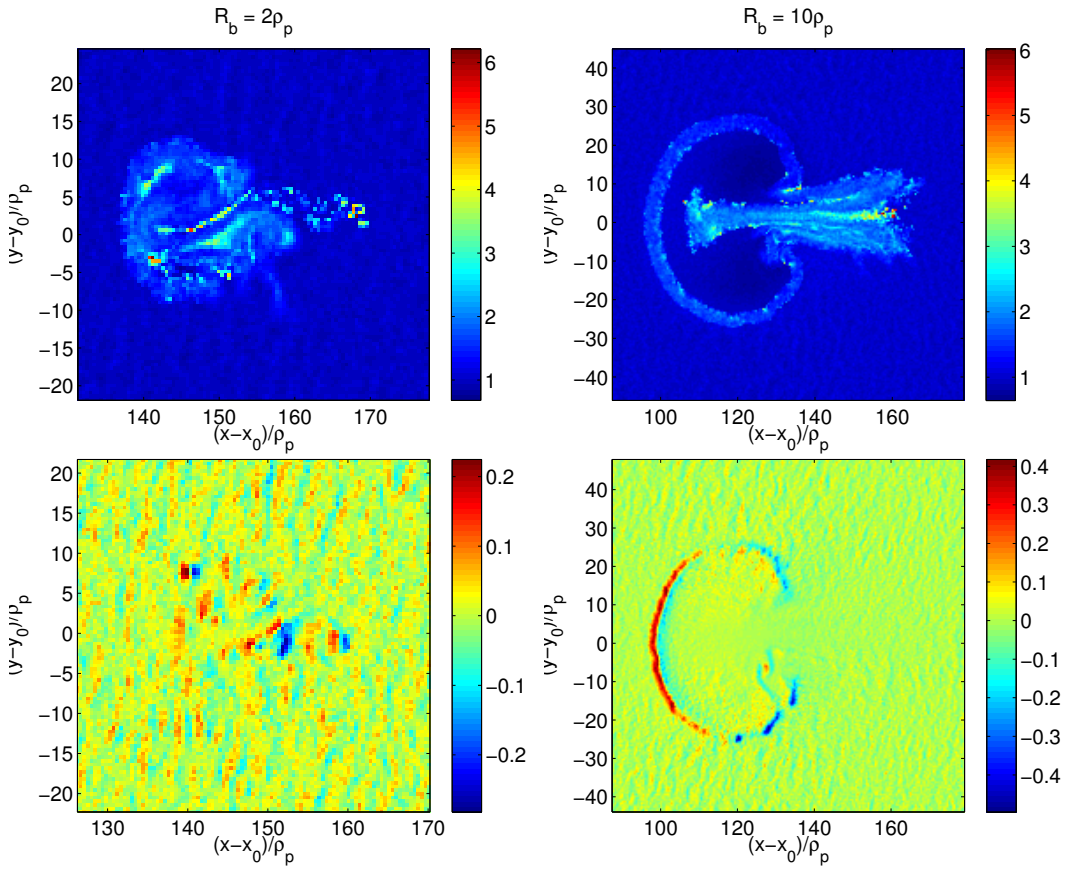

Figure 4.9: Top: Spatial dependence of the temperature for blobs of radius $2\rho_p$ (left) and $10\rho_p$ (right) at time $t = 16t_\Omega$. Temperature is given in colour for each grid cell in units of the background temperature $T_0 = 4 \times 10^6 K$. Here we note an increase in temperature in the region surrounding the blob and in the tail, where significant mixing of the blob and flow populations occurs, and a small decrease in the centre of the larger blob due to expansion of the blob plasma. Bottom: Spatial dependence of $\mathbf{J}_i \cdot \mathbf{E}$ for the same blobs at time $t = 16t_\Omega$, in units of the background $E_0 J_0$. These figures demonstrate that particle energisation is occurring largely on the upstream, leading edge of the blobs. This spatial dependence does not strongly correlate with the spatial dependence of the temperature.

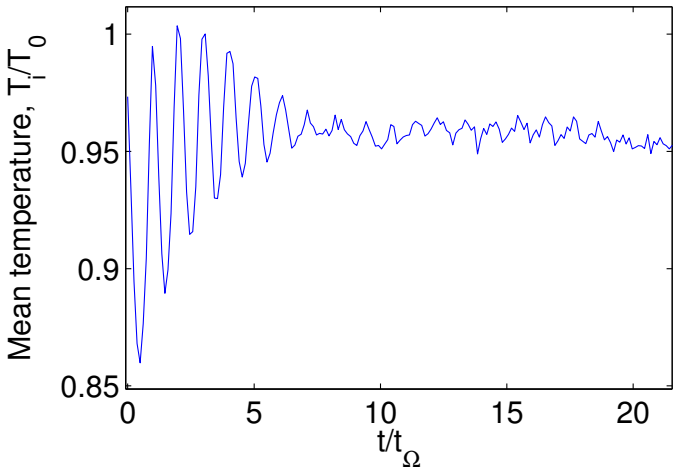

Figure 4.10: Time dependence of the temperature in grid cells containing ions initialised within the blob, for a blob of radius $R_b = 10\rho_p$. Here, the mean temperature $T_i = \Sigma_j T_j/N$ where T_j is the temperature in grid cell j and N is the total number of grid cells containing blob ions. We see no trend in the mean cell temperature during the period of particle acceleration seen in Figure 4.6

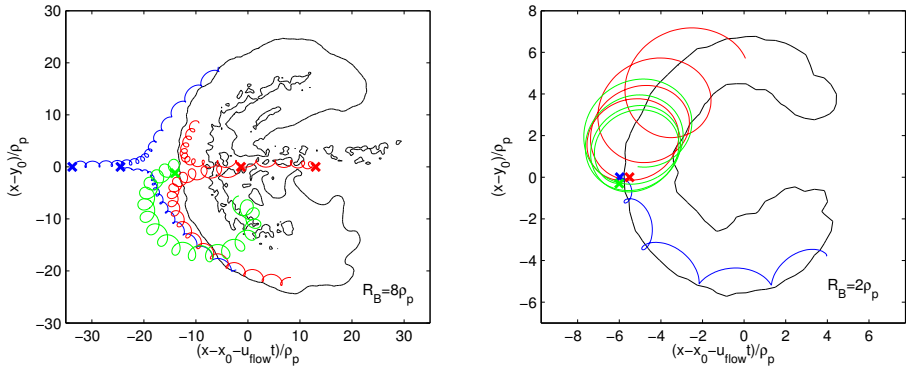

Figure 4.11: Ion trajectories plotted in the frame of reference of the blob, for blobs of initial radius $8\rho_\mathrm{p}$ (left) and $2\rho_\mathrm{p}$ (right). Initial positions of the ions are marked with an 'x'. For the larger blob, ions originating in both the blob (red) and the flow (blue) trace the streamlines of antisymmetric vortex cells formed on the upper and lower halves of the blob. For the smaller blob, an ion originating in the blob (red) is shown to pick-up in the flow and deflect in the $+y$ direction with relatively large gyro-radius, while an ion originating in the flow (blue) is deflected in the $-y$ direction with thermal gyro-radius. An additional blob ion is shown with a green trajectory in both cases, originating below the line of symmetry in the y-direction. This (green) ion is deflected in the $+y$ direction in the small blob, and the $-y$ direction in the large blob.

ion momentum equation for a species α [Chapman and Dunlop, 1986]:

$$m_\alpha n_\alpha \frac{\mathrm{D}\mathbf{v}_\alpha}{\mathrm{Dt}} = e n_\alpha u_{\mathrm{flow}} \left(\frac{\mathbf{v}_\alpha}{u_{\mathrm{flow}}} - \frac{1}{n} \sum_{\alpha'} n_{\alpha'} \frac{\mathbf{v}_{\alpha'}}{u_{\mathrm{flow}}} \right) \times \mathbf{B} + \frac{n_\alpha}{n} \left(\mathbf{J} \times \mathbf{B} - \nabla \cdot \vec{\mathbf{P}}_{\mathrm{e}} \right), \tag{4.2}$$

where $\mathbf{v}_\alpha$ represents the fluid velocity field for species α, and total number density $n = \sum_{\alpha'} n_{\alpha'}$. The first term on the RHS represents a symmetry breaking discussed in Section 3.4.2.1, present only in spatially inhomogeneous regions in which there is a difference between the mean velocities of blob and background ion populations. This symmetry breaking term depends on particle velocity, displayed here as a fraction of the background fluid velocity $\mathbf{v}_\alpha / u_{\mathrm{flow}}$. Hence momentum gain resulting from this term scales with relative particle velocities and therefore background flow speed, but not with particle mass, as manifest in Figure 4.8. The symmetry breaking term tends to zero as $\mathbf{v}_{\alpha'} \to \mathbf{v}_\alpha$, which is the fluid limit.

This mechanism [Gingell et al., 2012] is a major contributor to finite Larmor radius symmetry breaking in the blobs. It can be seen in the individual ion trajectories in Figure 4.11, which displays the $-y$ deflection of a typical background flow ion with thermal gyro-radius ρ_{p}, and the $+y$ deflection of a blob ion displaying pick-up with a much larger gyro-radius. For blobs of radius $R_B \sim \rho_p$, the $+y$ deflection is seen even for blob ions originating below the line of symmetry.

4.5 Conclusions

Ion gyro-scale blobs, as simulated here, are not easily resolved by current tokamak diagnostics. They constitute a population of structures which is likely to exist, but whose number and distribution are unknown. Our simulations show that the rate at which fields do work on the ions in the blob, dh/dt, is faster for smaller, un-resolvable blobs. The principal mechanisms behind the increase in ion energies have been inferred from normalised results for D-T plasma blobs: in the kinetic case $R_{\mathrm{B}} \sim \rho_{\mathrm{p}}$, pick-up ions are accelerated on the upstream edge of the blob, and in the fluid case $R_{\mathrm{B}} \gg \rho_{\mathrm{p}}$, momentum transfer occurs at the shear boundary between the blob and background plasmas. The total increase in ion energy caused by blobs during their dwell time in the plasma τ is thus $\tau\,\mathrm{dh/dt}$ which implies, for a dwell time independent of blob size, that smaller, ion gyro-scale blobs energise the plasma more than larger ones. These results indicate that the full ion kinetics of an observationally un-resolvable population of small blobs may be important in

determining energy flow through and within the edge plasma in fusion experiments.

Chapter 5

Creation of Ion Gyro-scale Blobs by Kinetic Interchange and Kelvin-Helmholtz Instabilities

5.1 Introduction

As discussed in Section 1.3.2, coherent, propagating filamentary structures, which appear in cross section as blobs, are observed in the edge region of tokamaks [Boedo et al., 2001; Grulke et al., 2006; Myra et al., 2006; Nold et al., 2010; Kirk et al., 2006]. Their role in particle and energy transport is significant, and blobs may result in as much as 50% of the particle transport across the scrape-off layer towards the vessel wall [Boedo et al., 2001]. Hence, a more complete understanding of the physics associated with blob transport and evolution is critical for future experiments such as ITER [Kukushkin et al., 2003].

Turbulence in the near-edge, confined region arises as a result of the drift wave and interchange instabilities present in the outboard side of the torus. Fluctuations of density, electron temperature and potential have been observed with amplitude 5-100% of the background, with smaller fluctuations in the magnetic field [Zweben et al., 2007]. The power spectrum for these fluctuations has been observed to be flat up to 10-100Hz, with a power-law exponent in the region of 1-4 for shorter time scales [Pedrosa et al., 1999]. The charge polarisation of these turbulent fluctuations, and subsequent radial transport, forms the classical model of blob creation and propagation in the near-edge region of tokamaks. Observations

and mechanisms of blob creation are discussed in Chapter 1, Section 1.3.2.4.

In Chapter 3 and Chapter 4 we have demonstrated, first, that ion gyro-scale blobs develop significant asymmetries in their evolution compared with larger scale, fluid blobs and, second, that these ion gyro-scale blobs can accelerate ions at a faster rate than their larger counterparts. In order to properly assess the impact of gyro-scale blobs to a tokamak plasma and make comparisons with those at fluid scales, we require a knowledge of the statistics of blob creation on ion gyro-scales. Since observations on these scales using contemporary diagnostics are difficult, we explore this regime using a hybrid code comprising kinetic ions and fluid electrons.

In this Chapter, we simulate blob creation on the ion gyro-scale using the hybrid code presented in Chapter 2. Interchange instabilities, as noted in the literature detailed in Section 1.3.2.4, have been presented as the most common mechanism for creating blobs. The appearance of shear boundaries in the edge region [Smolyakov et al., 2000] can lead to the generation of a Kelvin-Helmholtz instability, which may also serve as a mechanism for structure formation. These instabilities are the basis of this study, and inform our choice of initial and boundary conditions. The initial and boundary conditions chosen represent, in the first case, shear boundaries in the near-edge, confined region in the absence of a density gradient, for which the Kelvin-Helmholtz instability is the principal source of structure formation. In the second case, we present simulations which include a density gradient, in the absence of shear, for which the interchange instability dominates. Finally, in the third case, we present simulations which include both a shear boundary and a density gradient. The statistics of blob creation and particle displacement are discussed in each case.

5.2 Simulation Geometry

The hybrid code used in this chapter is that used for the rest of the work in this Thesis, which self-consistently evolves three-dimensional **E**, **B** and **J** vector fields on a 2D grid in space (x, y) and time, and evolves the full ion kinetics in the six-dimensional phase space. The $\pm x$ boundaries are periodic, and the y boundaries are open with a particle source at background conditions defined below.

Background parameters are chosen to be representative of conditions towards the edge of a tokamak, as in Chapters 3 and 4. These background parameters are as follows: $n_0 = 10^{19}\mathrm{m}^{-3}$, $T_i = T_e = 4 \times 10^6\mathrm{K}$, $B_0 = 0.4\mathrm{T}$. Derived parameters are given in Table 3.3. Several initial conditions are discussed in this Chapter, which lead to the growth of the interchange or Kelvin-Helmholtz instabilities separately and in combination for both proton plasmas and, for cases more relevant to burning

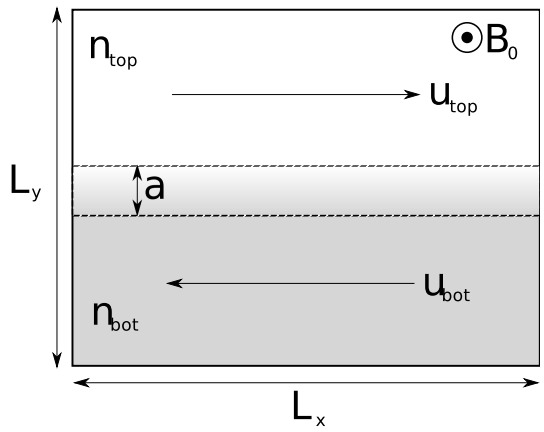

Figure 5.1: Initial conditions and geometry for the simulations presented in this Chapter.

plasmas, a 50/50 deuterium-tritium mix. For the simulations for which we study the evolution of the Kelvin-Helmholtz instability alone, the plasma is initially homogeneous in density, temperature and magnetic field strength, with a velocity shear boundary set up along $y = 0$ with $u_{\rm top} = 0.1v_A$ and $u_{\rm bot} = -0.1v_A$, as displayed in Figure 5.1. For the simulations for which we study the interchange instability, the background temperature and magnetic field are uniform, with densities $n_{\rm top} = n_0$ and $n_{\rm bot} = 4n_0$, thereby initialising the simulation with a pressure gradient to drive the instability. For those simulations for which we intend to study the combination of interchange and Kelvin-Helmholtz instabilities, both the shear boundary and pressure gradient are present. For the simulations presented in this Chapter, the initial boundary width a is equal to the cell size Δx. The background magnetic field $\mathbf{B}_0$ is initialised perpendicular to both the plane of the simulation and the background flows. A diagram of this geometry is given in Figure 5.1. From the chosen initial conditions, the initial distribution function of particles in the simulations is given by:

$$f_0(y, \mathbf{u}) \propto \left(\frac{1}{2}(n_{\rm bot} - n_{\rm top})\left[1 - \tanh\left(\frac{y}{a}\right)\right] + n_{\rm top}\right) \exp\left(-\frac{(\mathbf{u} - \mathbf{u}_{\rm bulk}(y))^2}{2u_{\rm th}}\right), \tag{5.1}$$

where $u_{\rm th}$ is the thermal velocity, and the local bulk velocity is given by $\mathbf{u}_{\rm bulk} = (u_x(y), 0)$ with

$$u_x(y) = \left(\frac{1}{2}(u_{\rm top} - n_{\rm bot})\left[1 + \tanh\left(\frac{y}{a}\right)\right] + u_{\rm bot}\right). \tag{5.2}$$

5.3 Results

The results presented here will focus on three aspects of the evolution in the presence of the K-H, the interchange and both instabilities. First, we will examine the morphology of the instabilities. Second, we will discuss the creation of coherent structures by these instabilities in terms of both the distribution of structure sizes and packing fractions. Finally, we will discuss the statistics of particle displacement perpendicular to the boundaries.

5.3.1 Morphology

The first simulations we will discuss are those which employ only a shear boundary at $y = 0$, which are subject to a growing Kelvin-Helmholtz instability. This geometry has been studied for both proton plasmas, as shown in Figures 5.2 and 5.3, and for deuterium-tritium plasmas, as shown in Figure 5.4. In both cases, we observe the characteristic vortex roll-up of the Kelvin-Helmholtz instability, with a growth rate proportional to the scale size. The growth of the instability continues until the vortices approach the size of the simulation domain at late times.

Although the Kelvin-Helmholtz instability can produce coherent structures at the boundary layer, these structures appear to be limited to vortices which coalesce over time. Additionally, as shown by plots of total number density in Figure 5.3, the vortices eject particles to form low-density holes. Neither the regions of weak over-density at the edges of the vortices, nor the holes which form within the vortices, are seen to propagate in the y-direction and are unable to separate from the boundary layer. Hence, the growth of the ion kinetic Kelvin-Helmholtz instability cannot, by itself, lead to the formation of propagating blobs in a proton plasma.

To determine whether the coupling between two populations with different gyro-radii can lead to structure formation which is not seen in the proton plasma simulation, we now examine simulations of a 50-50 mix deuterium-tritium plasma with a shear boundary. All background parameters, including shear velocity, are identical to the proton plasma case. The evolution of the number density in this case is given for particles initialised below the shear boundary in Figure 5.4. This scenario results in a reduced growth rate and a larger fastest growing mode than the proton plasma case. Again, we do not see structures that separate from the shear boundary. However, by examining the difference between the number densities of deuteron and triton populations, as given in Figure 5.5, we find that finite Larmor radius effects can effect the evolution of each population. In this case, more deuterons are found in the vortex centres than tritons, and more tritons are found towards the vortex

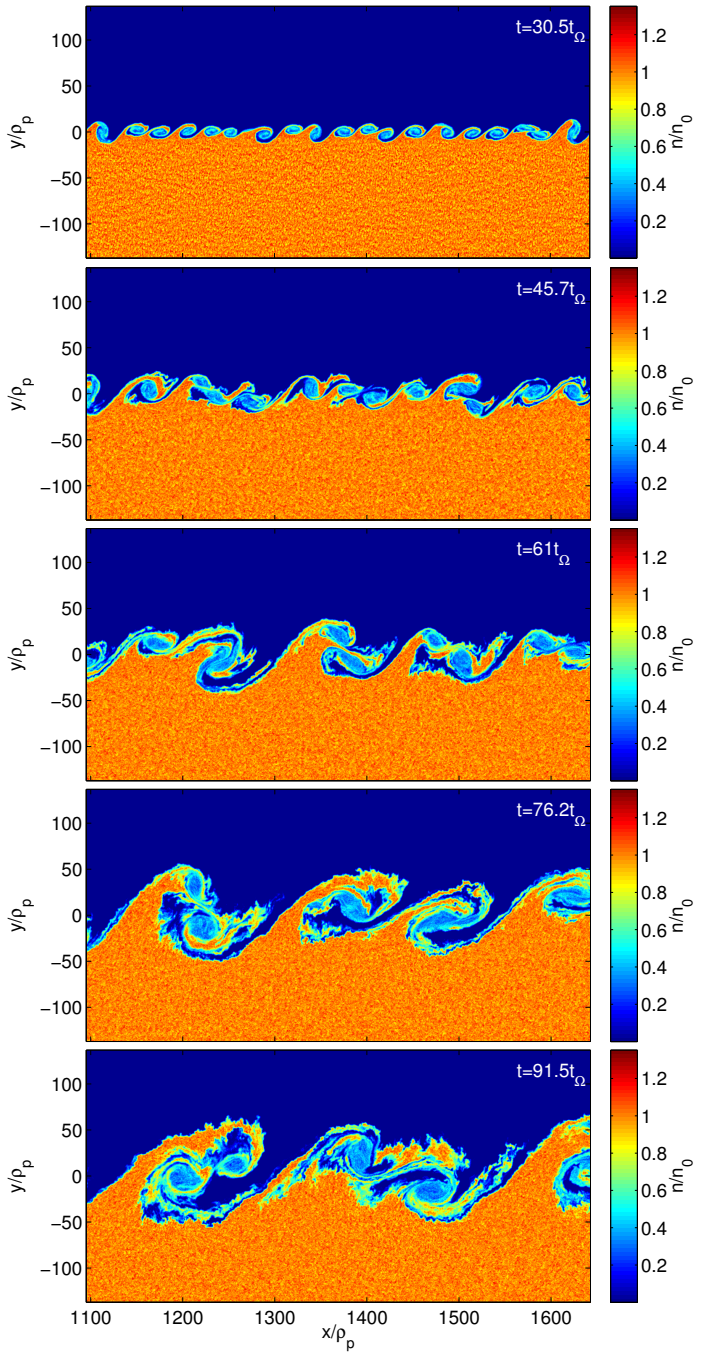

Figure 5.2: Number density of ions initialised below the shear boundary $y = 0$ for a proton plasma with flow $u_{\text{top/bot}} = \pm 0.1 v_A$ and shear boundary width $a = \Delta x$. The roll-up of vortices causes by the Kelvin-Helmholtz instability is visible from $t \approx 30 t_\Omega$. These vortices coalesce into larger structures over time consistent with the growth rate of the K-H instability.

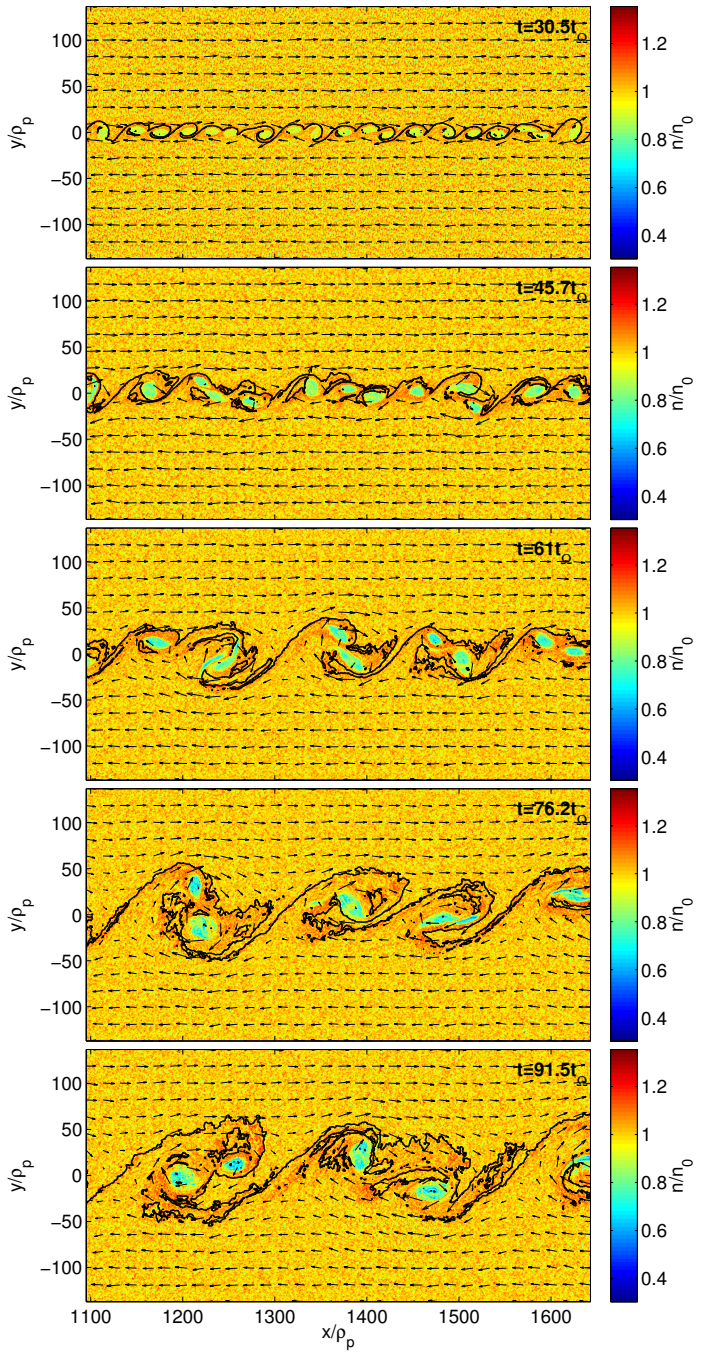

Figure 5.3: Total number density of ions for a proton plasma with initial flow $u_{\text{top/bot}} = \pm 0.1 v_A$ and shear boundary width $a = \Delta y$, as in Figure 5.2. A black line marks the boundary between plasma originating on opposite sides of the shear boundary at $t = 0$, and black arrows represent the velocity field. Note here that although propagating, high-density regions do not form due to the K-H instability, coherent, low-density holes form inside the vortices and grow larger with time.

edges.

The above suggests that the ion kinetic Kelvin-Helmholtz instability cannot act as the sole mechanism for the creation of blobs in a uniformly dense plasma. We now examine the effect of a density gradient and the associated interchange instability. The number density of a simulation of a proton plasma with $n_{\text{top}} = n_0$, $n_{\text{bot}} = 4n_0$ and $u_{\text{top/bot}} = 0$ is shown in Figure 5.6. In this scenario, we observe separation of populations of ions from their initial populations, i.e. blobs of high density plasma in the $y > 0$ region dominated by low density plasma, and holes of low density plasma in the $y < 0$ region. Additionally, these structures are seen to propagate in the y direction by virtue of the velocity imparted to these populations by the interchange instability. This propagation does not require a charge separation electric field across the blob plasma, which occurs in regions with open magnetic field lines. Hence, we can conclude that the interchange instability can lead to the formation of radially propagating blobs within the region of closed field lines.

We now examine the most realistic case, where both interchange and K-H instabilities are active. We now include in our initial and boundary conditions both a pressure gradient and a shear boundary at $y = 0$. For these simulations, $n_{\text{top}} = n_0$, $n_{\text{bot}} = 4n_0$ and $u_{\text{top/bot}} = \pm 0.02 v_A$. The evolution of the number density for these simulations is shown for a proton plasma in Figure 5.7 and for a D-T plasma in Figure 5.8. In both cases, separation of blobs occurs at the crests of vortices generated by the K-H instability, and at earlier times relative those simulations with zero shear, which are dominated by the interchange instability. The differences between the distribution of blob sizes created by the K-H and interchange instabilities in each of our three scenarios, and for proton and D-T plasmas, will be discussed in the following section.

5.3.2 Structure Statistics

The distribution of blob sizes in the core-edge and SOL regions of tokamaks is not well known, particularly for scale sizes on the order of or less than the ion gyro-radius. Since blobs play a significant role in particle and energy transport across the separatrix, and can damage components on the chamber wall, it is important to understand how significant kinetic effects are to the population as a whole, in addition to the individual blob level as discussed in Chapters 3 and 4. Hence, we now determine the distribution of blob sizes which develop as a result of our chosen mechanism, in this case the interchange and Kelvin-Helmholtz instabilities.

To recover structure size statistics from our simulations, we define a threshold condition to distinguish structures from the background, with a corresponding

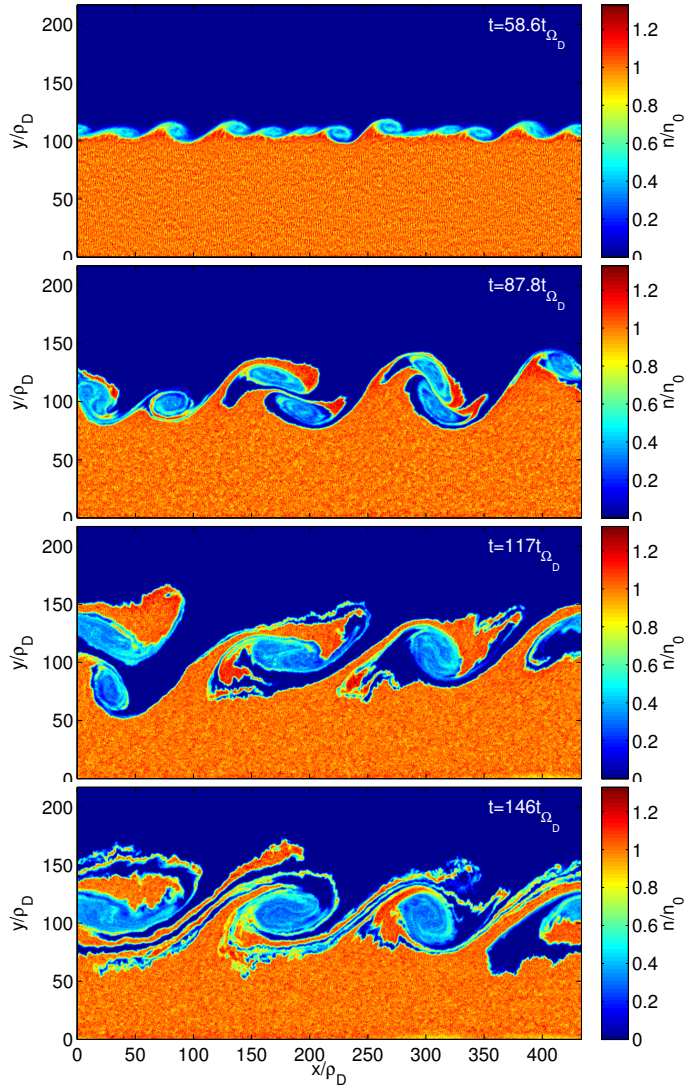

Figure 5.4: Number density of deuterons and tritons initialised below the shear boundary $y = 0$, with flow $u_{\text{top/bot}} = \pm 0.1 v_A$ and shear boundary width $a = \Delta x$. Evolution proceeds in much the same way as for proton plasmas, including vortex roll-up and growth rate $\Gamma \propto k$. However, we note both a decrease in growth rate for any given scale size, and a larger fastest growing mode.

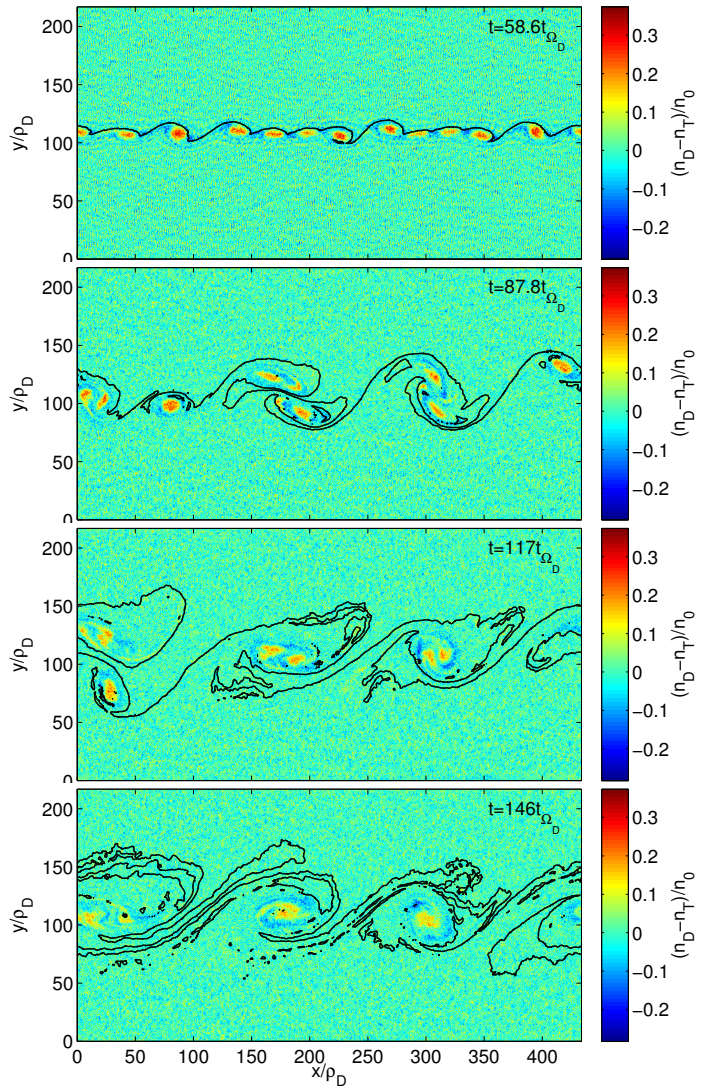

Figure 5.5: Difference in the number density between deuteron and triton populations across the whole simulation domain for the simulation displayed in Figure 5.4. The black line represents the boundary between plasma initialised above and below the shear boundary. Red represents a surplus of deuterons, and blue a surplus of tritons. Note that there is a surplus of deuterons inside the vortices which form as a result of the K-H instability, and a surplus of tritons on the outer edge.

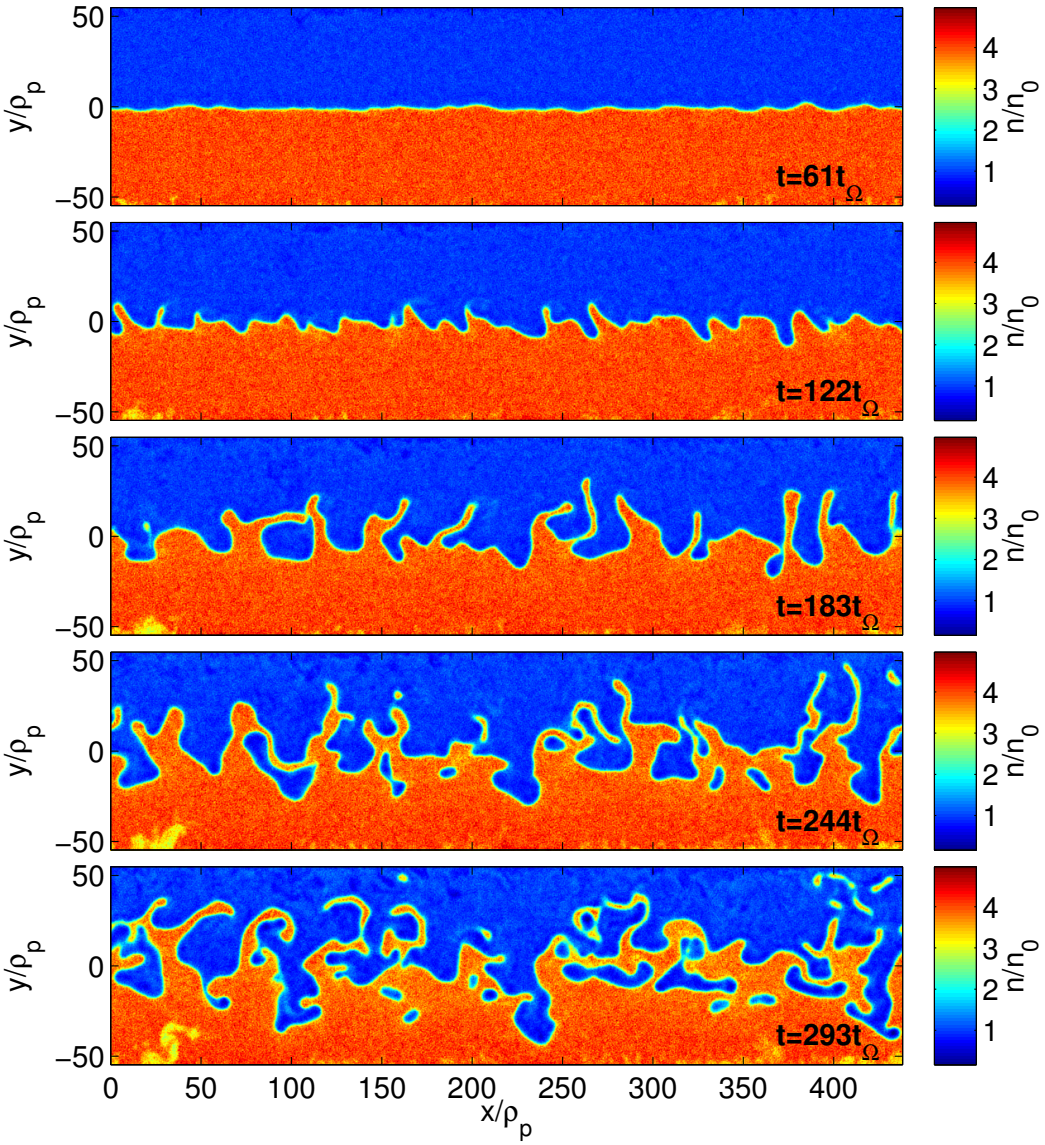

Figure 5.6: Total number density of ions for a simulation initialised with a pressure gradient of width $a = \Delta y$ at $y = 0$. The growth of the interchange instability can be seen to lead to separation of blobs from the higher density layer from $t = 220t_\Omega$.

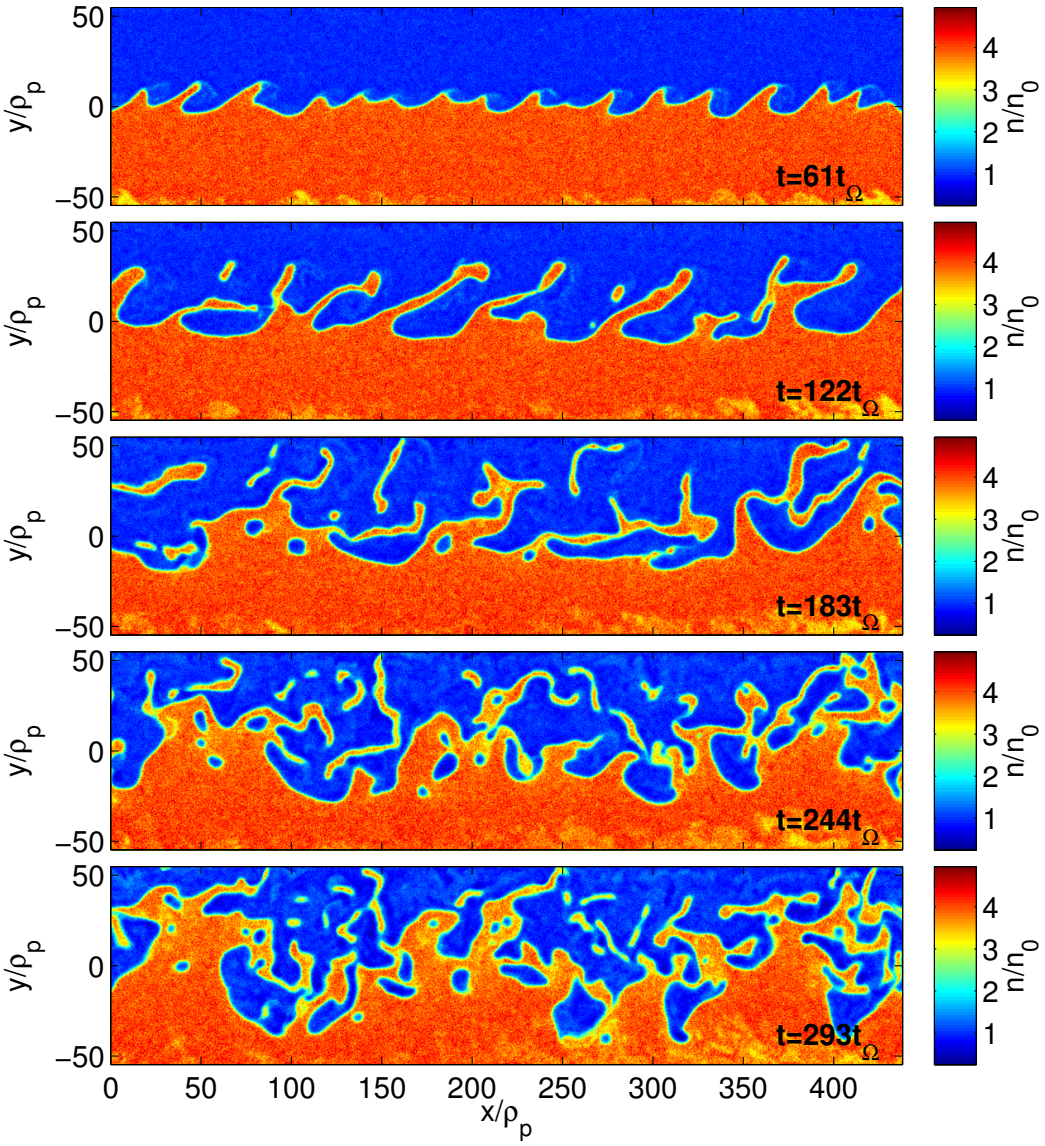

Figure 5.7: Total number density of ions for a proton plasma simulation initialised with a shear boundary and pressure gradient at $y = 0$ with flows $u_{\mathrm{top/bot}} = \pm 0.02 v_A$ and boundary width $a = \Delta y$. The combination of Kelvin-Helmholtz and interchange instabilities leads to separation of blobs from the high density, lower layer at significantly earlier times than the case with no shear boundary.

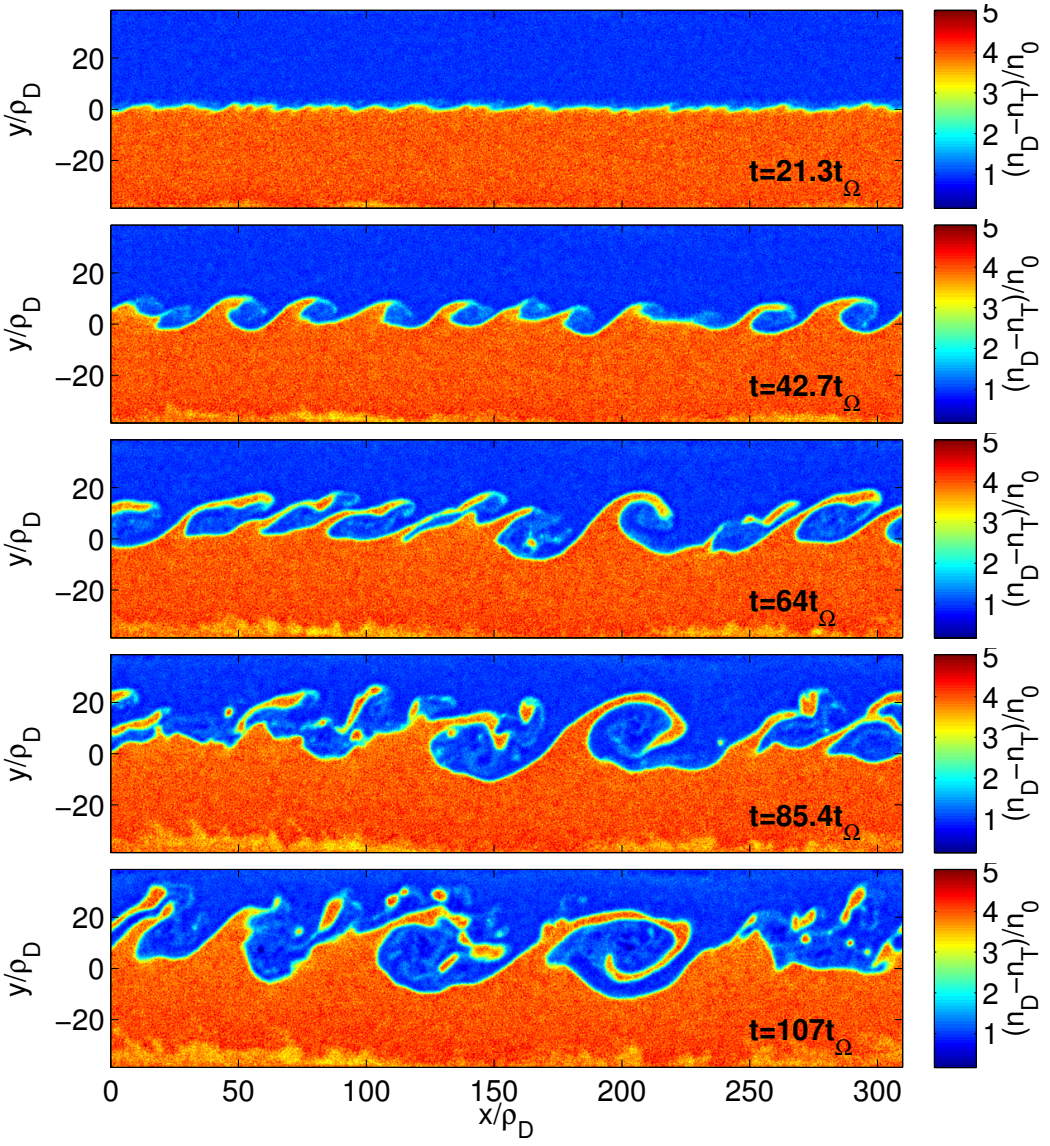

Figure 5.8: Total number density of all ion species for a D-T plasma simulation initialised with a shear boundary and pressure gradient at $y = 0$ with flows $u_{\mathrm{top/bot}} = \pm 0.02 v_A$ and boundary width $a = \Delta y$. The growth rate of both K-H and interchange instabilities is significantly reduced compared with the proton plasma cases, with suppression of small scale modes. As a consequence, separation of blobs occurs at later times.

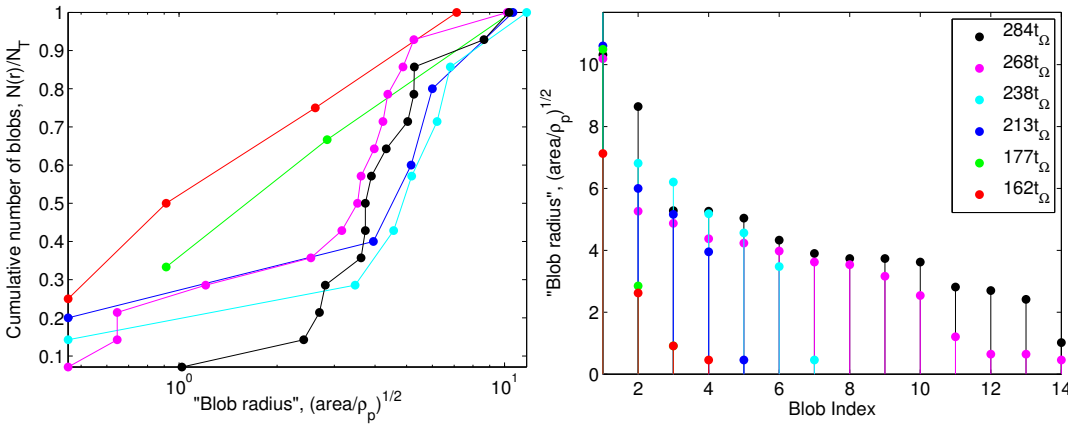

Figure 5.9: Cumulative distribution functions (left) and rank order plots (right) displaying the evolution of the distribution of blob sizes for a proton plasma simulation with a density gradient initialised at $y = 0$.

conditional function $f(x, y, t)$. For example, in the case of over-dense blobs:

$$f(x, y, t) = \begin{cases} 1, & \text{if } n(x, y, t) > n_{\text{threshold}} \\ 0, & \text{otherwise.} \end{cases} \tag{5.3}$$

In the case of holes, the condition instead becomes $n(x, y, t) < n_{\text{threshold}}$. We then label the connected regions in configuration space (x, y) for which $f(x, y, t) = 1$, and measure the properties of these regions, such as their area, for time dependent statistics.

Since the creation of blobs by the interchange and Kelvin-Helmholtz instabilities is relatively rare in our simulations, we present size statistics for each simulation using cumulative distributions and rank order plots. Cumulative distribution functions and rank order plots of blob sizes as the instabilities develop over time are given for the case including a density gradient with no shear boundary in Figure 5.9, for the case including both shear and density gradient in Figure 5.10, and for a D-T plasma with shear and density gradient in Figure 5.11. Cumulative distribution functions and rank order plots of blobs sizes are shown in Figure 5.9 for the proton plasma simulation initialised with a density gradient. The same for simulations initialised with both a density gradient and shear boundary are shown in Figure 5.10 for the proton plasma case, and in Figure 5.11 for the D-T plasma case. The minimum measurable blob size, limited by the size of the grid cells, is $0.4\rho_p$.

These simulations demonstrate that ion gyro-scale blobs contribute a significant portion to the population of blobs in all scenarios discussed here. Approxi-

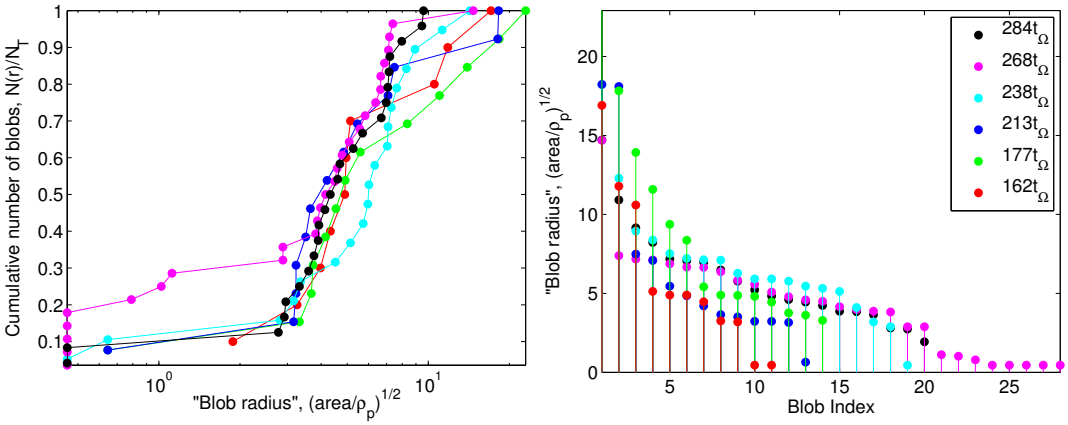

Figure 5.10: Cumulative distribution functions (left) and rank order plots (right) displaying the evolution of the distribution of blob sizes for a proton plasma simulation with a density gradient and shear boundary initialised at $y = 0$. Note that we see a steep increase in the relative number of blobs with radii above approximately $4\rho_p$.

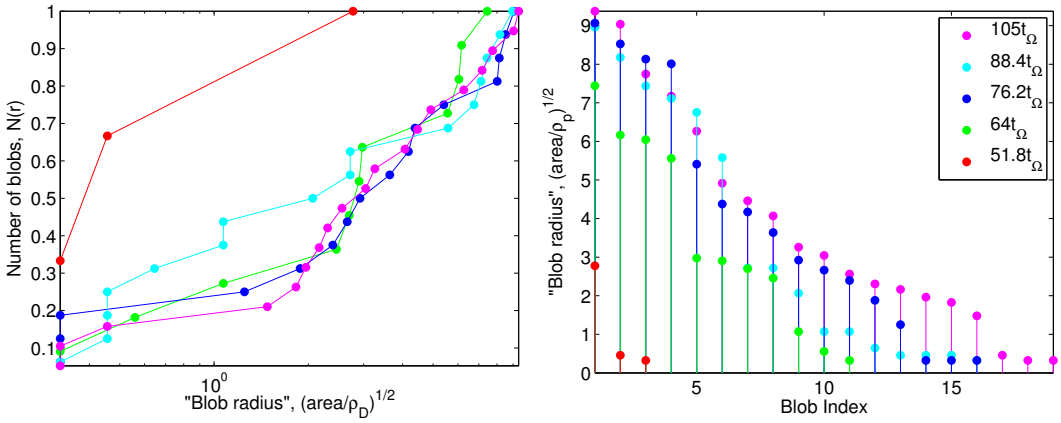

Figure 5.11: Cumulative distribution functions (left) and rank order plots (right) displaying the evolution of the distribution of blob sizes for a D-T plasma simulation with a density gradient and shear boundary initialised at $y = 0$.

mately 70% of the blob population have radii less than $5\rho_i$ in each scenario, with 10-30% with radii less than $2\rho_i$. We also note several trends visible by comparison between simulations. First, once the interchange and Kelvin-Helmholtz instabilities are sufficiently advanced to generate blobs, the cumulative distribution function of blob sizes tends to a distribution which is constant with time, i.e. it tends towards a saturated state. This is demonstrated most clearly by the distribution functions for the proton plasma case in Figure 5.10, for which significant blob creation begins at $\sim 160 t_\Omega$. However, since blob creation is a rare event, significantly larger simulations are needed to confirm saturation in the tail of the distributions. Second, the inclusion of shear appears to lead to the creation of relatively fewer small-scale blobs. For example, with the inclusion of the shear boundary, the distribution function in Figure 5.10 shows a sharp reduction in the number of blobs with radii below $4\rho_p$, in contrast to the more uniform distribution in Figure 5.9. Finally, the increase in ion gyro-radius, and inclusion of two ion populations with different gyro-radii, leads to an increase of the fraction of blobs at small scales. The sharp cut-off of in the distribution function for blobs with radii less than $4\rho_i$ in Figure 5.10 is not observed for the D-T plasma case in Figure 5.11.

To further characterise the creation of gyro-scale blobs by kinetic instabilities, we can measure the packing fraction f_p. As discussed in Section 1.3.2.5, this measures the fraction of the plasma perpendicular to the magnetic field occupied by blobs. Packing fractions for the proton plasma cases featuring interchange and K-H instabilities are given in Figure 5.12. This figure demonstrates first that the inclusion of a shear boundary leads to an earlier blob creation time, consistent with the density plots given above. Second, we observe a higher packing fraction and therefore a faster blob creation rate at all times for the simulation initialised with a shear boundary, in contrast with observations which report a decrease of the packing fraction by shear flows in the SOL [D'Ippolito et al., 2011].

5.3.3 Particle Diffusion

To determine radial particle flux across the shear boundary, and hence measure differences in transport for the fluid and kinetic ion cases, we measure the mean square displacement $\langle \Delta y^2 \rangle$ for populations of ions initialised at regular spacing along $y = 0$, in the viscinity of the shear boundary and density gradient. To characterise the evolution of this mean square displacement, we define a diffusion coefficient D:

$$D = \frac{\langle \Delta y^2 \rangle}{t}. \tag{5.4}$$

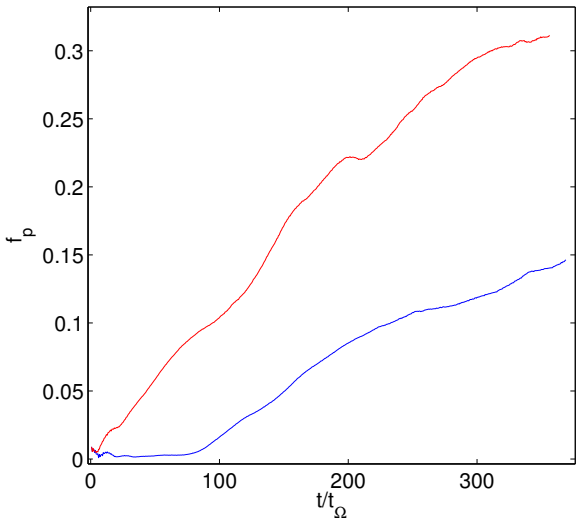

Figure 5.12: Evolution of the packing fractions for proton plasma simulations initialised with a pressure gradient (blue) and both a pressure gradient and shear boundary (red). The inclusion of a shear boundary, and hence the addition of a K-H instability, increases the packing fraction at all times. These packing fractions have been calculated using the fraction of the total area occupied by regions above a threshold density, as in Equation 5.3, in the intially low-density region $y > 0$.

We test for a power law increase in displacement such that $\left\langle \Delta y^2 \right\rangle \propto (\Omega_i t)^\gamma$. For classical diffusion, $\gamma = 1$ and the diffusion coefficient D is constant.

The dependence of the diffusion coefficient D and power law exponent γ on finite Larmor radius effects has been studied for turbulence in the edge region using both Hasegawa-Mima [Manfredi and Dendy, 1996, 1997; Annibaldi et al., 2000, 2002] and Hasegawa-Wakatani [Dewhurst et al., 2010] reduced fluid models. Particle transport studies have included models of ion kinetics that are gyro-averaged [Hauff and Jenko, 2006, 2007] or full Lorentz trajectories [Vlad and Spineanu, 2005]. These simulations have shown that the effect of a finite Larmor radius on particle transport is highly dependent on turbulent vortex scales sizes and shear boundaries. High frequency gyration effectively smooths out small turbulent fluctuations and leads to a reduction in transport [Manfredi and Dendy, 1997; Annibaldi et al., 2002]. However, the reduction is less dramatic, and transport may even increase with gyroradius, for slowly-varying turbulent fluctuations on the order of the gyroradius [Vlad and Spineanu, 2005; Hauff and Jenko, 2007; Dewhurst et al., 2010]. These studies typically report subdiffusive power law exponents $\gamma \sim 0 - 1$ in the radial direction, and superdiffusive power law exponents $\gamma \sim 1 - 2$ in the poloidal direction.

However, in contrast to the geometry chosen here, these simulations include multiple shear layers at the boundaries of several zonal flows. Similar analyses have also been conducted for particle displacement by K-H and interchange instabilities at the magnetopause [Cowee et al., 2009]. The geometry used in [Cowee et al., 2009] more closely resembles the geometry chosen here, with resulting hyperdiffusive power law exponents $\gamma \sim 3 - 4$.

For the simple shear boundary case, for which only the Kelvin-Helmholtz instability grows, the evolution of the mean radial displacement is given in Figure 5.13. Two regions are visible in this graph: at early times $t < 10t_\Omega$ the particle displacement is dominated by gyration, and at later times the evolution is characterised by a hyperdiffusive power law with exponent $\gamma \sim 2$. Here, we also measure the displacement of populations of particles initialised $\pm 5\rho_p$ above and below that boundary to investigate asymmetries resulting from finite Larmor radius effects. In this case, all three ion populations evolve with the same power law, suggesting that differences between populations initialised either side of the shear boundary are not significant. Mean particle displacements for a D-T plasma simulation of the same type are shown for each species in Figure 5.14. In this simulation, we see a third region at times $t > 35t_{\Omega_D} = 70t_{\Omega_p}$ for which the mean particle displacement levels off, which occurs when the K-H instability grows large enough to interact with the simulation boundary. For the time at which the growth of the K-H instability is uninhibited by the boundaries, the power law exponent is increased to $\gamma \sim 3.5$. We also note that the difference between the mean square displacements of the deuteron and triton populations is small. Hence, an increase in the gyroradii from the proton to the D-T plasma results in an increase in radial transport in this case.

The radial particle diffusion for simulations including a density gradient is given for proton plasmas in Figure 5.15 and for a D-T plasma in Figure 5.16. We find the greatest particle displacement occurs for the proton plasma simulation initialised without a shear boundary, with hyperdiffusive power law exponent $\gamma \sim 3.5$. With the introduction of a shear boundary, the power law exponent is reduced to $\gamma \sim 2.5$. However, we note that this is still an increase over the scenario featuring a shear boundary only, for which $n_{\text{top}} = n_{\text{bot}}$. Hence, we can conclude that the interchange instability increases particle transport, and a shear boundary reduces particle transport over long times. These results are consistent with the increase in particle diffusion with increasing density anisotropy seen in [Annibaldi et al., 2002]. Additionally, the power law exponents measured for the simulations including a density gradient and shear boundary are consistent with those measured for magnetospheric instabilities of similar geometry in [Cowee et al., 2009], for which $\gamma \sim 3-4$.

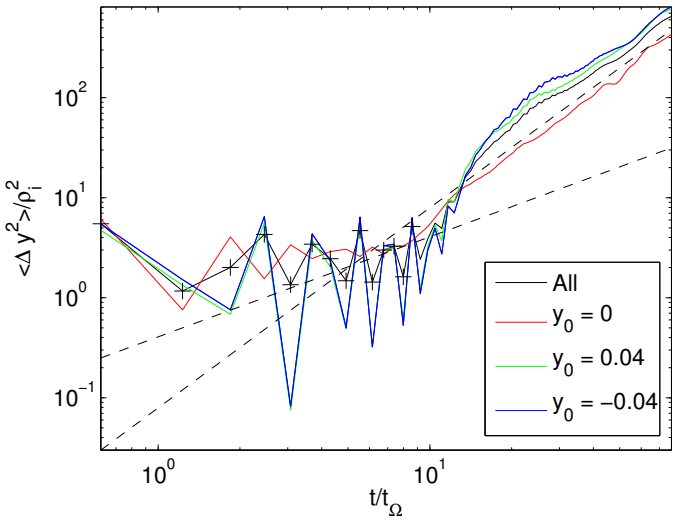

Figure 5.13: Mean particle displacement $\langle \Delta y^2 \rangle$ for the K-H instability in a proton plasma for all tracer particles (black), and for those initialised on (red), above (green) and below (blue) the shear boundary. A power law is visible in the later half of the graph, when the K-H instability becomes significant, with a diffusion power law exponent $\gamma \sim 2$ in all cases. Dashed lines display overlaid power laws for $\gamma = 2$, and for the standard diffusive power law $\gamma = 1$, which is observed in the absense of a shear boundary. At early times, data points are marked with a '+' to demonstrate subsampling of particle gyration at the chosen data sampling rate.

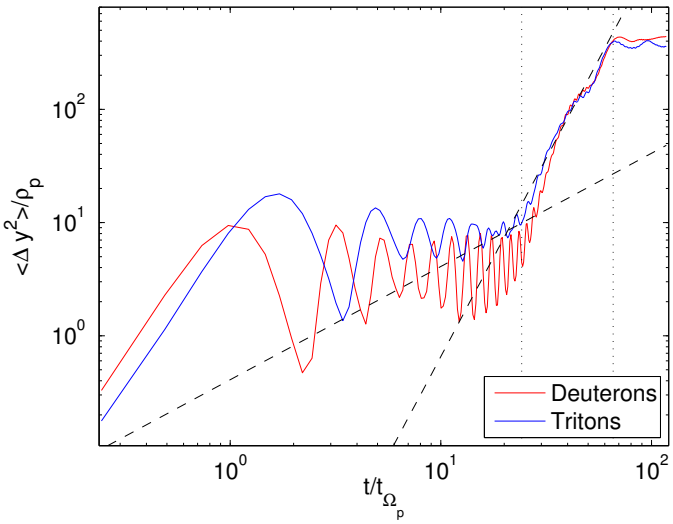

Figure 5.14: Mean particle displacement $\langle \Delta y^2 \rangle$ for the K-H instability in a D-T plasma for all tracer deuterons (red) and tritons (blue). The first section of the graph is dominated by gyration. The central section, between dotted lines, is the period of K-H instability with a clear diffusion power law. In this case, the diffusion exponent for the period shown is $\gamma = 3.5$. The final section of the graph levels off when the K-H instability grows to the size of the simulation domain. Dashed lines display overlaid power laws for $\gamma = 3.5$, and for the standard diffusive power law $\gamma = 1$, which is observed in the absence of a shear boundary.

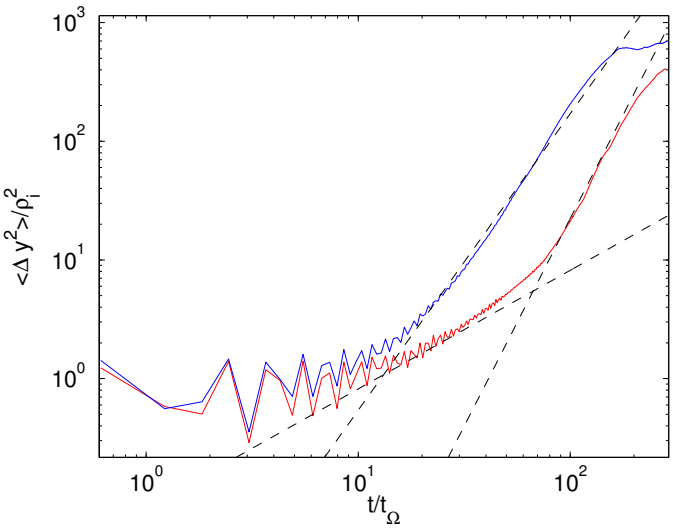

Figure 5.15: Mean particle displacement $\langle \Delta y^2 \rangle$ for proton plasma simulations initialised with a density gradient (red) and with both a density gradient and a shear boundary (blue). Dashed lines display power laws with exponents $\gamma = 2.5$ overlaid on the blue line representing the case of interchange only, and $\gamma = 3.5$ overlaid on the red line representing the case of combined interchange and K-H instabilities. A dashed line displaying the standard diffusive power law $\gamma = 1$ is also given for comparison. Here we find that diffusion of particles is suppressed by the K-H dynamics associated with the shear boundary.

The reduction in transport by the shear boundary is a consequence of the trapping of particles within vortices generated by the K-H instability [Vlad and Spineanu, 2005; Dewhurst et al., 2010]. As part of the dynamics of the K-H instability, these vortices "fold-up" and coalesce at the boundary layer, and do not propagate radially. Particles trapped within these vortices therefore have reduced radial transport. In the D-T plasma case, we again find that mean particle displacement is increased over the proton plasma case, and that deuteron and triton populations follow the same power law, with exponent $\gamma \sim 3$.

5.4 Conclusions

In this Chapter we have demonstrated using hybrid simulations that radially propagating ion gyro-scale blobs can be created in the closed field line region within the separatrix via the interchange instability alone and in combination with the Kelvin-Helmholtz instability. We have shown that the ion kinetic K-H instability does not lead to the creation of propagating blobs at any scale, and holes which form within

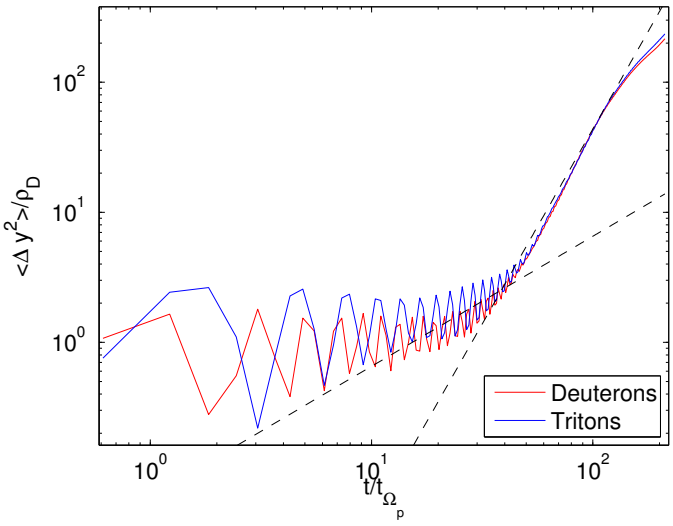

Figure 5.16: Mean particle displacement $\langle \Delta y^2 \rangle$ for a D-T plasma simulation including both pressure gradient and shear boundary. A dashed line displays the power law with exponent $\gamma = 3$. Both deuterons and tritons follow this power law closely. A dashed line representing the standard diffusive power law $\gamma = 1$ is shown for comparison.

coagulating vortices do not propagate away from the shear boundary. An analysis of the distribution of sizes of blobs created by these instabilities has revealed that, for ion gyro-scale boundary widths, ion gyro-scale blobs can account for as much as 70% of the blob population, and that the introduction of a shear boundary can increase the fraction of gyro-scale blobs compared to larger scales. Furthermore, by comparing the statistics of blob creation between proton and D-T plasmas, we have shown that an increase of the ion gyro-radius results in an increase of the fraction of blobs at smaller scales.

An analysis of the mean square displacement of particles has demonstrated that the ion kinetic interchange and Kelvin-Helmholtz instabilities lead to hyperdiffusion of particles in the radial direction, with diffusion power law exponent $\gamma \sim 2-4$. We have shown that the introduction of a shear flow at the boundary reduces the power law exponent, replicating the experimental observation that a shear boundary results in a reduction in radial particle transport. This occurs due to trapping of particles within vortices generated by the K-H instability at the boundary layer. Hence, we can conclude that blobs created in the region of a shear boundary must have reduced radial velocity compared to those created in the absence of shear, and are therefore less able to propagate into the SOL and interact with the vessel wall.

Finally, we have also shown using D-T plasma simulations that an increase in the ion gyro-radius results in an increase in particle transport in the radial direction.

Chapter 6

Conclusions

Throughout this Thesis, we have found that under the hybrid approximation, new physical processes emerge which do not arise under fluid models. We have demonstrated for the first time using ion kinetics in a 6-D phase phase that have not been gyro-averaged that blobs on ion gyro-scales develop structures and gradients on the ion gyro-scale. The specific features that arise are modifications of familiar fluid phenomena subject to an asymmetry governed by finite Larmor radius effects. These asymmetries include a lateral deflection of blobs perpendicular to both the magnetic field direction and blob velocity, and difference in the size of internal vortices, and a difference in the growth rate of the Kelvin-Helmholtz instability between the blobs' upper and lower edges. The strength of these asymmetries has been shown to increase as the size of blobs are reduced and/or the blob velocity is increased.

We have also shown that ion gyro-scale blobs can play a significant role in energy transport from the near-edge region towards the scrape-off layer. Acceleration of ions by pick-up at the blob/background boundary has been shown to have a clear dependence on blob size, with small, gyro-scale blobs increasing the energy of particles at a faster rate than those on fluid scales. The energy increase is also shown to be dependent on blob velocity.

Finally, we have demonstrated the creation of blobs on ion gyro-scales by means of a combination of the interchange instability and the Kelvin-Helmholtz instability in the near-edge, confined region. The statistics of these blobs has been presented, and we have been able to conclude that ion gyro-scale blobs represent a significant portion of the population of blobs born within the separatrix. We have also shown that an increase in ion gyro-radius, and hence stronger kinetic effects, results in an increase in particle transport in the studied regime, for which ion gyro-scale gradients in density and shear exist at tokamak near-edge conditions.

Additionally, we have confirmed the observation that a shear boundary results in a reduction in transport due to trapping of particles within vortices generated by the K-H instability.

Taken together, the results of Chapters 3 to 5 demonstrate that ion kinetic effects on the population of gyro-scale blobs, which may be un-resolvable with current diagnostics, may cause significant energy flow through and within the edge plasma in a tokamak.

The results presented in this Thesis invite further investigation of finite Larmor radius effects on the evolution and dynamics of blobs in the near-edge region of tokamaks via several different avenues. The first is the increase in resolution and expansion of the simulation domain. As computational resources are improved, the grid resolution and the number of particles per computational cell may be increased to more accurately resolve ion kinetic physics, and better sample the tails of particle distribution functions in phase space. An increase in the size of the simulation domain facilitated by an increase in computational resources would also improve the statistics of blob creation presented in Chapter 5, allowing for better estimates of blob creation rate and packing fractions, and better resolution of the distribution functions of gyro-scale blobs. Recent three-dimensional fluid simulations of blob dynamics have also demonstrated phenomena unique to the treatment of blobs as extended filaments. For blob motion on timescales on the order of the timescales for unstable drift waves, for example, the interaction of a filaments with drift wave turbulence has been shown to lead to significant deviation of blob structure from that predicted by 2D simulations [Angus et al., 2012]. These 3D simulations have also demonstrated a reduction in blob radial velocity, and spinning of blobs initialised with parallel structure. Extension of the hybrid code to three dimensions in order to investigate the effect of a finite Larmor radius on these phenomena, and on the evolution of the parallel structure of filaments, is therefore highly desirable.

The second avenue for further investigation is to expand the hybrid code to include more physics. In this Thesis, for example, we have used an isothermal electron fluid with fixed electron temperature. A change in the electron pressure term of the electron momentum equation by inclusion of an evolving, non-uniform, or even anisotropic electron temperature may lead to differences in the evolution of ion gyro-scale blobs reported in Chapter 3, and may also effect the heating by blobs reported in Chapter 4. For example, blobs with internal temperature gradients have been shown to spin, and demonstrate a reduced radial velocity [Myra et al., 2004]. Similarly, we may also wish to investigate the effects of the inertial term in the electron momentum equation, and the collisional term in the Boltzmann equation,

both of which have been neglected for the work presented in this Thesis. However, since these terms are small for the spatio-temporal scales studied here, their effects are expected to be minimal.

The final and perhaps most important avenue for further research is to repeat the simulations presented in this Thesis for background parameters associated with a variety tokamaks, and to better reproduce the geometry and gradients in the edge and near-edge regions of tokamaks. For example, it would be desirable for future simulations to include, by comparison with experimental data, realistic magnetic curvature and gradients in the background magnetic field strength, density and temperature. However, the quasi-neutrality approximation of the hybrid model prevents simulation of the transition of blobs into the region of open field lines, where charge separation drives radial convection.

Bibliography

M. Agostini, S. J. Zweben, R. Cavazzana, P. Scarin, G. Serianni, R. J. Maqueda, and D. P. Stotler. Study of statistical properties of edge turbulence in the National Spherical Torus Experiment with the gas puff imaging diagnostic. Physics of Plasmas, 14(10):102305, October 2007. doi: 10.1063/1.2776912.

J. R. Angus, M. Umansky, and S. I. Krasheninnikov. 3D Blob Modelling with BOUT++. Contributions to Plasma Physics, 52:348–352, June 2012. doi: 10.1002/ctpp.201210015.

Justin R. Angus, Maxim V. Umansky, and Sergei I. Krasheninnikov. Effect of drift waves on plasma blob dynamics. Phys. Rev. Lett., 108:215002, May 2012. doi: 10.1103/PhysRevLett.108.215002. URL `http://link.aps.org/doi/10.1103/PhysRevLett.108.215002`.

S. V. Annibaldi, G. Manfredi, R. O. Dendy, and L. O'C Drury. LETTER TO THE EDITOR: Evidence for strange kinetics in Hasegawa-Mima turbulent transport. Plasma Physics and Controlled Fusion, 42:L13–L22, April 2000. doi: 10.1088/0741-3335/42/4/102.

S. V. Annibaldi, G. Manfredi, and R. O. Dendy. Non-Gaussian transport in strong plasma turbulence. Physics of Plasmas, 9:791–799, March 2002. doi: 10.1063/1.1445426.

G. Y. Antar, M. Tsalas, E. Wolfrum, V. Rohde, and ASDEX Upgrade Team. Turbulence during H- and L-mode plasmas in the scrape-off layer of the ASDEX Upgrade tokamak. Plasma Physics and Controlled Fusion, 50(9):095012, September 2008. doi: 10.1088/0741-3335/50/9/095012.

P. L. Auer, R. W. Kilb, and W. F. Crevier. Thermalization in the earth's bow shock. J. Geophys. Res., 76:2927–2939, 1971. doi: 10.1029/JA076i013p02927.

A. Y. Aydemir. Convective transport in the scrape-off layer of tokamaks. Physics of Plasmas, 12(6):062503–+, June 2005. doi: 10.1063/1.1927539.

T. Bagdonat and U. Motschmann. From a Weak to a Strong Comet - 3d Global Hybrid Simulation Studies. Earth Moon and Planets, 90:305–321, June 2002. doi: 10.1023/A:1021578232282.

W. Baumjohann and R. A. Treumann. Basic space plasma physics. London: Imperial College Press, 1996.

A. R. Bell. The acceleration of cosmic rays in shock fronts. I. Mon. Not. R. Astr. Soc., 182:147–156, January 1978.

G. Belmont and G. Chanteur. Advances in magnetopause Kelvin-Helmholtz instability studies. Physica Scripta, 40:124–128, July 1989. doi: 10.1088/0031-8949/40/1/018.

H. Biglari, P. H. Diamond, and P. W. Terry. Influence of sheared poloidal rotation on edge turbulence. Physics of Fluids B, 2:1–4, January 1990. doi: 10.1063/1.859529.

C.K. Birdsall and A.B. Langdon. Plasma Physics via Computer Simulation. 2005.

J. Birn, J. F. Drake, M. A. Shay, B. N. Rogers, R. E. Denton, M. Hesse, M. Kuznetsova, Z. W. Ma, A. Bhattacharjee, A. Otto, and P. L. Pritchett. Geospace Environmental Modeling (GEM) magnetic reconnection challenge. J. Geophys. Res., 106:3715–3720, March 2001. doi: 10.1029/1999JA900449.

J. Birn, K. Galsgaard, M. Hesse, M. Hoshino, J. Huba, G. Lapenta, P. L. Pritchett, K. Schindler, L. Yin, J. Büchner, T. Neukirch, and E. R. Priest. *Geophys. Res. Lett.*, 320:L06105, March 2005. doi: 10.1029/2004GL022058.

N. Bisai, A. Das, S. Deshpande, R. Jha, P. Kaw, A. Sen, and R. Singh. Edge and scrape-off layer tokamak plasma turbulence simulation using two-field fluid model. Physics of Plasmas, 12(7):072520, July 2005. doi: 10.1063/1.1942427.

J. A. Boedo, D. Rudakov, R. Moyer, S. Krasheninnikov, D. Whyte, G. McKee, G. Tynan, M. Schaffer, P. Stangeby, P. West, S. Allen, T. Evans, R. Fonck, E. Hollmann, A. Leonard, A. Mahdavi, G. Porter, M. Tillack, and G. Antar. Transport by intermittent convection in the boundary of the DIII-D tokamak. Physics of Plasmas, 8:4826–4833, November 2001. doi: 10.1063/1.1406940.

J. A. Boedo, D. L. Rudakov, R. A. Moyer, G. R. McKee, R. J. Colchin, M. J. Schaffer, P. G. Stangeby, W. P. West, S. L. Allen, T. E. Evans, R. J. Fonck,

E. M. Hollmann, S. Krasheninnikov, A. W. Leonard, W. Nevins, M. A. Mahdavi, G. D. Porter, G. R. Tynan, D. G. Whyte, and X. Xu. Transport by intermittency in the boundary of the DIII-D tokamak. Physics of Plasmas, 10:1670–1677, May 2003. doi: 10.1063/1.1563259.

S. H. Brecht. Hybrid simulations of the magnetic topology of Mars. J. Geophys. Res., 102:4743–4750, March 1997. doi: 10.1029/96JA03205.

S. H. Brecht and J. R. Ferrante. J. Geophys. Res., 96:11209, July 1991. doi: 10.1029/91JA00671.

S. H. Brecht and V. A. Thomas. Three-dimensional simulation of an active magnetospheric release. J. Geophys. Res., 92:2289–2304, March 1987. doi: 10.1029/JA092iA03p02289.

D. Burgess. Cyclic behavior at quasi-parallel collisionless shocks. Geophys. Res. Lett., 16:345–348, May 1989. doi: 10.1029/GL016i005p00345.

D. Burgess, E. Möbius, and M. Scholer. Ion Acceleration at the Earth's Bow Shock. Space Sci. Rev., 173:5–47, November 2012. doi: 10.1007/s11214-012-9901-5.

I. T. Chapman, S. Brown, R. Kemp, and N. R. Walkden. Toroidal velocity shear Kelvin-Helmholtz instabilities in strongly rotating tokamak plasmas. Nuclear Fusion, 52(4):042005, April 2012. doi: 10.1088/0029-5515/52/4/042005.

S. C. Chapman and M. W. Dunlop. Ordering of momentum transfer along v (vector) x B (vector) in the AMPTE solar wind releases. J. Geophys. Res., 91:8051–8055, July 1986. doi: 10.1029/JA091iA07p08051.

S. C. Chapman and S. J. Schwartz. One-dimensional hybrid simulations of boundary layer processes in the AMPTE solar wind lithium releases. J. Geophys. Res., 92: 11059–11073, October 1987. doi: 10.1029/JA092iA10p11059.

F. F. Chen. Spectrum of Low-β Plasma Turbulence. Physical Review Letters, 15: 381–383, August 1965. doi: 10.1103/PhysRevLett.15.381.

J. Cheng, L. W. Yan, W. Y Hong, K. J. Zhao, T. Lan, J. Qian, A. D. Liu, H. L. Zhao, Y. Liu, Q. W. Yang, J. Q. Dong, X. R. Duan, and Y. Liu. Statistical characterization of blob turbulence across the separatrix in HL-2A tokamak. Plasma Physics and Controlled Fusion, 52(5):055003, May 2010. doi: 10.1088/0741-3335/52/5/055003.

R. Chodura. A hybrid fluid-particle model of ion heating in high-Mach-number shock waves. Nucl. Fusion, 15:55–61, February 1975.

J. W. Connor. Edge-localized modes - physics and theory. Plasma Physics and Controlled Fusion, 40:531–542, May 1998. doi: 10.1088/0741-3335/40/5/002.

R. Courant, K. Friedrichs, and H. Lewy. Über die partiellen Differenzengleichungen der mathematischen Physik. Mathematische Annalen, 100:32–74, 1928. doi: 10.1007/BF01448839.

M. M. Cowee, D. Winske, and S. P. Gary. Two-dimensional hybrid simulations of superdiffusion at the magnetopause driven by Kelvin-Helmholtz instability. Journal of Geophysical Research (Space Physics), 114:A10209, October 2009. doi: 10.1029/2009JA014222.

P. Debye and E. Hückel. On the Debye length in strong electrolytes. Physikal Z., 24(9):185–206, 1923.

P. A. Delamere, D. W. Swift, and H. C. Stenbaek-Nielsen. A three-dimensional hybrid code simulation of the December 1984 solar wind AMPTE release. Geophys. Res. Lett., 26:2837–2840, 1999. doi: 10.1029/1999GL900602.

R. Dendy, editor. Plasma Physics: an Introductory Course, 1993.

M. I. Desai and D. Burgess. Particle acceleration at coronal mass ejection-driven interplanetary shocks and the Earth's bow shock. Journal of Geophysical Research (Space Physics), 113:A00B06, September 2008. doi: 10.1029/2008JA013219.

P. Devynck, P. Ghendrih, and Y. Sarazin. The origin of the long time correlations of the density fluctuations in the scrape-off layer of the Tore Supra Tokamak. Physics of Plasmas, 12(5):050702, May 2005. doi: 10.1063/1.1894399.

J. M. Dewhurst, B. Hnat, and R. O. Dendy. Finite Larmor radius effects on test particle transport in drift wave-zonal flow turbulence. Plasma Physics and Controlled Fusion, 52(2):025004, February 2010. doi: 10.1088/0741-3335/52/2/025004.

D. A. D'Ippolito and J. R. Myra. Blob stability and transport in the scrape-off-layer. Physics of Plasmas, 10:4029–4039, October 2003. doi: 10.1063/1.1606447.

D. A. D'Ippolito, J. R. Myra, and S. I. Krasheninnikov. *Physics of Plasmas* , 9: 222–233, January 2002. doi: 10.1063/1.1426394.

D. A. D'Ippolito, J. R. Myra, D. A. Russell, and G. Q. Yu. Rotational stability of plasma blobs. Physics of Plasmas, 11:4603–4609, October 2004. doi: 10.1063/1.1785791.

D. A. D'Ippolito, J. R. Myra, and S. J. Zweben. Convective transport by intermittent blob-filaments: Comparison of theory and experiment. Physics of Plasmas, 18(6): 060501, June 2011. doi: 10.1063/1.3594609.

A. I. Ershkovich. Kelvin-Helmholtz instability in type-1 comet tails and associated phenomena. Space Sci. Rev., 25:3–34, January 1980. doi: 10.1007/BF00200796.

D. W. Forslund, K. B. Quest, J. U. Brackbill, and K. Lee. Collisionless dissipation in quasi-perpendicular shocks. J. Geophys. Res., 89:2142–2150, April 1984. doi: 10.1029/JA089iA04p02142.

C. Foullon, E. Verwichte, V. M. Nakariakov, K. Nykyri, and C. J. Farrugia. Magnetic Kelvin-Helmholtz Instability at the Sun. Astr. J. Lett., 729:L8, March 2011. doi: 10.1088/2041-8205/729/1/L8.

I. Furno, B. Labit, A. Fasoli, F. M. Poli, P. Ricci, C. Theiler, S. Brunner, A. Diallo, J. P. Graves, M. Podestà, and S. H. Müller. Mechanism for blob generation in the TORPEX toroidal plasma. Physics of Plasmas, 15(5):055903, May 2008. doi: 10.1063/1.2870082.

X. Garbet, C. Fenzi, H. Capes, P. Devynck, and G. Antar. Kelvin-Helmholtz instabilities in tokamak edge plasmas. Physics of Plasmas, 6:3955–3965, October 1999. doi: 10.1063/1.873659.

O. E. Garcia, N. H. Bian, V. Naulin, A. H. Nielsen, and J. J. Rasmussen. *Physics of Plasmas*, 12(9):090701–+, September 2005. doi: 10.1063/1.2044487.

O. E. Garcia, N. H. Bian, and W. Fundamenski. Radial interchange motions of plasma filaments. Physics of Plasmas, 13(8):082309, August 2006. doi: 10.1063/1.2336422.

J. Giacalone, J. R. Jokipii, and J. Kota. Ion injection and acceleration at quasi-perpendicular shocks. J. Geophys. Res., 99:19351, October 1994. doi: 10.1029/94JA01213.

P. W. Gingell, S. C. Chapman, R. O. Dendy, and C. S. Brady. Transport and evolution of ion gyro-scale plasma blobs in perpendicular magnetic fields. Plasma Physics and Controlled Fusion, 54(6):065005, June 2012. doi: 10.1088/0741-3335/54/6/065005.

P. W. Gingell, S. C. Chapman, and R. O. Dendy. Plasma heating by ion gyro-scale blobs in the kinetic and fluid regimes. Plasma Physics and Controlled Fusion, 55 (5):055010, April 2013.

G. Gloeckler, J. Geiss, E. C. Roelof, L. A. Fisk, F. M. Ipavich, K. W. Ogilvie, L. J. Lanzerotti, R. von Steiger, and B. Wilken. Acceleration of interstellar pickup ions in the disturbed solar wind observed on ULYSSES. J. Geophys. Res., 99: 17637–+, September 1994. doi: 10.1029/94JA01509.

B. Gonçalves, C. Hidalgo, C. Silva, M. A. Pedrosa, and K. Erents. Statistical description of the radial structure of turbulence in the JET plasma boundary region. Journal of Nuclear Materials, 337:376–380, March 2005. doi: 10.1016/j.jnucmat.2004.09.062.

O. Grulke, J. L. Terry, B. Labombard, and S. J. Zweben. Radially propagating fluctuation structures in the scrape-off layer of Alcator C-Mod. Physics of Plasmas, 13(1):012306–+, January 2006. doi: 10.1063/1.2164991.

D. A. Gurnett and A. Bhattacharjee. Introduction to Plasma Physics. Cambridge University Press, January 2005.

S. Hamasaki, N. A. Krall, C. E. Wagner, and R. N. Byrne. Effect of turbulence on theta pinch modeling by hybrid numerical models. Physics of Fluids, 20:65–71, January 1977. doi: 10.1063/1.861708.

J. B. Harold and A. B. Hassam. A simulation of the December 1984 solar wind AMPTE release. Geophys. Res. Lett., 18:135–138, February 1991. doi: 10.1029/90GL02437.

H. Hasegawa, M. Fujimoto, T.-D. Phan, H. Rème, A. Balogh, M. W. Dunlop, C. Hashimoto, and R. TanDokoro. Transport of solar wind into Earth's magnetosphere through rolled-up Kelvin-Helmholtz vortices. Nature (London), 430: 755–758, August 2004. doi: 10.1038/nature02799.

A. B. Hassam and J. D. Huba. Structuring of the AMPTE magnetotail barium releases. Geophys. Res. Lett., 14:60–63, January 1987. doi: 10.1029/GL014i001p00060.

T. Hauff and F. Jenko. Turbulent ExB advection of charged test particles with large gyroradii. Physics of Plasmas, 13(10):102309, October 2006. doi: 10.1063/1.2360173.

T. Hauff and F. Jenko. ExB advection of trace ions in tokamak microturbulence. Physics of Plasmas, 14(9):092301, September 2007. doi: 10.1063/1.2768025.

M. Hesse and D. Winske. *J. Geophys. Res.*, 991:11177–11192, June 1994. doi: 10.1029/94JA00676.

D. W. Hewett. A global method of solving the electron-field equations in a zero-inertia-electron-hybrid plasma simulation code. Journal of Computational Physics, 38:378–395, December 1980. doi: 10.1016/0021-9991(80)90155-2.

D. W. Hewett. Computer Phys. Communications, 84:243–277, November 1994. doi: 10.1016/0010-4655(94)90214-3.

D. Higgins, B. Hnat, A. Kirk, P. Tamain, N. Ben Ayed, and the MAST Team. Plasma Physics and Controlled Fusion, 54(1):015002, January 2012. doi: 10.1088/0741-3335/54/1/015002.

M. J. M. Hill. Royal Society of London Philosophical Transactions Series A, 185: 213–245, 1894. doi: 10.1098/rsta.1894.0006.

J. Horacek, J. Adamek, H. W. Müller, J. Seidl, A. H. Nielsen, V. Rohde, F. Mehlmann, C. Ionita, E. Havlíčková, and ASDEX Upgrade Team. Interpretation of fast measurements of plasma potential, temperature and density in SOL of ASDEX Upgrade. Nuclear Fusion, 50(10):105001, October 2010. doi: 10.1088/0029-5515/50/10/105001.

E. Kallio and P. Janhunen. Ion escape from Mars in a quasi-neutral hybrid model. Journal of Geophysical Research (Space Physics), 107:1035, March 2002. doi: 10.1029/2001JA000090.

J. R. Kan and D. W. Swift. Structure of the quasi-parallel bow shock - Results of numerical simulations. J. Geophys. Res., 88:6919–6925, September 1983. doi: 10.1029/JA088iA09p06919.

H. Karimabadi, D. Krauss-Varban, J. D. Huba, and H. X. Vu. *J.* Geophys. Res., 109:A09205, September 2004. doi: 10.1029/2004JA010478.

Noam Katz, Jan Egedal, Will Fox, Ari Le, and Miklos Porkolab. Experiments on the propagation of plasma filaments. Phys. Rev. Lett., 101:015003, Jul 2008. doi: 10.1103/PhysRevLett.101.015003. URL `http://link.aps.org/doi/10.1103/PhysRevLett.101.015003`.

A. Kirk, N. Ben Ayed, G. Counsell, B. Dudson, T. Eich, A. Herrmann, B. Koch, R. Martin, A. Meakins, S. Saarelma, R. Scannell, S. Tallents, M. Walsh, H. R. Wilson, and the MAST team. Filament structures at the plasma edge on mast. Plasma Physics and Controlled Fusion, 48(12B):B433, 2006. URL http://stacks.iop.org/0741-3335/48/i=12B/a=S41.

N. A. Krall and A. W. Trivelpiece. Principles of plasma physics. San Fransico Press, 1973.

S. Krasheninnikov. Multifaceted physics of edge plasma in magnetic fusion devices. Plasma Physics and Controlled Fusion, 53(7):074017, July 2011. doi: 10.1088/0741-3335/53/7/074017.

S. I. Krasheninnikov. On scrape off layer plasma transport. Phys. Lett. A, 283: 368–370, May 2001. doi: 10.1016/S0375-9601(01)00252-3.

S. I. Krasheninnikov and A. I. Smolyakov. On neutral wind and blob motion in linear devices. Physics of Plasmas, 10:3020–3021, July 2003. doi: 10.1063/1.1579692.

S. I. Krasheninnikov, D. A. D'Ippolito, and J. R. Myra. Recent theoretical progress in understanding coherent structures in edge and sol turbulence. Journal of Plasma Physics, 74:679–717, 9 2008. ISSN 1469-7807. doi: 10.1017/S0022377807006940.

H. Kriegel, S. Simon, J. Müller, U. Motschmann, J. Saur, K.-H. Glassmeier, and M. K. Dougherty. The plasma interaction of Enceladus: 3D hybrid simulations and comparison with Cassini MAG data. Planetary Space Sci., 57:2113–2122, December 2009. doi: 10.1016/j.pss.2009.09.025.

H. Kucharek and M. Scholer. Injection and acceleration of interstellar pickup ions at the heliospheric termination shock. J. Geophys. Res., 100:1745–1754, February 1995. doi: 10.1029/94JA02559.

A.S. Kukushkin, H.D. Pacher, G.W. Pacher, G. Janeschitz, D. Coster, A. Loarte, and D. Reiter. Scaling laws for edge plasma parameters in iter from two-dimensional edge modelling. Nucl. Fusion, 43(8):716, 2003. URL http://stacks.iop.org/0029-5515/43/i=8/a=312.

R. E. Lee, S. C. Chapman, and R. O. Dendy. Numerical Simulations of Local Shock Reformation and Ion Acceleration in Supernova Remnants. Astrophysical Journal, 604:187–195, March 2004. doi: 10.1086/381881.

M. M. Leroy and D. Winske. Backstreaming ions from oblique earth bow shocks. Annales Geophysicae, 1:527–536, December 1983.

M. M. Leroy, C. C. Goodrich, D. Winske, C. S. Wu, and K. Papadopoulos. *Geophys. Res. Lett.*, 8:1269–1272, December 1981. doi: 10.1029/GL008i012p01269.

A. S. Lipatov. The hybrid multiscale simulation technology. Berlin; New York: Springer, Scientific computation, 2002.

A. S. Lipatov, K. Sauer, and K. Baumgärtel. Advances in Space Research, 20:279, January 1997. doi: 10.1016/S0273-1177(97)00547-4.

R. Lundin, H. Borg, B. Hultqvist, A. Zakharov, and R. Pellinen. First measurements of the ionospheric plasma escape from Mars. Nature (London), 341:609–612, October 1989. doi: 10.1038/341609a0.

G. Manfredi and R. O. Dendy. Test-Particle Transport in Strong Electrostatic Drift Turbulence with Finite Larmor Radius Effects. Physical Review Letters, 76:4360–4363, June 1996. doi: 10.1103/PhysRevLett.76.4360.

G. Manfredi and R. O. Dendy. Transport properties of energetic particles in a turbulent electrostatic field. Physics of Plasmas, 4:628–635, March 1997. doi: 10.1063/1.872159.

U. Motschmann and E. Kührt. Space Sci. Rev., 122:197–208, February 2006a. doi: 10.1007/s11214-006-6218-2.

U. Motschmann and E. Kührt. Interaction of the Solar Wind with Weak Obstacles: Hybrid Simulations for Weakly Active Comets and for Mars. Space Sci. Rev., 122:197–208, February 2006b. doi: 10.1007/s11214-006-6218-2.

S. H. Müller, A. Diallo, A. Fasoli, I. Furno, B. Labit, and M. Podestà. Plasma blobs in a basic toroidal experiment: Origin, dynamics, and induced transport. Physics of Plasmas, 14(11):110704, November 2007. doi: 10.1063/1.2813193.

J. R. Myra. Current carrying blob filaments and edge-localized-mode dynamics. Physics of Plasmas, 14(10):102314, October 2007. doi: 10.1063/1.2776900.

J. R. Myra, D. A. D'Ippolito, S. I. Krasheninnikov, and G. Q. Yu. Convective transport in the scrape-off-layer by nonthermalized spinning blobs. Physics of Plasmas, 11:4267–4274, September 2004. doi: 10.1063/1.1774168.

J. R. Myra, D. A. D'Ippolito, D. P. Stotler, S. J. Zweben, B. P. Leblanc, J. E. Menard, R. J. Maqueda, and J. Boedo. Blob birth and transport in the tokamak edge plasma: Analysis of imaging data. Physics of Plasmas, 13(9):092509–+, September 2006. doi: 10.1063/1.2355668.

J. R. Myra, D. A. Russell, D. A. D'Ippolito, J.-W. Ahn, R. Maingi, R. J. Maqueda, D. P. Lundberg, D. P. Stotler, S. J. Zweben, J. Boedo, M. Umansky, and NSTX Team. Reduced model simulations of the scrape-off-layer heat-flux width and comparison with experiment. Physics of Plasmas, 18(1):012305, January 2011. doi: 10.1063/1.3526676.

H. Nagano. *Planet. Space Sci.*, 27:881–884, June 1979. doi: 10.1016/0032-0633(79)90013-8.

I. Nanobashvili, P. Devynck, J. P. Gunn, S. Nanobashvili, J. Stöckel, and G. van Oost. Comparative analysis of intermittent burst temporal characteristics at the edge of the CASTOR and Tore Supra tokamaks. Physics of Plasmas, 16(2):022309, February 2009. doi: 10.1063/1.3074787.

A. V. Nedospasov. Edge turbulence in tokamaks. Journal of Nuclear Materials, 196: 90–100, December 1992. doi: 10.1016/S0022-3115(06)80015-2.

B. Nold, G. D. Conway, T. Happel, H. W. Müller, M. Ramisch, V. Rohde, U. Stroth, and ASDEX Upgrade Team. Generation of blobs and holes in the edge of the ASDEX Upgrade tokamak. Plasma Physics and Controlled Fusion, 52(6):065005, June 2010. doi: 10.1088/0741-3335/52/6/065005.

K. Nykyri and A. Otto. Plasma transport at the magnetospheric boundary due to reconnection in Kelvin-Helmholtz vortices. Geophys. Res. Lett., 28:3565–3568, September 2001. doi: 10.1029/2001GL013239.

L. Ofman and B. J. Thompson. SDO/AIA Observation of Kelvin-Helmholtz Instability in the Solar Corona. Astr. J. Lett., 734:L11, June 2011. doi: 10.1088/2041-8205/734/1/L11.

W. Park, E. V. Belova, G. Y. Fu, X. Z. Tang, H. R. Strauss, and L. E. Sugiyama. Plasma simulation studies using multilevel physics models. Phys. Plasmas, 6: 1796–1803, May 1999. doi: 10.1063/1.873437.

M. A. Pedrosa, C. Hidalgo, B. A. Carreras, R. Balbín, I. García-Cortés, D. Newman, B. van Milligen, E. Sánchez, J. Bleuel, M. Endler, S. Davies, and G. F. Matthews. Empirical Similarity of Frequency Spectra of the Edge-Plasma Fluctuations in

Toroidal Magnetic-Confinement Systems. Physical Review Letters, 82:3621–3624, May 1999. doi: 10.1103/PhysRevLett.82.3621.

J. L. Phillips, J. G. Luhmann, C. T. Russell, and K. R. Moore. Finite Larmor radius effect on ion pickup at Venus. J. Geophys. Res., 92:9920–9930, September 1987. doi: 10.1029/JA092iA09p09920.

M. Podestà, A. Fasoli, B. Labit, I. Furno, P. Ricci, F. M. Poli, A. Diallo, S. H. Müller, and C. Theiler. Cross-field transport by instabilities and blobs in a magnetized toroidal plasma. Phys. Rev. Lett., 101:045001, Jul 2008. doi: 10.1103/PhysRevLett.101.045001. URL `http://link.aps.org/doi/10.1103/PhysRevLett.101.045001`.

P. L. Pritchett and F. S. Mozer. Rippling mode in the subsolar magnetopause current layer and its influence on three-dimensional magnetic reconnection. J. Geophys. Res., 116:A04215, April 2011. doi: 10.1029/2010JA016190.

K. B. Quest. Simulations of high-Mach-number collisionless perpendicular shocks in astrophysical plasmas. Physical Review Letters, 54:1872–1874, April 1985. doi: 10.1103/PhysRevLett.54.1872.

K. B. Quest. Very high Mach number shocks - Theory. Advances in Space Research, 6:33–39, 1986. doi: 10.1016/0273-1177(86)90006-2.

M. N. Rosenbluth and C. L. Longmire. Stability of plasmas confined by magnetic fields. Annals of Physics, 1:120–140, May 1957. doi: 10.1016/0003-4916(57)90055-6.

D. L. Rudakov, J. A. Boedo, R. A. Moyer, P. C. Stangeby, J. G. Watkins, D. G. Whyte, L. Zeng, N. H. Brooks, R. P. Doerner, T. E. Evans, M. E. Fenstermacher, M. Groth, E. M. Hollmann, S. I. Krasheninnikov, C. J. Lasnier, A. W. Leonard, M. A. Mahdavi, G. R. McKee, A. G. McLean, A. Y. Pigarov, W. R. Wampler, G. Wang, W. P. West, and C. P. C. Wong. Far SOL transport and main wall plasma interaction in DIII-D. Nuclear Fusion, 45:1589–1599, December 2005. doi: 10.1088/0029-5515/45/12/014.

D. A. Russell, D. A. D'Ippolito, J. R. Myra, W. M. Nevins, and X. Q. Xu. Blob dynamics in 3d bout simulations of tokamak edge turbulence. Phys. Rev. Lett., 93(26):265001, Dec 2004. doi: 10.1103/PhysRevLett.93.265001.

D. A. Russell, J. R. Myra, and D. A. D'Ippolito. Collisionality and magnetic geometry effects on tokamak edge turbulent transport. II. Many-blob turbulence

in the two-region model. Physics of Plasmas, 14(10):102307, October 2007. doi: 10.1063/1.2780137.

K. Sauer, A. Bogdanov, and K. Baumgartel. The protonopause-an ion composition boundary in the magnetosheath of comets, Venus and Mars. Advances in Space Research, 16:153–, August 1995.

H. Schmitz and R. Grauer. Kinetic Vlasov simulations of collisionless magnetic reconnection. Physics of Plasmas, 13(9):092309, September 2006. doi: 10.1063/1.2347101.

H. Schmitz, S. C. Chapman, and R. O. Dendy. Electron Preacceleration Mechanisms in the Foot Region of High Alfvénic Mach Number Shocks. Astrophysical Journal, 579:327–336, November 2002. doi: 10.1086/341733.

M. Scholer, I. Shinohara, and S. Matsukiyo. Quasi-perpendicular shocks: Length scale of the cross-shock potential, shock reformation, and implication for shock surfing. Journal of Geophysical Research (Space Physics), 108:1014, January 2003. doi: 10.1029/2002JA009515.

A. G. Sgro and C. W. Nielson. Hybrid model studies of ion dynamics and magnetic field diffusion during pinch implosions. Physics of Fluids, 19:126–133, January 1976. doi: 10.1063/1.861309.

H. Shimazu. Three-dimensional hybrid simulation of solar wind interaction with unmagnetized planets. J. Geophys. Res., 106:8333–8342, May 2001. doi: 10.1029/2000JA900069.

S. Simon and U. Motschmann. *Planet.* Space Sci., 57:2001–2015, December 2009. doi: 10.1016/j.pss.2009.08.010.

R. Smets, G. Belmont, D. Delcourt, and L. Rezeau. Diffusion at the Earth magnetopause: enhancement by Kelvin-Helmholtz instability. Annales Geophysicae, 25:271–282, February 2007. doi: 10.5194/angeo-25-271-2007.

A. I. Smolyakov, P. H. Diamond, and M. Malkov. Coherent Structure Phenomena in Drift Wave-Zonal Flow Turbulence. Physical Review Letters, 84:491–494, January 2000. doi: 10.1103/PhysRevLett.84.491.

D. J. Southwood and M. G. Kivelson. Magnetospheric interchange instability. J. Geophys. Res., 92:109–116, January 1987. doi: 10.1029/JA092iA01p00109.

M. Spolaore, V. Antoni, E. Spada, H. Bergsåker, R. Cavazzana, J. R. Drake, E. Martines, G. Regnoli, G. Serianni, and N. Vianello. Vortex-Induced Diffusivity In Reversed Field Pinch Plasmas. Physical Review Letters, 93(21):215003, November 2004. doi: 10.1103/PhysRevLett.93.215003.

Y. Su, Q. Lu, C. Huang, M. Wu, X. Gao, and S. Wang. Particle acceleration and generation of diffuse superthermal ions at a quasi-parallel collisionless shock: Hybrid simulations. Journal of Geophysical Research (Space Physics), 117:A08107, August 2012. doi: 10.1029/2012JA017736.

D. Sundkvist and S. D. Bale. Characteristic Parameters of Drift Vortices Coupled to Alfvén Waves in an Inhomogeneous Space Plasma. Phys. Rev. Lett., 101(6): 065001, August 2008. doi: 10.1103/PhysRevLett.101.065001.

D. Sundkvist, V. Krasnoselskikh, P. K. Shukla, A. Vaivads, M. André, S. Buchert, and H. Rème. In situ multi-satellite detection of coherent vortices as a manifestation of Alfvénic turbulence. Nature (London), 436:825–828, August 2005. doi: 10.1038/nature03931.

D. W. Swift. *Geophys.* Res. Lett., 22:311–314, February 1995. doi: 10.1029/94GL03082.

N. Terada, S. Machida, and H. Shinagawa. Global hybrid simulation of the Kelvin-Helmholtz instability at the Venus ionopause. Journal of Geophysical Research (Space Physics), 107:1471, December 2002. doi: 10.1029/2001JA009224.

T. Terasawa, T. Mukai, M. Kitayama, W. Miyake, and K. Hirao. Detection of cometary pickup ions up to 10 to the 7th KM from Comet Halley - Suisei observation. Geophys. Res. Lett., 13:837–840, August 1986. doi: 10.1029/GL013i008p00837.

J. L. Terry, S. J. Zweben, K. Hallatschek, B. Labombard, R. J. Maqueda, B. Bai, C. J. Boswell, M. Greenwald, D. Kopon, W. M. Nevins, C. S. Pitcher, B. N. Rogers, D. P. Stotler, and X. Q. Xu. Observations of the turbulence in the scrape-off-layer of Alcator C-Mod and comparisons with simulation. Physics of Plasmas, 10:1739–1747, May 2003. doi: 10.1063/1.1564090.

J. L. Terry, N. P. Basse, I. Cziegler, M. Greenwald, O. Grulke, B. La Bombard, S. J. Zweben, E. M. Edlund, J. W. Hughes, L. Lin, Y. Lin, M. Porkolab, M. Sampsell, B. Veto, and S. J. Wukitch. Transport phenomena in the edge of Alcator C-Mod plasmas. Nuclear Fusion, 45:1321–1327, November 2005. doi: 10.1088/0029-5515/45/11/013.

R. A. Treumann and W. Baumjohann. Advanced space plasma physics. London: Imperial College Press, 1997.

A. Valenzuela, G. Haerendel, H. Foeppl, F. Melzner, and H. Neuss. The AMPTE artificial comet experiments. Nature (London), 320:700–703, April 1986. doi: 10.1038/320700a0.

J. Villasenor and O. Buneman. Rigorous charge conservation for local electromagnetic field solvers. Computer Physics Communications, 69:306–316, March 1992. doi: 10.1016/0010-4655(92)90169-Y.

M. Vlad and F. Spineanu. Larmor radius effects on impurity transport in turbulent plasmas. Plasma Physics and Controlled Fusion, 47:281–294, February 2005. doi: 10.1088/0741-3335/47/2/006.

A. A. Vlasov. On the kinetic theory of an assembly of particles with collective interaction. J. Phys. (USSR), 9:25–40, 1945.

F. Wagner, G. Becker, K. Behringer, D. Campbell, A. Eberhagen, W. Engelhardt, G. Fussmann, O. Gehre, J. Gernhardt, G. V. Gierke, G. Haas, M. Huang, F. Karger, M. Keilhacker, O. Klüber, M. Kornherr, K. Lackner, G. Lisitano, G. G. Lister, H. M. Mayer, D. Meisel, E. R. Müller, H. Murmann, H. Niedermeyer, W. Poschenrieder, H. Rapp, H. Röhr, F. Schneider, G. Siller, E. Speth, A. Stäbler, K. H. Steuer, G. Venus, O. Vollmer, and Z. Yü. Regime of Improved Confinement and High Beta in Neutral-Beam-Heated Divertor Discharges of the ASDEX Tokamak. Physical Review Letters, 49:1408–1412, November 1982. doi: 10.1103/PhysRevLett.49.1408.

J. Wesson. Tokamaks (Third Edition). Oxford University Press, 2004.

H. R. Wilson, S. C. Cowley, A. Kirk, and P. B. Snyder. Magneto-hydrodynamic stability of the H-mode transport barrier as a model for edge localized modes: an overview. Plasma Physics and Controlled Fusion, 48(26):A260000–A84, May 2006. doi: 10.1088/0741-3335/48/5A/S06.

T. Windisch, O. Grulke, V. Naulin, and T. Klinger. Intermittent transport events in a cylindrical plasma device: experiment and simulation. Plasma Physics and Controlled Fusion, 53(8):085001, August 2011. doi: 10.1088/0741-3335/53/8/085001.

D. Winske, L. Yin, N. Omidi, and et al. In J. Büchner, C. Dum, & M. Scholer, editor, Space Plasma Simulation, volume 615 of Lecture Notes in Physics, Berlin Springer Verlag, pages 136–165, 2003.

G. S. Xu, V. Naulin, W. Fundamenski, C. Hidalgo, J. A. Alonso, C. Silva, B. Gonçalves, A. H. Nielsen, J. J. Rasmussen, S. I. Krasheninnikov, B. N. Wan, M. Stamp, and J. EFDA Contributors. LETTER: Blob/hole formation and zonal-flow generation in the edge plasma of the JET tokamak. Nuclear Fusion, 49(9): 092002, September 2009. doi: 10.1088/0029-5515/49/9/092002.

Y. H. Xu, S. Jachmich, R. R. Weynants, and TEXTOR Team. On the properties of turbulence intermittency in the boundary of the TEXTOR tokamak. Plasma Physics and Controlled Fusion, 47:1841–1855, October 2005. doi: 10.1088/0741-3335/47/10/014.

K. Yee. Numerical solution of inital boundary value problems involving maxwell's equations in isotropic media. IEEE Transactions on Antennas and Propagation, 14:302–307, May 1966. doi: 10.1109/TAP.1966.1138693.

L. Yin, D. Winske, S. P. Gary, and J. Birn. *J. Geophys. Res.*, 106:10761–10776, June 2001. doi: 10.1029/2000JA000398.

G. Q. Yu and S. I. Krasheninnikov. Dynamics of blobs in scrape-off-layer/shadow regions of tokamaks and linear devices. Physics of Plasmas, 10:4413–4418, November 2003. doi: 10.1063/1.1616937.

G. Q. Yu, S. I. Krasheninnikov, and P. N. Guzdar. *Physics of Plasmas*, 13(4): 042508–+, April 2006. doi: 10.1063/1.2193087.

S. J. Zweben, J. A. Boedo, O. Grulke, C. Hidalgo, B. La Bombard, R. J. Maqueda, P. Scarin, and J. L. Terry. Edge turbulence measurements in toroidal fusion devices. Plasma Physics and Controlled Fusion, 49:1, July 2007. doi: 10.1088/0741-3335/49/7/S01.